The ISM properties and evolution in AGNs

por

Yari Juárez López

Tesis sometida como requisito parcial para obtener el grado de **Doctorado en Ciencias en la especialidad de Astrofísica** en el Instituto Nacional de Astrofísica, Óptica y Electrónica.

Supervisada por:

Dr. Raúl Mújica García
Dr. Roberto Maiolino

Sta. Ma. Tonantzintla, Pue.
Octubre de 2009

The ISM properties and evolution in AGNs

por

Yari Juárez López

Tesis sometida como requisito parcial para obtener el grado de Doctorado en Ciencias en la especialidad de Astrofísica en el Instituto Nacional de Astrofísica, Óptica y Electrónica.

Supervisada por:
Dr. Raúl Mújica García
Dr. Roberto Maiolino

Sta. Ma. Tonantzintla, Pue.
Octubre de 2009

Abstract

A infrared (IR) and submillimeter/millimeter (submm/mm) study of a sample of Active Galactic Nuclei (AGNs) is presented in this thesis. The aim is to investigate the metallicity and dust evolution in these objects.

The work is divided in three sections. In the first part, we investigated the metallicity of the Broad Line Region (BLR) in a sample of 27 quasars in the redshift range $4 \leq z \leq 6.4$, by using near-IR (NIR) spectra. We focus on the ratio of the broad lines (SiIV1398+OIV1402)/CIV1549), which is a good metallicity tracer of the BLR. We find that the BLR metallicity is very high even in quasars at $z \sim 6$. The inferred metallicity of the BLR gas is so high (several times solar) that ejection or mixing of metals with lower metallicity in the host galaxy is required to match the metallicities observed in the local massive galaxies. On average, the observed metallicity does not change among the quasars in the observed redshift range $4 \leq z \leq 6.4$, not even when compared with quasars at lower redshifts. We show the apparent lack of metallicity evolution is, probably, a consequence of both: the black hole−galaxy co-evolution and the selection effects. The data also suggest a lack of evolution of the carbon abundance, even among $z > 6$ quasars. The latter result is puzzling, since the minimum enrichment timescale of carbon is about 1 Gyr, i.e., longer than the age of the universe at $z \sim 6$.

The second part focuses on a sample of 168 high redshift radio-quiet quasars ($1.5 \leq z \leq 6.4$) with submm/mm observations. The submm/mm emission implies far-IR (FIR) luminosities of order $10^{13} L_{\odot}$, suggesting substantial star formation (SF) activity. We found there is no apparent difference in the FIR luminosities of quasars at $z \sim 2$ and at $z \geq 4$. We investigated the correlation between the FIR luminosity with other quasar properties, such as black hole (BH) mass, [OIII] luminosity, metallicity, and UV luminosity. The FIR luminosity is correlated with the BH mass, which implies a connection between BH masses and SF in the host galaxies. We see an increment in the FIR luminosity with the [OIII] luminosity, indicating the [OIII] emission is associated with enhanced SF in the host galaxy. No correlation was found between FIR luminosity and metallicity, which probably implies that current SF in quasar hosts is not a significant source of metal enrichment for the gas. In order to study the dust content, we obtained the monochromatic luminosities at the rest frame 1500 Å. We found a strong correlation between FIR and UV luminosities.

Moreover, the ratio of the FIR luminosity to the UV luminosity decreases from $z = 1.5$ to $z \sim 6$, indicating an evolution in the dust mass at $z \sim 5$. Large Millimeter telescope (LMT), Atacama Large Millimeter Array (ALMA), James Webb Space Telescope (JWST), and Herschel telescopes will allow us to confirm these results.

In the third part, we combined *Spitzer* data with X-ray data from the literature in order to investigate the X-ray−IR connection for AGNs. The sample consists of 127 sources. We studied the correlation between the mid-IR (MIR) and absorption corrected hard X-ray luminosities. A high correlation is found between the rest frame $6.7\,\mu$m ($L_{\rm MIR}$) and $2-10$ keV ($L_{\rm X}$) luminosities, following the non-linear relation $\lambda L_{\lambda}(6.7\,\mu{\rm m}) \propto L_{\rm X}^{0.82}$. We found type 1 and type 2 AGNs have the same distribution of $L_{\rm X}$ over $L_{\rm MIR}$, which is in agreement with the idea of clumpy torus. However, the dust covering factor measured by the ratio of dust torus luminosity to X-ray luminosity does not show correlation with $L_{\rm X}$. We also found the $9.7\,\mu$m silicate strength correlates with the intrinsic column density $N_{\rm H}$, estimated from X-ray data, which is consistent with the unified scheme. The $7.7\,\mu$m Polycyclic Aromatic Hydrocarbon (PAH) emission feature, expected from starburst activity, was used to estimate the star formation rate (SFR). A relationship is seen between SFR and X-ray luminosity: more luminous AGNs have large SFRs. The dust covering factor shows a trend to increase with the SFR. Finally, no correlation was found between X-ray absorption and SFRs nor between silicate strength with SFRs.

Resumen

En esta tesis se presenta un estudio de Núcleos Activos de Galaxias (AGNs) usando observaciones en el IR y submm/mm con el objetivo de investigar la evolución de la metalicidad así como la evolución del polvo.

El trabajo está dividido en tres partes. En la primera, estudiamos la metalicidad de la Región de Líneas Anchas (BLR) en una muestra de 27 cuásares entre $4 \leq z \leq 6.4$, usando espectros en el NIR. Nos centramos en la tasa (SiIV1398+OIV1402)/CIV1549), que es un buen indicador de la metalicidad de la BLR. Encontramos que ésta metalicidad es muy alta, incluso en cuásares a $z \sim 6$. La metalicidad inferida del gas en la BLR es tan alta, varias veces la solar, que es necesaria la eyección o la mezcla de metales con baja metalicidad en la galaxia anfitriona, de tal manera que sean similares a las metalicidades observadas en las galaxias masivas locales. En promedio, la metalicidad observada no cambia para cuásares en el intervalo de corrimiento al rojo $4 \leq z \leq 6.4$, ni cuando se compara con los cuásares a bajos corrimientos al rojo. La falta aparente de la evolución en la metalicidad es, probablemente, una consecuencia tanto de co-evolución agujero negro−galaxia, como de efectos de selección. Los datos también muestran una falta de evolución en la abundancia de carbón, aún entre los cuásares a $z > 6$. Este último resultado es desconcertante, ya que el tiempo mínimo de enriquecimiento de carbón es de aproximadamente 1 Gyr, es decir, más grande que la edad del universo a $z \sim 6$.

La segunda parte se centra en una muestra de 168 cuásares radio-callados (*radio-quiet*) a alto corrimiento al rojo ($1.5 \leq z \leq 6.4$) con observaciones en el submm/mm. La emisión submm/mm implica luminosidades en el FIR del orden de $10^{13} L_{\odot}$, sugiriendo una actividad intensa de formación estelar. Encontramos que no hay diferencia aparente en las luminosidades en el FIR de los cuásares a $z \sim 2$ y a $z \geq 4$. Además, estudiamos la correlación entre la luminosidad en el FIR con otras propiedades de los cuásares, tales como la masa del agujero negro (BH), la luminosidad de [OIII], la metalicidad y la luminosidad en el UV. La luminosidad en el FIR está correlacionada con la masa del BH, es decir, hay una intensa formación estelar asociada con la masa del BH. También observamos un aumento de la luminosidad en el FIR con la luminosidad de [OIII], indicando que la emisión de [OIII] está asociada con intensa formación estelar en la galaxia anfitriona. No se encontró correlación entre la luminosidad en el FIR y la metalicidad, lo cual probablemente implica que reciente formación estelar en las galaxias anfitrionas no es una fuente importante de enriquecimiento de metal para el gas. Para verificar si hay una evolución en el contenido de polvo se calcularon las

luminosidades monocromáticas a 1500 Å y encontramos una fuerte correlación entre las luminosidades en el FIR y en el UV. Además, encontramos que la tasa FIR/UV disminuye para corrimientos al rojo altos, indicando una evolución en la masa del polvo a $z > 5$. La siguiente generación de telescopios (GTM, ALMA, JWST y Herschel) nos permitirán confirmar estos resultados.

En la tercera parte combinamos datos de *Spitzer* con datos en rayos X tomados de la literatura para estudiar la conexión rayos X−IR en una muestra de 127 AGNs. Investigamos la correlación entre el MIR y las luminosidades en rayos X duros corregidas por absorción. Encontramos una alta correlación entre las luminosidades a $6.7\,\mu$m en el sistema en reposo ($L_{\rm MIR}$) y $2-10\,$keV ($L_{\rm X}$), siguiendo una relación no-lineal $\lambda L_{\lambda}(6.7\,\mu{\rm m}) \propto L_{\rm X}^{0.82}$. Los AGNs tipo 1 y tipo 2 muestran la misma distribución de $L_{\rm X}$ sobre $L_{\rm MIR}$, de acuerdo con el modelo de un toro que es *clumpy*. Sin embargo, el factor de cobertura del polvo, medido mediante la tasa luminosidad en el MIR a luminosidad en rayos X, no muestra correlación con $L_{\rm X}$. Además, encontramos que la intensidad de silicatos (*silicate strength*) a $9.7\,\mu$m está correlacionada con la densidad columnar intrínseca $N_{\rm H}$, obtenida de datos en rayos X, lo cual es consistente con el modelo unificado. La emisión de hidrocarburo aromático policíclico (PAH) a $7.7\,\mu$m, la cual está asociada a actividad *starburst*, se utilizó para estimar la tasa de formación estelar (SFR). Observamos una relación entre la SFR y la luminosidad en rayos X: los AGNs más luminosos tienen grandes SFRs. Por otro lado, el factor de cobertura del polvo muestra una tendencia a aumentar con la SFR. Finalmente, no encontramos correlación entre la SFR y la densidad columnar en rayos X ni con la *silicate strength*.

Dedications

To my beloved husband Oscar.

None of this would be possible without your love and support.

To my parents and my sister.

Who offered me unconditional love and support throughout the course of this thesis.

Acknowledgments

These words are some of the last written during my work on the thesis (but probably among the first looked at by the reader). It is a pleasure for me to be able to thank the numerous persons who in one way or another have contributed towards the completion of this thesis.

I am especially grateful to my supervisors Dr. Raúl Mújica García and Dr. Roberto Maiolino for their guidance. Their enthusiasm, help, advice, and insight has been invaluable to me.

I wish to express my appreciation to Raúl, who first brought me into the world of research and with whom I began to learn about astrophysics. He has also been a cornerstone in my professional development. Raúl, thank you very much for all the support you gave me. I am forever indebted to you!

Roberto, thank you for believing in me from the beginning, your help, and patience trying to get a scientist out of this student. Thanks for all your support during my stays in Italy. Thanks also to your family for their hospitality.

I am grateful to all of my Ph.D. comittee members: Dr. Vahram Chavushyan, Dr. José Ramón Valdés, Dr. Omar López Cruz, Dra. Irene cruz-González Espinosa, and Dr. José Guichard Romero for taking the time to serve on my thesis exam and have read this manuscript, providing helpful comments to improve it.

Also thank you to Enrico Piconcelli for helping me with the X-ray data.

So naturally, I am in debt to Astrophysics Department at the *Instituto Nacional de Astrofísica, Óptica y Electrónica* (INAOE) for their help during my studies. Thanks a lot to all the people of INAOE that directly or indirectly contributed to this work.

To my many office mates over the years, thanks for brightening my days and making coming to work more fun than it should be. Thank you all my friends for being there for me, always ready to give me patient support and to provide distractions when I needed it. I also express my gratitude towards all people I had the chance to meet in Italy who, beyond the professional relationship, offered me their friendship.

Financial support for this work was provided by *Consejo Nacional de Ciencia y Tecnología* (CONACyT) grant for Ph.D. studies #157846 and by the CONACyT project #45948.

I cannot finish without saying how grateful I am with my parents, Irma and Uris, for all the love and support they given me through my entire life. Particular thanks, of course, to Yedi, she will always be the best little sister. Finally, I must acknowledge my husband and

best friend, Oscar, without whose love, encouragement and editing assistance, I would not have finish this thesis. I love you like you wouldn't believe.

Yari Juárez López, October 2009.

CONTENTS

LIST OF FIGURES

LIST OF TABLES

CHAPTER 1

INTRODUCTION

1.1 Active Galactic Nuclei (AGNs)

AGNs are galaxies with very energetic central regions, due to either the presence of a black hole (BH) or star formation (SF) activity at the core. In general, AGNs have five main properties: (1) very compact angular size; (2) high luminosity ($\sim 10^{45}$ to $\sim 10^{48}$ erg s^{-1}); (3) Continuum emission from the core, meaning the objects emit radiation at a range of wavelengths from radio up to X-ray and Gamma; (4) emission lines; and (5) variability of the continuum and spectral line emission.

In the unification scheme for AGNs (Antonucci 1993; Urry & Padovani 1995) the central massive ($10^{6-10} M_{\odot}$) BH is surrounded by a cloud of gas and dust with the geometry of a torus. This torus is illuminated by the accretion disk (Figure 1.1). Matter pulled toward the BH loses angular momentum through viscous or turbulent processes in an accretion disk, which glows brightly at ultraviolet (UV) and perhaps soft X-ray wavelengths. Hard X-ray emission is also produced very close to the BH. Strong optical and UV emission lines are produced in clouds of gas moving rapidly in the potential of the BH, the so-called "broad-line clouds". Beyond the torus, slower moving clouds of gas produce emission lines with narrower widths. Outflows of energetic particles occur along the poles of the disk or torus, escaping and forming collimated radio-emitting jets. The plasma in the jets, at least on the smallest scales, streams outward at very high velocities, beaming radiation relativistically in the forward direction.

In AGNs, three different regions of ionized gas can be distinguished. The outermost

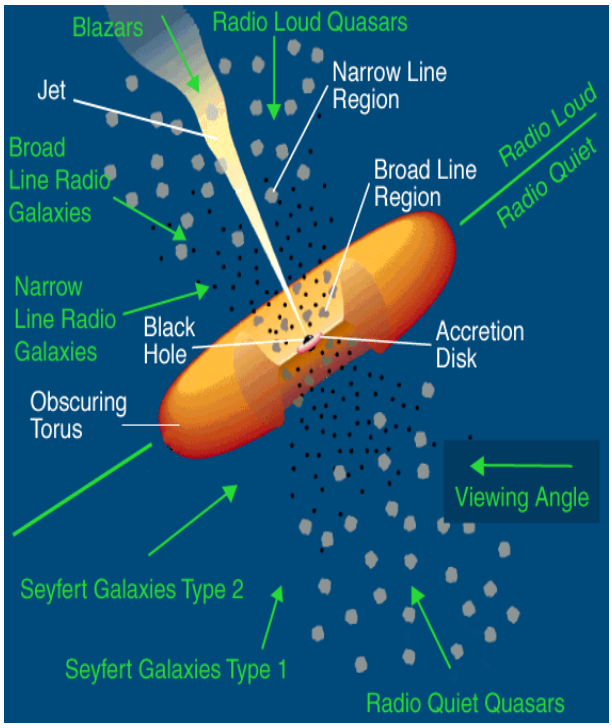

Figure 1.1: Schematic picture of the key elements of an AGN: central supermassive BH, accretion disk, BLR surrounded by a dusty torus or warped disk, NLR, and, at least for radio-loud AGN, a relativistically outflowing jet which originates near the BH.

region, the Extended Narrow Line Region (ENLR), has an electron density of $\sim 10^3\,\mathrm{cm}^{-3}$ and a radius of $\sim 10\,\mathrm{kpc}$, the spectral lines formed in this region have Doppler widths of $\sim 10^2\,\mathrm{km\,s}^{-1}$. The next region, the Narrow Line Region (NLR), located beyond the opening of the torus funnel, has an electron density of $\sim 10^5\,\mathrm{cm}^{-3}$, line widths of several hundred kilometers per second, and a radius of $\sim 1{-}100\,\mathrm{pc}$. The inner-most region, the Broad Line Region (BLR), located within the opening in the middle of the dust torus, has electron densities $> 10^9\,\mathrm{cm}^{-3}$ and emission line widths of several thousand kilometres per second. The size of the BLR in AGNs is $\sim 0.01{-}0.1\,\mathrm{pc}$. Sizes and morphologies of BLRs and NLRs provide an ideal probe of the distribution of dust and gas in the central parts of AGNs.

The central regions of many AGNs appear to contain obscuring material, probably in the form of dust, that prevents IR through UV light from penetrating some lines of sight. This dust may be distributed in a torus (Pier & Krolik 1993), which causes AGN to look markedly different from different aspect angles. From this arises to the separation into two spectroscopic groups (Type 1 and Type 2), depending on the presence or absence in their

optical spectra of broad emission lines.

Broad line, Type 1 AGNs are AGNs in which the line of sight to the nucleus is not blocked. They have bright continua and broad strong optical/UV emission lines. In narrow line, Type 2 AGNs the line of sight to the nucleus is blocked by the obscuring torus. These objects have weak continua and only the NLR is directly visible. Also, Type 2 AGN are defined as those that have absorbing column densities $N_H \geq 10^{22}\,cm^{-2}$ in the X-ray band. A small number of AGN have very unusual spectral characteristics called Type 0 AGN and they are related by a small angle to the line of sight (near 0 degrees). The unified model for AGN assumes that the Type 0, 1, and 2 are intrinsically the same class of objects, only seen at different angles with respect to the line of sight (Antonucci 1993).

Furthermore, the AGNs are also divided in terms of their radio power as the radio-loud and radio-quiet AGNs. Radio-quiet AGN tend to lack relativistic jets, releasing heat and light through accreting matter. In radio-quiet objects, their optical and radio luminosities are typically comparable. Radio-loud AGN possess relativistic jets and in the most luminous objects, blazars, these jets are pointing very close to the line of sight. In radio-loud objects the radio luminosities often exceed the optical by factors of $10^3 - 10^4$. Roughly 15−20% of AGN are radio-loud.

In fact, a wide range of objects are subsumed under the name AGN, all of which have in common strong non-thermal emission in the core of a galaxy (host galaxy). The classification of AGNs is described below.

Radio-Quiet AGNs:

- Low-ionization nuclear emission-line regions (LINERs). They are characterized by narrow emission lines from low ionization states or neutral atoms, such as OI, OII, NII, and SII, with only weak lines from highly ionized states. They constitute the lowest-luminosity class of radio-quiet AGN. Approximately 75% of LINER galaxies are either elliptical, lenticular, or spiral galaxies (Filippenko 2003).

- Seyfert galaxies, which have modest luminosities but tend to be the best studied since they are nearby. They show optical nuclear continuum emission, narrow and broad emission lines. Originally they were divided into two types known as Seyfert 1 and 2. Seyfert 1 have both very broad (up to $10^4\,km\,s^{-1}$) permitted and also narrower emission lines (several hundred $km\,s^{-1}$). Seyfert 2 galaxies differ from Seyfert 1 galaxies in that only the narrow lines are present in the spectra. The host galaxies of Seyferts are usually spiral or irregular galaxies (Osterbrock Donald E. 2006).

- Radio-Quiet Quasars. They are more luminous than their host galaxy and show very high redshifts. The optical/UV spectra are dominated by numerous strong and very broad emission lines, some of them emitted by highly ionized atoms. They always have strong optical continuum emission and X-ray continuum emission. Most quasars are brightest in their rest-frame near-UV. The host galaxies of quasars can be spirals, irregulars or ellipticals.

- Quasar 2. These are objects with quasar-like luminosities but without strong optical nuclear continuum emission or broad line emission. They have narrow permitted lines, powerful hard X-ray emission, and a high equivalent width Fe Kα line. Many quasars 2 are so highly obscured that they are hidden, even at hard X-rays (Sturm et al. 2006).

- Broad Absorption Line (BAL) quasar. These objects exhibit strong, broad and blueshifted spectroscopic absorption features (Weymann et al. 1991).

Radio-Loud AGNs:

- Radio-loud quasars. These behave exactly like radio-quiet quasars with the addition of strong radio emission which originates from jets of matter moving close to the speed of light. Thus, they show strong optical continuum emission, broad and narrow emission lines, and strong X-ray emission, together with nuclear and often extended radio emission (Wang et al. 2003). They reside in giant elliptical hosts.

- Blazars (BL Lac objects and OVV quasars). These classes are strongly variable, showing flux variability from radio to γ-ray on a timescale from months and days to a fraction of an hour. They have high and variable optical polarization and flat radio spectra. BL Lac objects in general show no optical emission lines, broad or narrow, so that their redshifts can only be determined from features in the spectra of their host galaxies (Vermeulen et al. 1995). Optically Violent Variable (OVV) quasars behave more like standard radio-loud quasars with the addition of a rapidly variable component (Smith 1996). In both cases the host galaxies are giant ellipticals.

- Radio galaxies. These objects show nuclear and extended radio emission. They can broadly be divided into broad-line radio galaxies (BLRGs) and narrow-line radio galaxies (NLRGs). BLRGs show broad optical emission lines. BLRGs are not generally obscured by large amounts of circumnuclear cold gas and, as a consequence, offer a direct view of their inner regions (Dennett-Thorpe et al. 2000). NLRGs include two

distinct morphological types: the low-luminosity Fanaroff-Riley type I (FR I) radio galaxies, which have often-symmetric radio jets whose intensity falls away from the nucleus, and the high-luminosity Fanaroff-Riley type II (FR II) radio galaxies, which have more highly collimated jets leading to well-defined lobes with prominent hot spots (Baum et al. 1995; Fanaroff & Riley 1974). The host galaxies are almost exclusively large elliptical galaxies.

Table 1.1 shows the main classes of AGN, organized according to their radio-loudness and their optical spectra, i.e., whether they have broad emission lines (Type-1), only narrow lines (Type-2), or weak or unusual line emission. Within each of the groupings, different types of AGN are listed by increasing luminosity. Whether AGN are classified Type-1 or Type-2 depends on obscuration of the luminous nucleus and whether a radio-loud AGN is a blazar or a radio galaxy depends on the alignment of the relativistic jet with the observer's line of sight.

Table 1.1: Main classes of AGN: A Simplified Scheme

Radio Loudness	**Optical Emission Line Properties**		
	Type 2 (Narrow Line)	**Type 1** (Broad Line)	**Type 0** (Unusual)
Radio-quiet:	LINERs Seyfert 2 Quasars 2	Seyfert 1 Quasars	BAL quasar?
Radio-loud:	NLRG { FR I, FR II }	BLRG Quasars	Blazars { BL Lacs, OVV quasars }

1.2 The circumnuclear region in AGNs

1.2.1 Metallicity diagnostic in Quasars

Among the AGNs, quasars are the most distant and extremely bright objects in the universe. They were first identified as being high redshift sources of electromagnetic energy, including radio waves and visible light that were point-like. All observed spectra have shown

considerable redshifts, ranging from 0.06 to the recent maximum of 6.4. Quasars are found to vary in luminosity on a variety of timescales. The *Sloan Digital Sky Survey* (SDSS) has uncovered the most distant quasars known, up to $z \sim 6.4$ (Fan et al. 2001, 2003, 2004, 2006).

The exceptional luminosities of quasars allow us to study the properties of gas and dust in their circumnuclear region in the highest redshift systems discovered so far ($z \sim 6$). High redshift quasars provide direct probes of the distant early universe when the first generation of galaxies and quasars formed. Among the characteristic properties of quasars are the prominent emission lines from the gas ionized and heated by a central radiation source. Assuming that this gas originates from the interstellar medium (ISM) of the quasar host galaxies, line diagnostics applied to the most prominent emission lines provide an important tool to study both the chemical composition and enrichment history of the quasar host galaxies (Hamann & Ferland 1999).

The spectra of the highest redshift quasars are very similar to those of quasars in the local universe (Fan et al. 2004), suggesting that chemical enrichment of their enviroments operates on short cosmological timescales. The quasar environments are typically metal rich, with metallicities near or above the solar value at even the highest observed redshifts (Dietrich et al. 2003a; Freudling et al. 2003; Maiolino et al. 2003). The optical/X-ray flux ratios and X-ray continuum shapes show little evolution with redshift (Shemmer et al. 2005). These measurements show that quasar accretion disks and emission line regions are formed on very short timescales and that their properties are not sensitive to the cosmic age.

The elemental abundances near quasars can be inferred from a variety of spectroscopic observations, each providing unique information, so it is important to consider all of them.

- **Broad Emission Lines (BELs).** BELs are seen in most AGNs and are known to be formed in close proximity to the nucleus (within 0.01−0.1 pc). One great advantage of the BELs for quasar abundance work is that they are relatively easy to measure in a large number of objects. Their emission line ratios show solar or supersolar metallicity in high redshift quasars, as found in low redshift quasars (Barth et al. 2003; Dietrich et al. 2003b; Freudling et al. 2003; Maiolino et al. 2003). However, BELs abundance studies are only relative, in the sense they do not measure directly the ratio of heavy elements to hydrogen.

  Photoionization models (Hamann & Ferland 1993, 1999; Ferland et al. 1996) show that various emission line ratios provide reliable estimates of metallicity in the BLRs of quasars. Strong permitted line ratios, such as NVλ1240/CIVλ1549,

NVλ1240/HeIIλ1640, are sensitive to the metallicity if nitrogen behaves as a secondary element and therefore its abundance scales quadratically with metallicity, i.e., $\mathrm{N/H} \propto (\mathrm{O/H})^2 \propto Z^2$. Other metallicity diagnostic is the FeII(UV)/MgIIλ2800 emission line ratio which is considered a probable indicator of the Fe/α-elements abundance ratio. Fe abundance is of particular interest (Hamann & Ferland 1993, 1999), since most of the Fe in the solar neighborhood is generated by Type Ia supernovae (SNe Ia), whose precursors are believed to be long-lived intermediate-mass stars in close binaries; so appreciable Fe enrichment can only happen on a timescale of 1 Gyr after the initial starburst. On the other hand, the production of α-elements such as Mg and O is dominated by supernovae (SNe) of types II, Ib, and Ic, which explode very soon after the initial burst. Therefore, the Fe/α ratio is expected to be a strong function of age in young systems, and thus putting a useful constraint on the age and chemical enrichment timescale of the gas in the quasar environment.

More recently, Nagao et al. (2006b) showed that the (SiIVλ1398+OIVλ1402)/CIVλ1549 (hereafter (SiIV+OIV)/CIV) ratio is a tracer of the BLR metallicity, mainly because the relative importance of CIV as a coolant decreases when the BLR metallicity increases. This ratio has the advantage of not relying on the assumption $\mathrm{N/H} \propto (\mathrm{O/H})^2$. Moreover, (SiIV+OIV) and CIV are well isolated features which do not require difficult deblending techniques and can be measured even in low resolution spectra.

- **Narrow Emission Lines (NELs).** The well-known NELs at rest-frame visible wavelengths have not yet been used to estimated the abundances in high redshift quasars because they are shifted into the near-infrared (NIR) and are thus more difficult to measure. However, there have been several studies of these lines in low redshift AGNs. Photoionization models and standard line ratios such as [OIII]λ5007/Hβ and [NII]λ6583/Hα have been used to infer NEL region metallicities (Groves et al. 2006), revealing that the metallicity of the NLR is generally lower than typically observed in the BLR, but still solar or supersolar. Nagao et al. (2006a) examined high redshift AGNs having only narrow lines using the flux ratios of CIVλ1549/HeIIλ1640 and CIII]λ1909/CIVλ1549, which are a powerful diagnostic to probe the metallicity of the NLR. They found a wider range of NELs metallicities, from 0.2 to $5Z_{\odot}$. They note that the results depended on the assumed gas density.

- **Associated Absorption Lines (AALs).** Quasar absorption lines provide another opportunity to measure the element abundances. Most of the work in this area has been

on the narrow "associated" absorption lines because: *i)* most of them are physically related to the quasar or its host galaxy, and *ii)* the line profiles are narrow enough to resolve important doublets, such as CIV$\lambda\lambda$1549,1551. In principle, the absorption line analysis is much simpler than the emission lines because it is only necessary to measure the ionic column densities and to apply ionization corrections in order to derive abundance ratios. The absorption line studies have found solar or supersolar metallicities even for what concerns the carbon abundance, consistent with the emission line data (Hamann & Ferland 1999; Gabel et al. 2006).

1.2.2 Dust emission in Quasars

Dust is the cornerstone of the AGN unified scheme that postulates that the diversity of the observed properties of AGN are merely a result of the different lines of sight with respect to obscuring material surrounding tha active nucleus (Antonucci 1993; Urry & Padovani 1995). The necessary elements for understanding the nature of AGN and the variety of their properties are the geometry of the circumnuclear dust and the amount of obscuration.

Dust plays a crucial role in the evolution of the early universe: $\sim 50\%$ of optical radiation emitted since the Big-Bang by all astrophysical sources has been "reprocessed" by dust. Dust is regarded as an efficient ISM coolant (Lehner et al. 2004), thus controlling accretion and profoundly influencing star formation rates, especially for massive stars. On cosmological scales, thermal emission from high redshift dust dominates the FIR background radiation and can even distort the cosmic microwave background (Elfgren & Désert 2004). There are indications of the presence of dust in high redshift Lyman-break galaxies (Ando et al. 2004) and quasars (Beelen et al. 2006; Bertoldi et al. 2003a; Maiolino et al. 2004; Priddey et al. 2003b; Wang et al. 2008), which may have serious implications for the estimated SFR.

Dust grains in the early universe have great impact on the formation processes of stars and galaxies. Dust grains control the chemistry of the ISM by involving a large fraction of refractory elements and by serving as catalysts for chemical reactions of gas. Dust grains also influence the thermal balance in the interestellar space by producing photoelectrons that heat the gas and by reemitting the absorbed stellar light at IR wavelengths. The spectral properties of the IR emission from dust allow to infer its composition, the size distribution of the dust particles, the intensity of the starlight dust is heating, and the total dust mass.

Dust is important at high redshift for three reasons. First, intrinsic luminosities and SFRs are always underestimated when dust is not taken into account; this may have vast

implications for metal production at early epochs. Second, dust may hide entire populations of high redshift star forming galaxies from detection because of sample selection effects. And third, dusty ISM in galaxies at $z > 3$ imply previous episodes of star formation and enrichment, pushing the first epoch of star formation to even higher redshifts.

According to the classical scenario, dust in the ISM is mostly formed in the envelopes of low- and intermediate-mass AGB stars which take about 1 Gyr to evolve (Morgan & Edmunds 2003). As a consequence, small amounts of dust are expected to be present at $z > 5$, when the universe was younger than 1 Gyr. However, deep submm/mm observations have detected FIR thermal emission from warm dust in several quasars and galaxies at redshifts $z \geq 5$, tracing large amounts of dust with masses in excess of $10^8 - 10^9 M_\odot$ (Bertoldi et al. 2003a; Priddey et al. 2003b; Beelen et al. 2006), which implies a rapid enrichment of the ISM with dust in such young systems. One possible explanation is that the dust is produced in the ejecta of core-collapse (e.g. type II) SNe ($M > 8 M_\odot$), which evolve on short time scales ($t < 20$ Myr) and therefore provide a rapid mechanism of dust enrichment (Maiolino et al. 2004; Dwek et al. 2007). Elvis et al. (2002) have proposed an alternative mechanism for dust production in the early universe, based on the possible condensation of a large amount of dust in quasar winds, while it is suggested that the formation of dust in AGB stars can dominate over contributions from SNe even at $z = 5$. Possibly, both SNe and quasar winds may contribute to the dust enrichment in the early universe. The large dust masses and massive dense gas reservoir found in high redshift quasars, including sources at the end of reionization, provide direct evidence that vigorous SF is co-eval with the rapid growth of massive BHs up to the earliest epochs of the universe.

On the other hand, the rest-frame NIR photometry of quasars at $z > 5$ with *Spitzer* (Jiang et al. 2006) have confirmed the existence of hot dust heated by the central active nuclei. This indicates the fundamental structures of quasars such as accretion disks and hot-dust tori had been already established during the first billion years of cosmic history. However, the origin and nature of dust in the high redshift universe are not necessarily the same as those in our Galaxy. About this, Maiolino et al. (2004) have found that the rest-frame UV extinction curve observed for the quasar SDSS J1048+4637 at $z = 6.2$ is quite different from those in local galaxies, suggesting that the source and evolution of dust at high redshift ($z > 5$) are different from those at low redshift ($z < 4$).

1.2.3 Dust and star formation in AGNs

The MIR and hard X-rays regions of the electromagnetic spectrum are of particular interest for the study of AGN. Hard X-rays can provide a direct view of the central engine, since they are almost uncontaminated by SF processes. The nuclear IR continuum is due to AGN emission reprocessed by dust, either in the putative torus or on somewhat larger scales, e.g. inside the NLR. Nonthermal IR emission is possibly connected to the X-ray emission, directly as part of a broad synchrotron component or as part of a radio-IR spectrum that Compton scatters to produce the X-rays. In general terms, measurements of the MIR continuum in combination with hard X-ray observations can be thought as testing unification scenarios for AGN.

AGNs are powered by accretion onto a massive BH. The observed relation between BH mass and host bulge mass in AGNs suggests that nuclear activity is closely connected to SF. Obscuring dust, however, hampers studies of the optical–soft X-ray emission produced by young stars and the accretion disk. Emission at IR wavelengths does not suffer such large extinction, and furthermore, the dust that absorbs the shorter wavelength emission re-radiates in the IR and correspondingly produces a substantial fraction of the bolometric flux of the object. Analyzing the detailed IR spectral energy distribution of AGNs can reveal the properties of the dust in the nuclear region, as well as to put constraints on the optical–soft X-ray spectrum that heats the dust.

The MIR spectrum of AGNs contains a wealth of information which is crucial to the understanding of their inner region. The observed prominent continuum emission is due to the circumnuclear dust heated to a temperature of several hundred degrees by the nuclear primary optical/UV/X-ray source; therefore, the MIR continuum provides information on the amount of the circumnuclear dust. The MIR region is also rich in several emission features which are important tracers of the ISM. Among the dust features, the PAH bands (6.2, 7.7, 8.6, 11.3, and 12.7 μm), generally attributed to vibrational emission, arise in regions of the ISM of a galaxy where their aromatic carriers are present, and where their transient excitation is made possible by a non-ionizing (< 13.6 eV) soft UV radiation field. PAHs have been used as a quantitative tracer of SF activity. SF is a driving force behind galaxy evolution; it largely determines the stellar, energy (radiant and mechanical), metal, and dust content of a galaxy. MIR dust luminosities are ideal tracers of SF and can be widely used to estimated the star formation rate (SFR). In local sources, the presence of PAH features, combined with the shape of the continuum, can be used to determine the nature of the

emission (AGN vs. SF) that dominates the bolometric luminosity of a source.

Additional MIR dust features are the silicates bands, which produce two spectral features: a 10 μm feature that arises from a Si−O stretching mode, and 18 μm feature from an O−Si−O bending mode. It is known that most of type 2 AGNs display silicate absorption bands (Siebenmorgen et al. 2004; Hao et al. 2007; Spoon et al. 2007) which are expected from the AGN unified theory: for a centrally heated optically thick torus viewed edge-on, the silicate features should be in absorption. For type 1 AGN viewed face-on, the silicate features are in emission since the silicate dust in the surface of the inner torus wall will be heated to temperatures of several hundred degrees kelvin to $\sim$1000 K by the radiation from the central engine, allowing for a direct detection of the 9.7 and 18 μm silicate bands emitted from the hot dust (Hao et al. 2005; Siebenmorgen et al. 2005; Sturm et al. 2005; Weedman et al. 2005; Shi et al. 2006; Schweitzer et al. 2008).

1.3 Goals

The study of quasars requires observations from X-ray to radio wavelengths since the physical mechanisms observed in each spectral region allows to probe different regions of the active nucleus. In particular, the dust emission takes place in the IR, submm and mm bands, whereas the rest-frame UV spectrum, from the Lyα emission line to the FeII bump at 2000−3000 Å, contains strong diagnostic emission lines and provides key information on the physical conditions and emission mechanisms of the BLR. At high redshifts, the rest-frame UV lines are red-shifted to the NIR range, therefore it is necessary to carry out observations in IR, submm, and mm wavelengths.

On this thesis, based on IR and submm/mm observations, the goal is to study the evolutionary properties of AGNs by means of the metals, dust content and activity of SF in the host galaxies of these objects at high redshift. More specifically:

The metallicity evolution (§1.2.1) will be studied by analyzing the abundance of α-elements (SiIVλ1398+OIVλ1402) and CIVλ1549 in the most distant quasars ($z > 4$). For this part of the work, NIR and optical observations obtained with TNG+NICS and with VLT-ESO will be used. The NIR observations are necessary because, as it was mentioned before, for these redshifts the main emission lines are displaced to the NIR. The metallicity study using (SiIV+OIV)/CIV has the purpose of complementing other studies at high redshift regime and therefore, for early epochs in the cosmic evolution.

The submm/mm observations are important to study the dust properties in high redshift

quasars (§1.2.2). We select a sample of quasars in the redshift range $1.5 < z \leq 6.4$, by using submm/mm observations with the aim to study the implications on the relation between star formation and quasars, and on the evolution of dust mass at high redshift.

In order to continue the investigation of the dust properties in the circumnuclear region, we select an obscured AGN sample with observations in the MIR in order to study the MIR and hard X-ray luminosities, the strength of the $9.7\,\mu$m silicate feature as a function of HI column density, and SFRs (§1.2.3). This will allow us to investigate whether the circumnuclear dust absorption depends on the luminosity and SFR.

The thesis is organized as follows: in Chapter 2 we study the metallicity evolution of the most distant quasars. We present observations and data reduction, we discuss in detail the emission line measurements, and we present the results. In Chapter 3 we study the dust evolution in high redshift quasars. We present the sample selection, observations, and data reduction. We showed the analysis of the NIR spectra and the measurements of the FIR luminosity, as well as the results. In Chapter 4 we study the MIR and hard X-ray luminosities, silicates features and SFR in AGNs. We discussed the data acquisition and data reduction. We analyzed the silicate features in IRS spectra and we showed the results. Finally, in Chapter 5 we draw the final conclusions.

Throughout this thesis, we adopt a cosmological model with $\Omega_\Lambda = 0.7$, $\Omega_m = 0.3$, and $H_0 = 70\,\mathrm{km\,s^{-1}\,Mpc^{-1}}$.

CHAPTER 2

METALLICITY EVOLUTION

The spectra of high redshift quasars contain important information about the enrichment history of the gas in the quasar environment and can probe the star formation preceding the epoch at which the quasars are observed.

In particular, the rest-frame UV spectrum, from the Lyα emission line to the FeII bump at 2000−3000 Å, contains strong diagnostic emission lines and provides key information on the physical conditions and emission mechanisms of the BLR. The chemical abundances in the BLR are important for understanding the history of star formation in the host galaxy (Hamann & Ferland 1999).

One of the main results from studies of high redshift quasars, is the apparent lack of strong evolution in their rest-frame UV/optical and X-ray spectral properties. Their emission-line strengths and UV continuum shapes are very similar to low-redshift quasars (Fan et al. 2004; Pentericci et al. 2003). The emission-line ratios indicate solar or supersolar metallicity in the BLRs as it is found in low-redshift quasars. This is a direct evidence of rapid chemical enrichment process through multiple generations of star formation in the immediate environment of these luminous quasars (Dietrich et al. 1999, 2003a,b; Hamann & Ferland 1999).

At $z > 5$ most of the interesting emission lines used to constrain the BLR metallicity are redshifted into the NIR. As a consequence, the investigation of the BLR metallicity at $z > 5$ has been limited to a small number of objects. Some authors have investigated the iron abundance in $z \sim 6$ quasars by using NIR spectra to measure the intensity of the UV FeII bump relative to the MgIIλ2789 line (Dietrich et al. 2003b; Maiolino et al. 2003; Freudling et al. 2003; Iwamuro et al. 2004), as a proxy of the Fe/α-elements abundance

ratio. They found the FeII/MgII ratio to have roughly the same value at $z \sim 5$ as at lower redshift, suggesting the metallicity of quasar emission line region remains high to even earlier epochs. Nagao et al. (2006b) showed that the (SiIV+OIV)/CIV) ratio is a tracer of the BLR metallicity. (SiIV+OIV) and CIV are well isolated features, which do not require difficult deblending techniques, and which can be measured even in low resolution spectra. Jiang et al. (2007) used NIR spectra to measure (SiIV+OIV)/CIV in five quasars at $z \sim 6$, and found no evidence of evolution when compared with lower redshift quasars. These data give a strong constraint on the first epoch of active star formation in quasars host galaxies, especially when the minimum timescale required for the enrichment of some metals (C, N, Si, Fe) is taken into account.

This chapter is based on a paper published in the Astronomy & Astrophysics by Juarez et al. (2009) shown in Appendix A.

2.1 Observations and data redution

2.1.1 Sample selection

We selected a sample of 27 high redshift quasars ($4 \leq z \leq 6.4$) from the SDSS, which contains the valuable diagnostic UV rest-frame emission lines (e.g., SiIVλ1398+OIVλ1402, CIVλ1549, HeIIλ1640, CIII]λ1909) in order to study the chemical composition of the BELR gas and its implications on the star formation history in quasar host galaxies in the early universe.

The quasars were selected to be accessible at the time of observation and to be bright enough to be observed within reasonable integration times (see Table 2.1 for names, coordinates, and redshifts). The spectral wavelength range was chosen to cover the redshifted SiIVλ1398+OIVλ1402 to CIII]λ1909 emission lines.

2.1.2 Observations

The observations were obtained with telescopes: the Italian Telescopio Nazionale Galileo (TNG), a 3.56 m telescope, operated on the island of La Palma by the Centro Galileo Galilei of the INAF (Istituto Nazionale di Astrofisica) at the Spanish Observatorio del Roque de los Muchachos (ORM) of the Instituto de Astrofísica de Canarias and with Very Large Telescope (VLT) 8.2 m Antu telescope. The VLT was built and is operated by the European Southern Observatory (ESO), and is located at the Paranal Observatory on Cerro Paranal, a high mountain in the Atacama desert in northern Chile. Observations were performed in several

Table 2.1: Log of Observations

Name	R.A. (J2000)	DEC (J2000)	z[a]	Date	t_{exp} (minutes)
SDSS J000239.40+255035*	00 02 39.4	+25 50 35	5.80	2004 Jul 20,21,31	65,40,20
				2005 Jan 22	40
SDSS J000552.3-000656*	00 05 52.3	-00 06 56	5.85	2004 Aug 5,17	80,85
				2005 Sep 15,19	27,87
SDSS J001714.66-100055†	00 17 14.7	-10 00 55	5.01	2005 Dec 2	45
SDSS J012004.82+141108*	01 20 04.8	+14 11 08	4.73	2004 Aug 4,23	35,30
				2004 Sep 10	168
SDSS J015642.11+141944*	01 56 42.1	+14 19 44	4.325	2004 Sep 22,23	210,27
SDSS J023137.60-072855†	02 31 37.6	-07 28 55	5.413	2005 Dec 2	45
SDSS J023923.47-081005*	02 39 23.5	-08 10 05	4.023	2004 Sep 10	60
SDSS J033829.30+002156†	03 38 29.3	+00 21 56	5.00	2005 Dec 2	45
SDSS J075618.10+410408*	07 56 18.1	+41 04 08	5.07	2002 Nov 7	60
SDSS J083643.80+005453*	08 36 43.8	+00 54 53	5.80	2004 Feb 6	53
SDSS J085210.89+535948*	08 52 10.9	+53 59 49	4.22	2004 Oct 31	27
				2005 Jan 22	120
SDSS J095707.67+061059†	09 57 07.7	+06 11 00	5.157	2005 Mar 18	30
SDSSp J102119.16-030937†	10 21 19.1	-03 09 37	4.696	2005 Mar 18	30
SDSS J103027.10+052455*	10 30 27.1	+05 24 55	6.28	2003 May 24,25,26	54,27,30
SDSS J114816.60+525150*	11 48 16.6	+52 51 50	6.40	2003 May 23,25	62,63
SDSS J120441.70-002150†	12 04 41.7	-00 21 50	5.055	2005 Mar 18	30
SDSSp J120823.80+001028†	12 08 23.8	+00 10 28	5.273	2005 Mar 18	75
SDSS J130608.20+035626*	13 06 08.2	+03 56 26	5.99	2003 May 24,26	63,18
SDSS J141111.30+121737*	14 11 11.3	+12 17 37	5.93	2005 Apr 20	80
SDSS J160254.20+422823*	16 02 54.2	+42 28 23	6.07	2004 Jul 5,6	80,100
SDSS J160320.89+072104*	16 03 21.0	+07 21 04	4.385	2003 May 24	48
SDSS J161425.13+464028*	16 14 25.1	+46 40 29	5.313	2005 May 13	40
				2005 Jun 3	80
SDSS J162331.80+311201*	16 23 31.8	+31 12 01	6.22	2004 Jul 15,20,31	20,80,65
SDSS J162626.50+275132*	16 26 26.5	+27 51 33	5.20	2005 Jun 4	80
SDSS J163033.90+401210*	16 30 33.9	+40 12 10	6.065	2004 May 13	228
SDSS J220008.70+001744*	22 00 08.7	+00 17 44	4.77	2002 Nov 7,9	60,60
SDSS J221644.00+001348*	22 16 44.0	+00 13 48	4.99	2004 Jul 5,6,15	72,19,19

[a] Redshift taken from the NASA/IPAC Extragalactic Database (NED), * TNG Observations, and † VLT Observations.

observing runs from 2002 to 2005. All observations were obtained in low resolution modes. Such low resolution is excellent for the investigation of the quasar continuum shape, but also for the detection of broad emission lines.

TNG is an altazimuth telescope equipped with an active optics system. Its two Nasmyth foci host five instruments which are permanently mounted and operating. The observations at TNG were done with the Near Infrared Camera and Spectrometer (NICS), it is the TNG infrared multimode instrument which is based on a HgCdTe Hawaii 1024×1024 array. Its observing capabilities include imaging ($4.2' \times 4.2'$), high-throughput low resolution spectroscopy ($R = 50-500$), medium resolution spectroscopy (max-$R = 2500$), imaging polarimetry, spectropolarimetry, and when coupled to the adaptive optics module, nearly diffraction limited imaging (Baffa et al. 2001).

The VLT consists of four separate optical/infrared telescopes (Antu, Kueyen, Melipal, and Yepun telescopes). Each telescope provides one Cassegrain and two Nasmyth focus stations for facility instruments. The VLTs are equipped with a large set of instruments permitting observations to be performed from the near-UV to the mid-IR with the full range of techniques including high-resolution spectroscopy, multi-object spectroscopy, imaging, and high-resolution imaging. FORS2 is the visual and near UV FOcal Reducer and low dispersion Spectrograph 2 for the VLT. The instrument is designed as an all-dioptric instrument for the wavelength range from 3300 to 11000 Å including imaging and low to medium resolution spectroscopy modes, with a wide range of filters and grisms (see FORS user manual[1]). FORS2 is installed on the Antu telescope and is optimised for the red with a very low level of fringes thanks to a mosaic of two 2k×4k MIT CCDs (with 15 μm pixels) with a pixel scale of $0.125''$/pixel. Although it is operated with binning 2×2 as standard delivering a final pixel scale of $0.25''$/pixel. Furthermore the instrument allows multi-object spectroscopy with exchangable masks and offers HIgh Time resolution (HIT) mode in imaging and spectroscopy.

The observations at the TNG were obtained with NICS. In the IR, the background emission caused by the atmosphere and the telescope starts to predominate in the signal, preventing the objects of interest could be detected. Therefore, in order to eliminate the background noise and to be able to observe faint objects, the frames are taken alternatively by shifting the field, but always containing the object in ABBA sequence, where A and B stand for the first and second position on the slit along the spatial axis. In the spectroscopy observing mode of low resolution and high sensitivity, NICS uses an Amici prism as a dispersing element (Oliva 2003). The Amici disperser consists of two low-dispersion and one

[1] http://www.eso.org/instruments/fors/doc/

high-dispersion prisms arranged in the classical Amici configuration which disperses the light without deviating the central wavelength. The most remarkable feature of this system is its throughput: 88% average and 82% minimum transmission over the $0.8-2.4\,\mu$m spectral range, i.e., nearly 2 times higher than other more commonly used dispersers. This makes possible to obtain spectra covering the whole NIR in one shot. Ten quasars were observed with a $0\farcs75$ wide slit, and ten were observed with a $1''$ wide slit. The spectral resolution is $R\sim75$ ($0\farcs75$) or $R=50$ ($1''$), as it was in our case, and nearly constant over the whole wavelength range.

In addition, we observed three quasars by using the IJ grism to obtain the $0.9-1.45\,\mu$m, which provides an almost uniform dispersion of $5.5\,\text{Å}\,\text{pixel}^{-1}$ throughout this range, and a resolving power of $R=500$ with a $1''$ slit. For the wavelength calibration, exposures of argon arc lamps were obtained. Typical integration times ranged from ∼20 minutes to ∼3 hours. Several quasars were observed more than once on different nights to check for any instrumental or observational artifacts in the individual spectra. Before or after the exposure of each quasar, a nearby spectroscopic standard star was observed for flux calibration and to remove telluric absorption.

The spectroscopic observations at VLT were done with the FORS2 instrument in long-slit spectroscopy (LSS) mode. We used the ESO grism GRIS150I+27 providing a dispersion of $3.45\,\text{Å}\,\text{pixel}^{-1}$ and a resolving power R∼ 300 with a $1''$ slit in combination with the OG590+32 order separating filter, leading to the wavelength coverage of approximately 6000−11000 Å. The target was placed at different locations along the slit for each individual frame. For the wavelength calibration, exposures of HgCdHe+Ar arc lamps were obtained. Spectra of standard stars were observed each night for relative flux calibration, with exposure times of 10 seconds. For the quasars, the total exposure times are ranging from 30 to 75 minutes. These observations are mostly used to cover the short wavelength part of some of the quasar spectra not properly sampled by the NIR observations. However, we also specifically observed a few quasars without NIR data with the specific aim of measuring the (SiIV+OIV)/CIV ratio.

2.1.3 Data reduction

The two-dimensional spectra (quasars and standard stars) from both observatories were reduced using standard IRAF[2] procedures and additional supermongo routines written by

[2]IRAF (Image Reduction and Analysis Facility) is distributed by the National optical Astronomy Observatories in Tucson, Arizona, which are operated by the Association of Universities for Research in Astronomy,

us (mainly by R. Maiolino).

NICS Data Reduction. A previous process to the data reduction takes place for the NICS data. Due to a false connection between the electronic channels that simultaneously read the four sections of the array, the detected signal produces negative images ghost in the other three quadrants, therefore, cross-talking is corrected applying an algorithm in the pre-reduction phase. This program in Fortran eliminates most of the cross-talking effects produced by nonsaturated images.

After having corrected the images by cross-talking, the Amici spectra taken at different positions are pair-subtracted to remove most of the background (difference A−B frame), which results in a positive and a negative spectrum of the object in the same image. Then we reviewed where the spectrum is saturated to trim the image. In order to produce a combined spectrum from each set of frames, we aligned them and added the aligned frames. Later, the unidimensional spectrum is extracted, converting it to ASCII format.

Due to the low resolution of the Amici disperser, all the lines of argon/xenon are mixed and cannot be easily used for procedures of standard reduction. Therefore, the wavelength calibration takes place using a table of data based on theoretical predictions and adapted to the best fit of the observed spectrum of the calibration lamps.

The telluric absorption was then removed by dividing the quasar spectrum by a standard star spectrum observed at similar airmass. The intrinsic features and slope of the standard star were then removed by multiplying its spectrum by a spectrum of the same stellar type from the library by Kurucz (1993), smoothed to our resolution. Finally, a supermongo program is used, which reads the quasar and standard star information in ASCII format, in order to obtain the calibrated spectrum in wavelength and flux. This program displays the final spectrum, showing in the top part of the spectrum the atmospheric transmission.

The data reduction for IJ spectra is very similar to the Amici spectra, the difference is in the wavelength calibration which is performed by using an argon arc lamp before the frames are aligned and combined.

FORS2 Data Reduction. For the FORS2 spectra, the object was observed in two positions along the slit. The sky emission lines are removed by subtracting the resulting spectra from each other. Later, the two-dimensional spectra are trimmed. The spectra are flat-fielded using dome flats. These flats are then averaged together with a minimum-

Inc., under cooperative agreement with the National Science Foundation.

maximum rejection to obtain the final flat, which is then normalized. Each spectrum is divided by this flat. The wavelength calibration is done using argon spectra obtained in the same slit configuration as the observations. The data are corrected for bad pixels, are aligned, and then co-added. One-dimensional spectra are extracted from the combined images.

The data of the standard stars of both observatories are reduced using the same procedures as for the science targets. The objects observed in differents nights were averaged according to the signal−to−noise ratio in the continuum.

For some of the $z < 5$ quasars observed with NICS, for which no FORS2 observations were available, we combined our NIR spectra with optical data taken from Anderson et al. (2001).

2.2 Emission line measurement

In order to measure emission line fluxes, the quasar spectra were fitted with a model consisting of a power-law continuum and gaussians to model the emission lines. In the following we detailed for each contribution the way in which they were measured and eliminated.

Nonstellar Continuum. The dominant component in the spectra is the continuum, which is usually modeled as a power-law

$$F_{\rm cont}(\lambda) = k\lambda^{\beta}$$

where k and β parameters were determined minimizing the function

$$\chi^2 = \sum_{i=1}^{n} \left[\frac{(F_{\rm cont}(\lambda) - F_{\rm obs}(\lambda))^2}{n} \right]$$

F_{obs} is the object flux, $\beta = -2-\alpha$ is the spectral index, and k is the normalization constant. The errors of the fitted parameters were computed from the covariance matrix in the standard way.

The continuum was fitted using small spectral regions, which are free of detectable emission lines (1345−1355 Å, 1445−1455 Å, 1695−1704 Å, 1973−1983 Å). This continuum is subtracted from the spectrum.

Broad Emission Lines. The CIV and SiIV+OIV emission lines were fitted with one symmetric gaussian profile. It is important to note that the SiIV+OIV are unresolved and are fitted with a single gaussian. Lyα was not included in the fits since it is not of interest for the estimation of the metal abundances.

After continuum sustraction, the emission lines were fitted as follow:

$$F_{\mathrm{Gauss}}(\lambda) = I_0 e^{\left[-0.5\left(\frac{\lambda-\lambda_c}{\sigma}\right)^2\right]}$$

where

$$\sigma = \frac{FWHM}{2\sqrt{2\ln 2}} = \frac{FWHM}{2.3}$$

with an initial FWHM of $2000\,\mathrm{km\,s^{-1}}$.

During the fitting of the line profile, the amplitude (I_0), FWHM (σ), and central wavelength (λ_c) of the gaussian are treated as free parameters. The best fit of the emission lines was determined with a χ^2 test.

$$\chi^2 = \sum_{i=1}^{n} \left[\frac{(F_{\mathrm{Gauss}}(\lambda) - F_{\mathrm{obs}}(\lambda))^2}{n}\right]$$

Then, we calculated the fluxes for CIV and SiIV+OIV. The total flux is given by

$$F = \int_0^\infty F_{\mathrm{Gauss}}(\lambda) d\lambda$$

approximating this integral we have

$$F_{\mathrm{line}} \approx F_{\mathrm{Gauss}}(\lambda)\Delta\lambda$$

Five of our sources are broad absorption line (BAL) quasars, for them the measurement of the emission line flux is more complex and uncertain because of the absorption trough. Absorption troughs are avoided when fitting both the continuum and the emission lines.

As an example, Figure 2.1 shows the flux calibrated spectrum of the quasar SDSS J0002+2550 at $z = 5.80$. The green solid line indicates the best fits to the emission lines, and the green dashed line indicated the best model fit to the power-law continuum. The red line indicates the sum of all components. The residual, subtracting the best fit from the quasar spectrum, is displayed at the bottom of each plot. In Appendix A, we showed the spectra for all the quasars of the sample.

2.3 Results

Emission-line ratios can be used to measure gas metallicity in the quasar BLR and track the chemical evolution with redshift.

Nagao et al. (2006b) used more than 5000 quasars spectra from the SDSS data realease 2 (DR2) to study the metallicity of the BLR. They made quasar composite spectra in the range

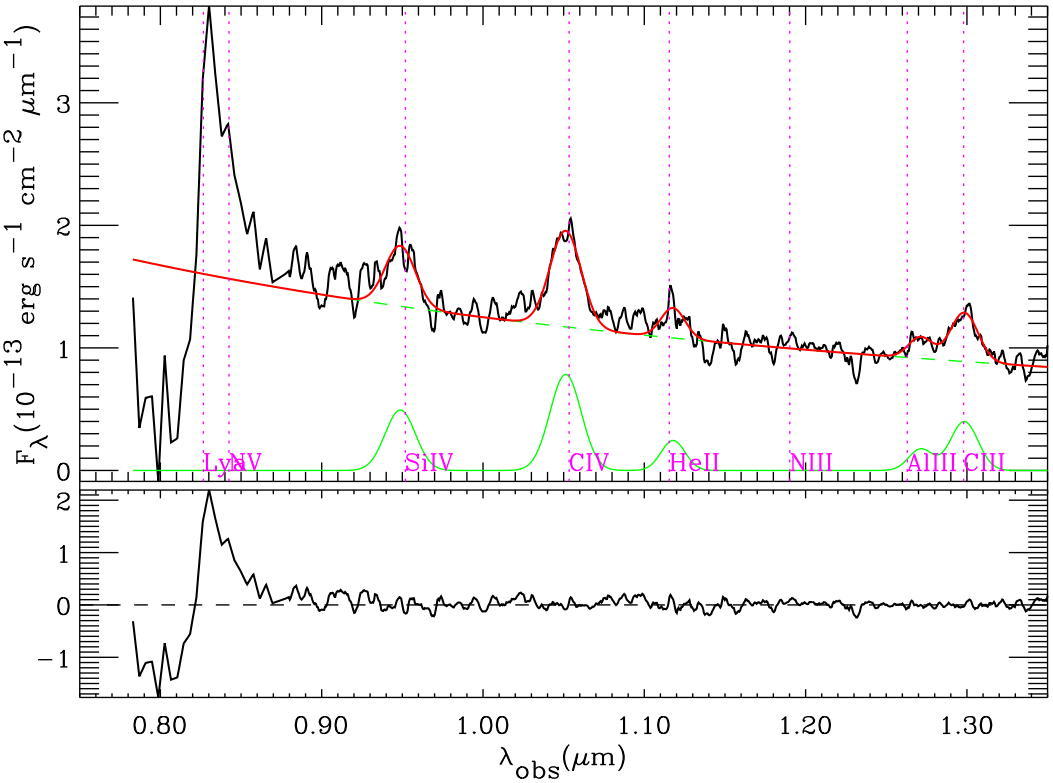

Figure 2.1: Near-IR spectrum of the quasar SDSS J0002+2550 at $z = 5.80$. (*Upper.*) The quasar spectrum is shown together with the power law continuum fit and the gaussian components to fit the emission line profiles. The resulting fit is overplotted as a red solid line. (*Lower*) Residual of the model fitting.

$2 < z < 4.5$ and over the luminosity range -24.5 $< M_B <$ -29.5 in order to measure emission line ratios and metallicities in the composite spectra for each redshift and luminosity bin. They found that most of the line ratios they investigated do not show strong evolution with redshift.

As suggested by Nagao et al. (2006b), emission line ratio of SiIV+OIV to CIV can be used as a new diagnostic tool of the metallicity of BLR in quasars, because this ratio is a good metallicity tracer of the BLR, since the relative importance of CIV as a coolant decreases with the BLR metallicity (Ferland et al. 1996). The ratio of (SiIV+OIV)/CIV is useful for determining the abundance pattern at early epochs. The α-elements, such as oxigen, can be enriched on a very short timescale ($<< 1$ Gyr) owing to SNeII; the silicon is largely

produced by SNeIa and therefore it is also probably enriched with a delay. However, Nagao et al. (2006b) found in their high resolution spectra that probably most of the emission in the SiIV+OIV blend is mostly due to OIV. The C enrichement require longer timescale ($\sim 0.5-1$ Gyr) since it is largely produced in low- and intermediate- mass stars.

2.3.1 The quasar metallicity evolution

Following Nagao et al. (2006b), we used (SiIV+OIV)/CIV ratio as the BLR metallicity indicator for our sample. The advantage of (SiIV+OIV)/CIV relative to the more commonly used NV/CIV as a tracer of metallicity, is that the former does not require detailed deblending of the lines (in contrast to NV+Lyα) and can be easily obtained even with low resolution (hence higher sensitivity) spectra.

We calculated emission line fluxes from the model fitting results described in §2.2. The measured (SiIV+OIV)/CIV ratios for the quasars in our sample are given in Table 2.2, along with their redshift and continuum luminosity (λL_λ) at 1450 Å.

In Figure 2.2 (top panel) appears the measured (SiIV+OIV)/CIV ratios as a function of redshift. According to the calibration given in Nagao et al. (2006b), the observed ratios correspond to metallicities several times solar. As can be seen, there is no correlation between the emission line ratio (hence metallicity) and redshift. Also, there is obviously no strong indication for an evolution of the (SiIV+OIV)/CIV ratio from $z \simeq 4$ up to $z \simeq 6.4$.

In order to investigate the evolution of the (SiIV+OIV)/CIV ratio over a wide range in cosmic time, we compared our results with data at low redshift. Also, in Figure 2.2 (bottom panel) the average of the (SiIV+OIV)/CIV ratios is shown in two redshift intervals ($4.0 \leq z < 5.5$ and $5.5 \leq z \leq 6.4$), together with the (SiIV+OIV)/CIV ratio obtained by Nagao et al. (2006b) from the SDSS composite optical spectra of quasars at $2 < z < 4$ and the luminosity range -28.5$< M_B <$-29.5. It is important to use quasars with similar luminosities, since quasar metallicities show a strong correlation with luminosity. Given that, at different redshifts magnitude limited surveys probe different luminosities, this may introduce an apparent redshift evolution; for this, from the $2 < z < 4$ templates in Nagao et al. (2006b) we select those in the highest luminosity bin (-28.5$< M_B <$-29.5), which match the quasar luminosities in our sample. As can be seen, the line ratio of $z \sim 6$ quasars appears to be consistent with those at redshift between 2 and 4, indicating little evolution in the metallicities, of quasars enviroments.

Another way to check this result can be done by inspecting Figure 2.3, which shows

Table 2.2: (SiIV+OIV)/CIV measurements

Name	z	(SiIV+OIV)/CIV	$\log\lambda L_\lambda^{a}$
SDSS J000239.40+255035	5.80	0.61±0.12	46.93
SDSS J000552.30-000656	5.85	0.34±0.06	46.20
SDSS J001714.66-100055.4[b]	5.0105	0.58±0.07	46.56
SDSS J012004.82+141108.2[b]	4.73	0.32±0.03	46.09
SDSS J015642.11+141944.3[b]	4.325	0.16±0.03	46.62
SDSS J023137.60-072855	5.413	0.29±0.07	46.56
SDSS J023923.47-081005.1[b]	4.023	0.23±0.04	46.58
SDSS J033829.30+002156	5.00	0.97±0.29	46.46
SDSS J075618.10+410408	5.07	0.80±0.15	46.53
SDSS J083643.80+005453	5.80	0.63±0.16	46.97
SDSS J085210.89+535948.9[b]	4.22	0.42±0.04	46.53
SDSS J095707.67+061059.5	5.157	0.69±0.14	46.65
SDSSp J102119.16-030937.2	4.696	0.35±0.12	46.58
SDSS J103027.10+052455	6.28	0.59±0.20	46.68
SDSS J114816.60+525150	6.40	0.41±0.08	46.95
SDSS J120441.70-002150	5.055	0.57±0.12	46.63
SDSSp J120823.80+001028	5.273	0.63±0.21	46.07
SDSS J130608.20+035626	5.99	0.38±0.19	47.32
SDSS J141111.30+121737	5.93	0.57±0.13	46.58
SDSS J160254.20+422823	6.07	0.53±0.17	46.90
SDSS J160320.89+072104.5	4.39	0.39±0.08	46.85
SDSS J161425.13+464028.9	5.313	0.34±0.03	46.62
SDSS J162331.80+311201	6.22	0.54±0.12	46.54
SDSS J162626.50+275132.4	5.20	0.30±0.09	46.94
SDSS J163033.90+401210	6.065	0.23±0.11	46.38
SDSS J220008.70+001744	4.77	0.55±0.07	46.58
SDSS J221644.00+001348	4.99	0.29±0.06	46.18

[a] Rest-frame luminosity at 1450 Å, in units of $\mathrm{erg\,s^{-1}}$.

[b] BAL quasar

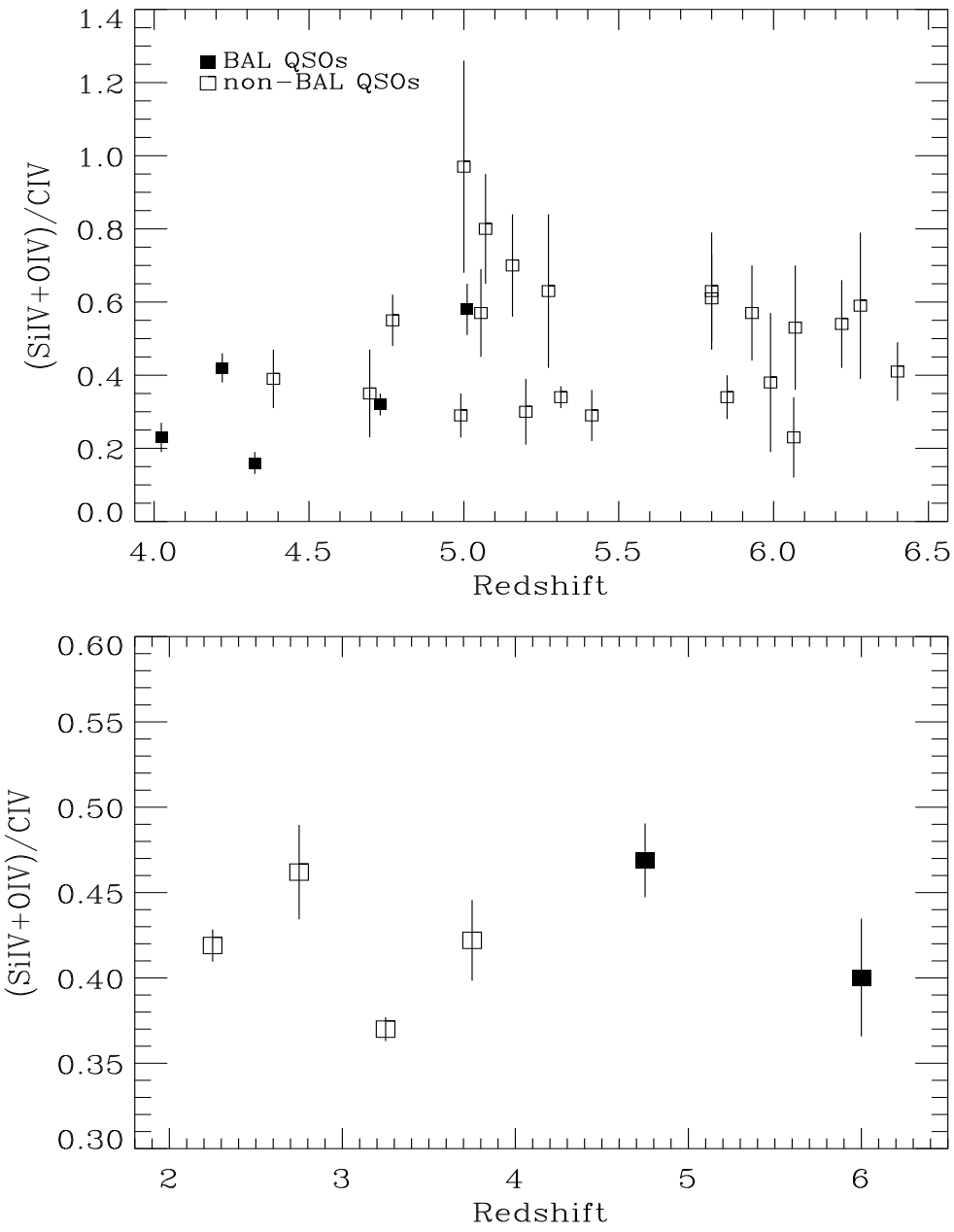

Figure 2.2: (*Upper*) (SiIV+OIV)/CIV flux ratio as a function of redshift for the quasars observed in this work. (*Lower*) (SiIV+OIV)/CIV ratio inferred from quasar stacked spectra (filled squares) and compared to low redshift quasars studied in Nagao et al. (2006b) in the luminosity range -28.5 $< M_B <$ -29.5 (empty squares).

the average spectra grouped in two redshift intervals ($4.0 \leq z < 5.5$ and $5.5 \leq z \leq 6.4$). In order to produce the stacked spectra, we first transformed the individual high redshift quasar spectra into the rest-frame using of the redshifts given in Table 2.2 (normalized to the continuum flux at 1500 Å). We removed the BAL quasars from our sample because the BAL features affect the profiles of broad emission lines in the average spectrum. These average spectra are remarkably similar, again highlighting lack of evolution. Small differences in Lyα and NV are due to different absorption of the intergalactic medium and to different spectral resolution of the spectra.

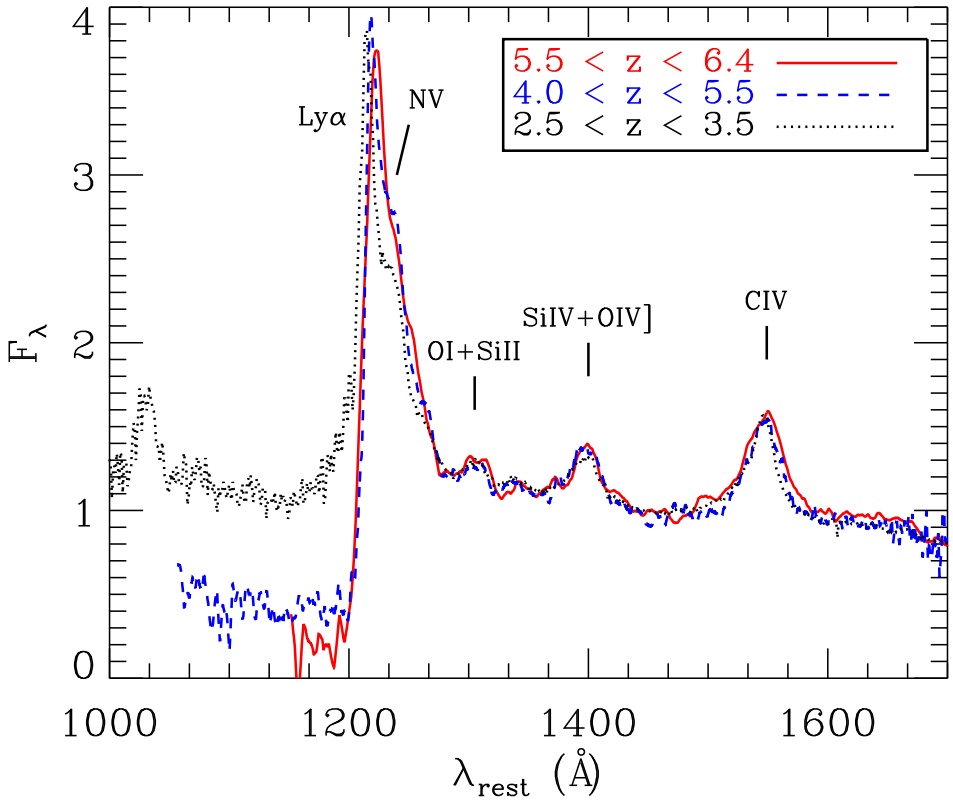

Figure 2.3: Stacked spectra of quasars obtained by grouping the objects in two redshift bins and by normalizing each spectrum to the continuum at 1500 Å prior to averaging. The blue dashed line and the red solid line are the stacked spectra from our sample in the redshift intervals $4.0 \leq z < 5.5$ and $5.5 \leq z \leq 6.4$. For comparison, we also plot the low redshift SDSS quasar stacked spectrum in the redshift interval $2.5 \leq z < 3.5$ (Nagao et al. 2006b).

Comparing the spectra, it can be seen the relative intensities of SiIV+OIV and CIV appear almost identical in the two redshift intervals. Moreover the averaged spectra at $z \sim 6$

are almost identical to the low redshift, as obtained by Nagao et al. (2006b). The quasar spectrum redward of Lyα emission shows no detectable evolution up to $z \sim 6$, neither on the spectral slope nor on the emission line strengths. The strength of emission lines remains roughly constant through cosmic history indicating that the metallicity and the chemical composition of the gas in the BLR do not evolve significantly over the whole redshift. In other words, the emission line region structure is not a function of redshift, and is not affected by cosmic environment.

Our analysis shows there is no apparent dependence of emission line flux ratio on redshifts up to $z \sim 6$, which is consistent with the results presented by Nagao et al. (2006b) and Jiang et al. (2007). The (SiIV+OIV)/CIV ratio at high redshifts shows similar value compared with those measured in low redshift quasars ($z \sim 2$). In consequence, the chemical composition of the gas clouds in the BLR does not change significantly up to $z \sim 6$. The observed lack of evolution of the (SiIV+OIV)/CIV emission ratio suggest the observed relative abundance of (SiIV+OIV)/CIV at $z \sim 2$ is already achieved at redshifts $z \sim 6$. The nearly constant (SiIV+OIV)/CIV ratio over cosmic time has important implications for the star formation history, particularly at high redshifts since the age of the Universe is ~ 1 Gyr (for redshifts $z \sim 6$), and approaches the enrichment time scale of low-mass stars and SNeIa.

The lack of evolution observed in Figures 2.2 and 2.3 should not be interpreted as a lack of evolution of the BLR metallicity in individual AGNs. Certainly, Figure 2.2 shows the average metallicity of the BLR in quasars which are accreting at the given redshift, but does *not* trace the evolutionary path of individual quasars. The aparent lack of evolution in the BLR metallicity observed in Figure 2.2 is likely a result from a combination of the BH-galaxy co-evolution and of selection effects. Indeed, to cross the detection threshold of the SDSS magnitude limited survey, high redshift quasars must have high luminosities, hence high black hole masses. High black hole masses must have been accompanied by the formation of a massive host galaxy. This is expected by most models of BH-galaxy co-evolution (Granato et al. 2004), in the attempt of explaining the local $M_{\rm BH} - M_{\rm spheroid}$ relationship. Therefore, by the time a quasar at any redshift is detectable in a magnitude-limited survey, its host galaxy must have evolved significantly, and enriched significantly its ISM. The quasar feedback is another evolutionary effect may yield to observational biases resulting into an apparent lack of metallicity evolution. Indeed, according to many models, during the early phases when the host galaxy is still metal poor, the accreting black hole is embedded within the dusty ISM, and therefore difficult to detect in optical surveys. Only during the late evolutionary phases, when the galaxy is already metal rich, the quasar develops winds powerful enough to

expel large quantities of gas and dust, so the quasar becomes visible to optical observations.

The observed (SiIV+OIV)/CIV imply very high metallicities in the BLR of luminous, high redshift quasars. According to Nagao et al. (2006b), the (SiIV+OIV)/CIV ~ 0.4 observed in the stacked spectrum of the most distant quasars corresponds to a gas metallicity of $\sim 7\,Z_{\odot}$. Such huge metallicities were also inferred by Nagao et al. (2006b) based on a much wider set of lines of lower redshift quasars. In fact, the BLR is a small nuclear region (size less than a few pc in the most luminous quasars) with masses of a few times ($\sim 10^4\,M_{\odot}$), which can be enriched to super-solar metallicities within less than 10^8 yrs by having less than a SN explosion every 10^4 yrs. More troublesome is the fact that such high metallicities are not found in the stellar population of local massive galaxies, not even in their central regions. Therefore, the high metallicity gas observed in the BLR of high redshift quasars must be either expelled, or diluted by lower metallicity gas in the host galaxy before forming stars.

The observational result that the (SiIV+OIV)/CIV ratio does not evolve suggests that the abundance of carbon relative to silicon and oxygen also does not evolve significantly. Large carbon abundances in the hosts of the most distant quasars is also suggested by the detection of strong [CII]158 μm and CO lines in the most distant quasars (Maiolino et al. 2005; Bertoldi et al. 2003b). Carbon is mostly produced by AGB stars and Planetary Nebulae, most of which evolve on long timescale. Although the first AGB stars appears as soon as ~ 50 Myr after the onset of star formation, the bulk of carbon production occurs after about 1 Gyr, yielding a delayed enrichment with respect to α-elements (e.g. oxygen) that are promptly produced by SNeII.

The fact that the ratio (SiIV+OIV)/CIV does not evolve with redshift, out to $z = 6.4$, suggests that the abundance of carbon relative to the α-elements does not evolve, contrary to the expectation that the carbon abundance should drop at $z > 5$ because stellar evolution may fall short of time to produce the observed large carbon abundance.

2.3.2 (SiIV+OIV)/CIV as a function of luminosity

In this section we tried to verify if the abundance as function of redshift have luminosity effects, since in some magnitude limited samples L and z are found associated.

We have derived monochromatic luminosities for our quasar sample at the rest-frame 1450 Å band using our NIR and optical observations. The continuum luminosity $\lambda L_{\lambda}(1450\,\text{Å})$ is calculated from its flux (f_{1450}) by the following formula:

$$\lambda L_{\lambda}(1450) = 4\pi d_L^2 \lambda_{\rm obs} f_{1450}(\rm obs),$$

where d_L is the luminosity distance. For a flat universe,

$$d_L = c(1+z)H_0^{-1}\int_0^z dz[(1+z)^2(1+\Omega_M z) - z(2+z)\Omega_\Lambda]^{-1/2},$$

where c is the speed of light, H_0 is the present Hubble constant, Ω_M is the mass density and Ω_Λ is the vacuum density (Hogg 1999).

Figure 2.4 (*upper*) represents the distribution of the $\lambda L_\lambda(1450\,\text{Å})$ depending on z. As it is possible to observe from the plot, the luminosity does not present a clear tendency to vary with z value, which indicates the luminosity does not decrease with the distance.

In order to study the dependence of the (SiIV+OIV)/CIV ratio with the luminosity, we analyzed our quasar sample, which spans about 1 order of magnitude in luminosity. In Figure 2.4 (*lower*), the (SiIV+OIV)/CIV ratios measured are displayed as a function of the continuum luminosity $\lambda L_\lambda(1450\,\text{Å})$. No trend of the (SiIV+OIV)/CIV ratio with luminosity was found within the luminosity range. This figure suggest the most luminous quasars are not those having the highest abundances.

2.3.3 Implications in the star formation and evolution of galaxies

We do not find evidence for any evolution in the spectral properties in our quasar sample. The lack of metallicity evolution is observed even in the spectra of the most distant quasars known ($z \sim 6$).

Our results can be explained with the models of rapid and strong star formation at high redshift as suggested by Matteucci & Padovani (1993). The authors proposed a model in which quasars are hosted by massive ellipticals, following in detail the evolution of several chemical species (C, N, O, Ne, Mg, Si, and Fe) in the gas. They assumed that after the ocurrence of a galactic wind, the galaxy evolves passively, and for masses $> 10^{11} M_\odot$ the gas restored by the dying stars is not lost but it feeds the central black hole. They showed that in this context, the stellar mass loss rate can explain the observed AGN luminosities. They also found solar abundances in the gas are reached in no more than 10^8 yrs, explaining in a natural way the standard emission lines observed in high redshift quasars. The predicted abundances could explain the data available at that time and solve the problem of the quasi-similarity of quasar spectra at different redshifts.

More recently, Maiolino et al. (2006) used more than 5000 quasar spectra from the SDSS data to investigate the metallicity of the BLR across the redshift range $2 < z < 4.5$ and over the luminosity range -24.5$< M_B <$-29.5. They found substantial chemical enrichment in

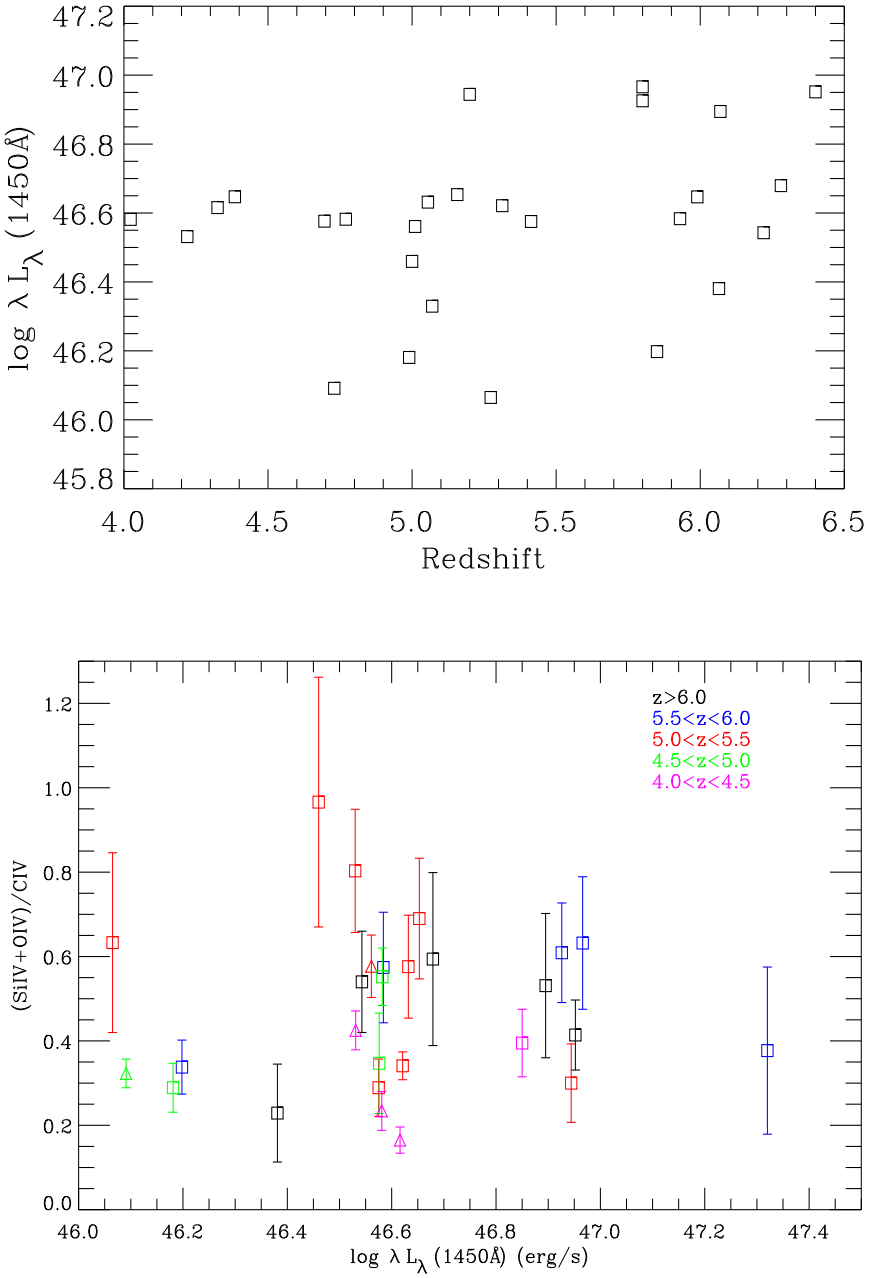

Figure 2.4: *Upper.* Luminosity as a function of redshift. *Lower.* (SiIV+OIV)/CIV ratios plotted as a function of continuum luminosity, $\lambda L_\lambda(1400\,\text{Å})$. Objects are color coded by redshift range, as indicated in the legend. Quasars and BAL quasars corresponding to squares and triangles, respectively.

quasars at $z \sim 6$. In addition, they show a very good agreement between their data set and the models for ellipticals developed by Pipino & Matteucci (2004) (Figure 2.5).

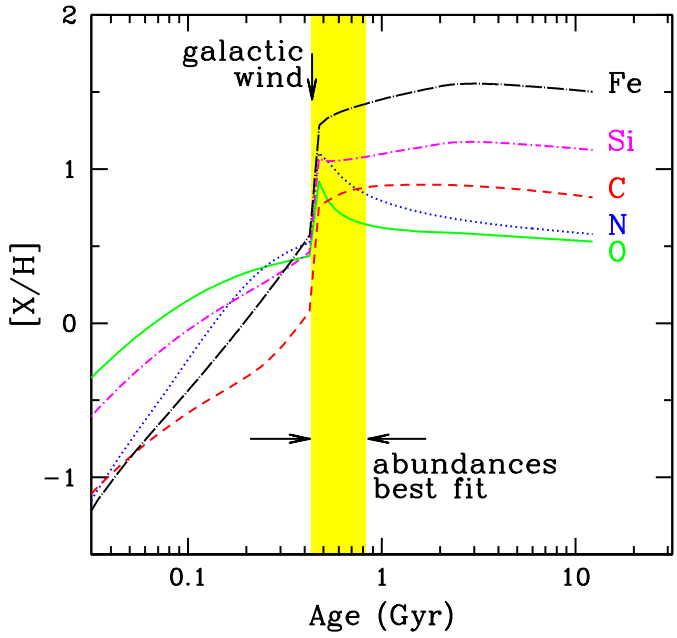

Figure 2.5: Abundances evolution of several chemical elements in the gas of an elliptical galaxy including feedback effects. The downward arrow indicates the time for the ocurrence of the galactic wind. All the abundances after the time for the ocurrence of the wind are those observable in the BELR. The shaded area indicates the abundance sets which best fit the line ratios observed in the quasar spectra. Figure from Maiolino et al. (2006).

Figure 2.5 shows the abundance evolution of several chemical elements in the gas of a massive elliptical galaxy. The ellipticals suffer a galactic wind at around 0.4 Gyr after the beginning of star formation. This wind devoids the galaxy of all the gas present at that time. After this time, the star formation stops and the galaxy evolves passively. All the gas can be restored after the galactic wind event, since dying stars can in principle feed the central black hole, thus the abundances shown in Figure 2.5, after the wind time, can be compared with the abundances measured in the BELR. The shaded area shows the range of abundances pattern that best match the line ratios observed in the quasar spectra. As we can see, the predicted Fe abundance after the galactic wind is always higher than the oxigen one, due to the SNIa which continues producing Fe, even after the SF stops. On the other hand, O and α-elements stop to be produced when the SF halts. The comparison

between the predicted abundances and those derived from the quasar spectra, are in very good agreement and indicates ages for these objects between 0.5 and 1 Gyr.

In the context of the joint formation of quasars and ellipticals, Granato et al. (2001, 2004) included the energy feedback from the central AGN in ellipticals. This feedback produces outflows and stops the star formation in a downsizing fashion in agreement with the chemical evolution of elliptical galaxies (stellar metallicity, luminosity-metallicity relationship, the α enhancement), indicating a shorter period of star formation for the more massive objects and the observed elemental abundances in quasars.

We note that other models (Di Matteo et al. 2005; Hopkins et al. 2008) predict a co-evolution of the BH mass and of the host galaxy stellar mass, as well as a strong quasar feedback in the final phases. The main differences are only on the duration of the luminous and unobscured quasar phases, and on the absolute metallicity in these epochs. Regardless of the specific model, the co-evolution of black holes and galaxies combined with observational selection effects (mostly in optical surveys), naturally explains how quasars of a given luminosity appear to have, on average, the same metallicity at any redshift.

In order to show these effects clearly, we employ the quasar-galaxy evolutionary models reported in Granato et al. (2004). In Figure 2.6 we show the evolution of the gas metallicity in a massive galaxy forming in a dark halo of $M_{\rm halo} = 10^{13.2}\,M_\odot$, along with the evolution of the quasar bolometric luminosity and the total mass gas. While the host galaxy forms stars, the gas metallicity increases. At the same time the BH accretion increases, yielding an increasingly high quasar luminosity. At $z > 5$ the SDSS magnitud limit translates into a minimum quasar bolometric luminosity of about $10^{46}\,{\rm erg\,s^{-1}}$ for detection. Figure 2.6 shows that, by the time the quasar reaches such high luminosity (shaded region), the metallicity in the host galaxy is already higher than $\sim 3\,Z_\odot$. At this time the model expects the quasar to be probably still embedded in gas and dust, although the quasar has already developed a wind expelling gas. It is not easy to identify the stage when the quasar becomes unobscured and detectable in optical surveys, since it depends on the detailed distribution of dust. We assume that the quasar becomes optically visible when more than half of the gas mass has been expelled. In Figure 2.6, the hatched region shows that by the time the quasar is unobscured (when more than half of the gas mass has been expelled), the gas in the host galaxy has already reached a metallicity of about $\sim 4\,Z_\odot$. Summarizing, the co-evolution of BH and galaxies, combined with observational selection effects (mostly in optical surveys), naturally explains how an unobscured quasars of a given luminosity appear to have, on average, the same metallicity at any redshift.

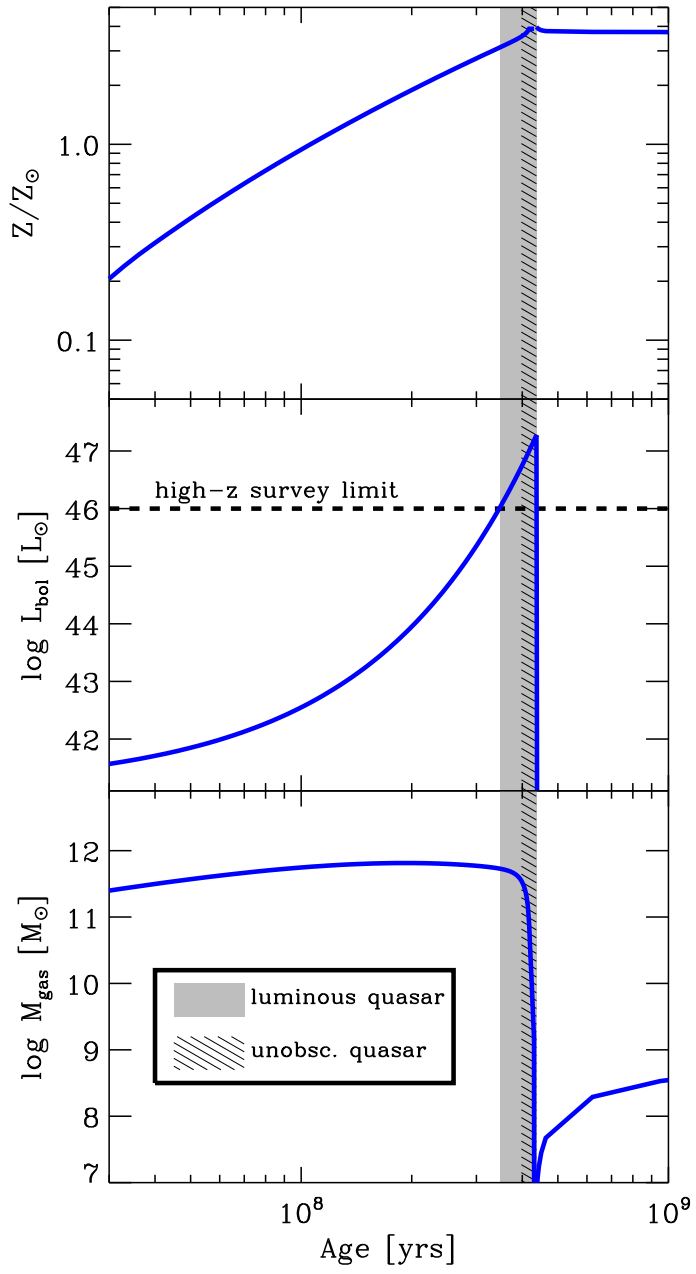

Figure 2.6: Evolution of the gas metallicity (*top*), bolometric quasar luminosity (*middle*), and total gas mass (*bottom*) in the model by Granato et al. (2004). The horizontal dashed line shows the approximate minimum bolometric luminosity detectable at high redshif in the SDSS quasar survey. The dashed area shows the epoch when a high redshift quasar is luminous enough to be detected in the SDSS survey (if unobscured). The hatched zone is the epoch when the quasar has ejected more than half of the gas mass, and it is likely unobscured and therefore detectable in optical surveys. By the time the quasar has reached the luminous "unobscured" epoch the gas is already highly enriched.

2.4 Summary

Quasars are powerful systems whose spectrum is rich of metal features that allow us to investigate the chemical evolution of galaxies at very high redshift, at the end of the reionization epoch.

In this chapter, we present measurements of the (SiIV+OIV)/CIV ratio in a sample of 27 quasars with a redshift range $4 \leq z \leq 6.4$, obtained by means of low resolution NIR and optical spectra, with the goal of investigating the metallicity evolution of quasars in the early Universe.

In order to measure emission line fluxes, these low resolution quasar spectra were fitted using a combination of a power-law continuum and gaussian profiles to model the emission lines. We find that the (SiIV+OIV)/CIV ratio does not show strong evolution with redshift and that the metallicity of the BLR is very high, even in quasars at $z \sim 6$. On average, the observed metallicity does not change, neither among quasars in the observed redshift range $4 \leq z \leq 6.4$, nor when compared with quasars at lower redshifts. All these measurements indicate the existence of vigorous SF and element enrichment in host galaxies in the first Gyr after the Big Bang.

The apparent lack of evolution in the BLR metallicity comes results from a combination of the BH-galaxy co-evolution and a selection effects (mostly in optical surveys). The data also suggest a lack of evolution in the carbon abundance, even among $z > 6$ quasars. The latter result is puzzling, since the minimum enrichment timescales of carbon is about 1 Gyr, i.e., longer than the age of the universe at $z \sim 6$.

CHAPTER 3

DUST MASS EVOLUTION

Another important aspect in the study of the evolution quasar, is to determine the dust properties in the circumnuclear region. To this purpose, the submm/mm observations are important to study the dust properties at high redshift, since this waveband is appropriate to search for structure, as traced by dusty, star forming galaxies surrounding high redshift AGNs.

FIR to mm observations show that most of the energy generated in star formation at $z > 1$ is absorbed by dust, which re-emits the energy at FIR wavelengths, a spectral range that is red-shifted into transparent submm/mm atmospheric windows (Omont et al. 2001).

3.1 Observations and data reduction

3.1.1 Sample selection

First, we selected candidates to be observed with the MAMBO (1.2 mm) and SCUBA (850 μm) instruments. We consider only those quasars where the Hβ region is shifted to the NIR ($2.23 < z < 3.5$). We choose 13 quasars, nine of them were observed and analyzed by Shemmer et al. (2004), and four were observed by Dietrich et al. (2002), who provided us the spectra to perform our own analysis. Second, four quasars already observed in the submm/mm wavelengths by Omont et al. (2003) and Priddey et al. (2003a) were selected to be observed in the NIR in order to investigate the Hβ region. These four objects are bright submm/mm sources and it is important to investigate any dependence between [OIII] emission and FIR emission. In Table 3.1 we list the quasars together with their redshifts,

apparent magnitude, and the references for the observations.

Table 3.1: The quasars sample

Quasar	RA (J2000)	DEC (J2000)	z	Apparent Magnitude	References
SDSS0058+0115	00 58 14.3	+01 15 30	2.54	16.33 H	1
Q0103-260	01 06 04.3	-25 46 53	3.37	18.82 r	1
Q0105-2634	01 08 12.4	-26 18 20	3.48	15.76 H	1
LBQS 0109+0213	01 12 16.9	+02 29 48	3.37	15.26 H	2
Q0302-0019	03 04 49.9	-00 08 13	3.28	15.68 H	1
[HB89]0504+030	05 07 36.4	+03 07 52	2.46	15.43 H	2
[HB89]1246-057	12 49 13.9	-05 59 19	2.23	14.29 H	2
[HB89]1318-113	13 21 09.4	-11 39 32	2.30	15.14 H	2
[HB89]1346-036	13 48 44.1	-03 53 25	2.37	15.09 H	2
UM 629	14 03 23.4	-00 06 07	2.46	16.02 H	2
UM 632	14 04 45.9	-01 30 22	2.51	16.14 H	2
UM 645	14 11 23.5	+00 42 53	2.26	14.24 H	2
SDSS1701+6123	17 01 02.2	+61 23 01	2.30	16.40 H	2
LBQS 0018-0220	00 21 27.3	-02 03 33	2.56	15.40 H	3
HSB 0211+1858	02 14 29.7	+19 12 37	2.47	15.57 H	3
J140955+562827	14 09 55.5	+56 28 27	2.56	15.18 H	4
J164914+530316	03 04 49.9	+53 03 16	2.26	15.57 H	4

References: (1) Dietrich et al. (2002), (2) Shemmer et al. (2004), (3) Priddey et al. (2003a), and (4) Omont et al. (2003)

In order to study the FIR emission in a more robust way, we compiled from the literature a list of 217 quasars observed at submm/mm wavelengths between $1.5 \leq z \leq 6.4$. These objects were taken from Omont et al. (2003, 2001); Priddey et al. (2003a,b); Carilli et al. (2001b); Isaak et al. (2002); Bertoldi et al. (2003a) and Wang et al. (2007).

As in the radio-loud quasars the mm emission is probably due to synchrotron emission, the dominant process in radio-loud sources at submm/mm wavelengths, and not to dust thermal emission (we have excluded these objects from our sample). Thus, the final source selection (230 quasars) was based on its radio flux.

We used the FIRST-VLA and NVSS radio catalogues[1], as well as other radio studies (Carilli et al. 2001b,a; Stern et al. 2000; Isaak et al. 1994; Hooper et al. 1995; Hook et al. 1998; Petric et al. 2006) to check the radio emission from all quasars in our sample.

All sources with $S_{1.4\mathrm{GHz}} > 0.5\,\mathrm{mJy}$ and no FIRST coverage were excluded from the final target list. Our final list comprised 168 radio-quiet quasars. In Appendix B, we report the resulting 850 μm and 1.2 mm flux densities.

3.1.2 Observations

We have carried out continuum observations with SCUBA (850 μm) and MAMBO (1.2 mm) for 13 quasars with NIR data, as well as NIR observations for 4 quasars with submm/mm data.

The submm observations were made with the 15 meter James Clerk Maxwell Telescope (JCMT), located in Mauna Kea, Hawaii, using the wide-band 850 μm filter on the Submillimeter Common-User Bolometer Array (SCUBA). SCUBA consists of two detector arrays, an array of 91 bolometers for operation at short wavelengths, usually 450 μm, and an array of 37 bolometers for use at long wavelengths, commonly 850 μm. As the atmospheric transmission decreases with frequency, hence the long-wave array is the usual primary instrument.

We used the standard 850 μm photometry observing mode. In this mode, the source is placed on the central bolometer, while the rest of the array samples the sky. During each night we monitored the opacity of the atmosphere at 850 μm using skydips[2]. These measurements were compared with data taken by the 225 GHz Caltech Submillimeter-Observatory (CSO) tau-meter. Flux calibration was performed, where possible, against the planets Mars and Uranus, and when planets were not visible, by using standard secondary flux calibrators. The average time to complete the observation of a single source, including pointing, calibration, skydip and slewing overheads, was over 3.2 hrs.

The mm observations were made with the 30 meter IRAM telescope at Pico Veleta (Spain), using the Max-Planck Millimeter Bolometer (MAMBO). MAMBO is a 37-element bolometer array operating at 300 mK. It is sensitive between 190 and 315 GHz, with half-power sensitivity limits at 210 and 290 GHz, and an effective bandwidth center at 250 GHz for thermal sources. The bolometer feed horns are matched to the telescope $FHWM$ beam

[1]The NVSS survey is a sensitive radio survey that was carried out with the VLA at 1.4 GHz in D and DnC configurations, with a 5σ sensitivity of ~ 2.5 mJy beam^{-1}.

[2]The skydip observing mode measures the sky brightness at a range of elevations and uses that data to calculate the zenith sky opacity.

at 1.2 mm of 10.″6, and they are arranged in an hexagonal pattern with a beam separation of 22″. The sources were observed with the central channel of the array, using the standard on-off observing mode with the telescope secondary chopping in azimuth by 50″ at a rate of 2 GHz. The target was positioned on the central bolometer of the array, and after 10 s of integration, the telescope was nodded so the previous *off* beam became the *on* beam.

The telescope pointing was checked about once per hour on nearby continuum sources, and was found to be stable typically within $\sim 2''$. Gain calibration was performed using observations of the planets Mars and Uranus. The sky opacity was monitored regularly, with zenith opacities at 1.2 mm varying between 0.08 and 0.4. Frequent skydip observations were used to determine atmospheric extinction as a function of elevation and time. The point-source sensitivity of MAMBO at 1.2 mm is 20 to 40 mJy/$\sqrt{\text{Hz}}$, depending on weather conditions and the effectiveness of sky-noise subtraction. The average time to complete the observation of a single source was over 1.8 hrs.

NIR observations were obtained with NICS at the TNG. For the low resolution spectroscopy mode, we used the JK′ grism as the disperser element. The JK′ grism consist of a 150 lines/mm blaze = 26.7 deg transmission grating glued on the hypotenuse of a 31 deg prism of IRGn6 glass and working in first order. The quasars were observed with a 1″ wide slit. During the observations the telescope was nodded along the slit and each spectrum was taken several times at different positions along the spatial axis in order to perform the background subtraction. We used the JK′ grism to obtained the $1.15-2.23\,\mu$m wavelength range, which provides an almost uniform dispersion of 11.6 Å pixel^{-1} throughout this range. This results in a resolving power of R $\sim$ 350 (1″ slit). Each night, spectra of standard stars were taken as close as possible in time and in air mass to the quasar to allow the removal of telluric absorption features from the quasar's spectra.

3.1.3 Data reduction

Submm/mm Data Reduction. The SCUBA data were reduced using the SCUBA User Reduction Facility (SURF) software. We used the Remo Tilanus scripts to reduce SCUBA photometry observations within ORAC-DR (Observatory Reduction and Acquisition Control - Data Reduction) pipeline (Jenness & Economou 1999). These scripts reduce the three relevant bolometers (in which the source appears) together. Standard procedures were followed, involving sky-subtraction and clipping at the 3σ level to remove spikes for all quasar's data. Corrections for atmospheric extinction were made using sky opacities derived from

850 μm sky-dips. Flux calibration was performed against the planets Uranus and Mars. Absolute fluxes for the planets were derived using the Starlink package FLUXES. Afterwards we found the mean and errors, and then we combined the 3 bolometers data into a weighted mean through an IDL program.

As some of the sources were observed several times on different dates, we were able to check the consistency of the resulting fluxes. We noticed that observing periods yielded source fluxes which were inconsistent with the observations of the same objects on other dates. We suspect that during such periods, either the telescope pointing, the optics, or an unstable atmosphere lead to a significant sensitivity loss, and we therefore ignored observations during such suspicions periods.

For the observations with MAMBO, the data were analyzed with the MOPSI software package (Zylka 1998) of the Max-Planck-Institut für Radioastronomie. The flux calibration was performed by observing either Mars or Uranus to determine the flux conversion factor. For each channel the sky noise was subtracted by computing the weighted mean of the signals from its surrounding channels. Sky noise subtraction reduce the noise in the signals by typical factors of 2 to 3. Since the source signal in not affected by the sky noise subtraction, the error on the final source signal is given by the remaining noise level of the source channel. The mean rms noise of the coadded signals is ≈ 0.7 mJy. The data obtained with MAMBO are provided already reduced, following a standard process described in the Web page:

http://www.mpifr-bonn.mpg.de/staff/bertoldi/mambo/

Near-IR Data Reduction. The first step is to correct the cross-talking (see Section §2.1.3). The two dimensional, quasars and standard stars spectra, were reduced using IRAF routines.

We create A−B frames from successive frames observed at the two positions (more reference in §2.1.3) to remove most of the background, which is swamped by strong telluric features. Wavelength calibration is achieved by using an Argon lamp spectra. After wavelength calibration, we selected the maxima signal region, in our case the H band, in order to align all the images of the same object and to add them. Residual sky subtraction is then carried out, since only the A−B procedure may not completely remove the sky background due to its time variation. The bad pixels and cosmic rays are removed, and one-dimensional spectra are extracted.

The spectral shape of the quasars was recovered by dividing each spectrum by a spectrum of a standard star, after the stellar absorption features were carefully removed. The

quasar/star ratio was then multiplied by a synthetic spectrum of the same stellar type from the library by Pickles (1998), smoothed to our resolution. Flux calibration of the quasars was obtained by comparing the H magnitude of the quasars with the photometry in H band provided by 2MASS for these objects, and using the flux density of Vega as the zero-point flux.

3.2 Analysis

The NIR spectra analysis is complicated because the presence of many blended FeII emission lines around the Hβ and [OIII]$\lambda\lambda$4959,5007 complex. Therefore, it is necessary to subtract this FeII emission from the spectra in order to obtain accurate measurements of the Hβ and [OIII]λ5007 lines, as well as the continuum. On the other hand, the submm/mm observations were used to derive the FIR luminosity. For this we needed the spectral energy distribution (SED) of high redshift quasars and the submm/mm fluxes. We explains in detail the data analysis in the following paragraphs.

3.2.1 Modeling the NIR spectra

In order to measure the Hβ and [OIII]$\lambda\lambda$4959,5007 line fluxes, the quasar spectra observed in the NIR were fitted with a model consisting of a power-law continuum, the Véron-Cetty et al. (2004) empirical FeII emission template, and a gaussian profile to the emission lines.

Nonstellar Continuum. In the first step, a power-law continuum is determined

$$F_{\rm cont}(\lambda) = k\lambda^{-2-\alpha}$$

where k and α parameters were determined minimizing the function

$$\chi^2 = \sum_{i=1}^{n} \left[\frac{(F_{\rm cont}(\lambda) - F_{\rm obs}(\lambda))^2}{n} \right]$$

$F_{\rm obs}$ is the object flux and k is the normalization constant.

The continuum was fitted only on the spectral regions free from emission features and away from regions with very bad atmospheric transmission. The fit to the continuum was optimized iteratively after the inclusion of the FeII emission template.

FeII emission. Calculating the FeII emission spectrum is much more difficult due to the influence of several parameters, such as metallicity, line fluorescence, emission-line transport, and turbulence velocities that are not well understood yet and, which affect the emergent

FeII spectrum. In spite of these uncertainties, McIntosh et al. (1999); Laor et al. (1997), and others have demostrated the FeII emission spectrum of quasars can be modeled using empirical FeII emission template. We used the Véron-Cetty et al. (2004) optical FeII emission template. In the fitting processes, the intensity and the broadening of the FeII template are free parameters. The FeII emission template was broadened to the dispersion velocity determined from the Hβ line.

In order to obtain the FeII intensity, we used

$$f_{FeII}(\lambda) = I_0(FeII) \times F_{FeII}(\text{template})$$

the I_0 parameter was determined with the function

$$\chi^2 = \sum_{i=1}^{n} \left[\frac{(f_{FeII}(\lambda) - F_{\text{obs}}(\lambda))^2}{n} \right]$$

The total flux is defined as

$$F = \int_0^\infty F_\lambda d\lambda \approx F_\lambda \Delta\lambda$$

in our case,

$$F_{FeII} = f_{FeII} \times \Delta\lambda$$

Hβ and [OIII]$\lambda\lambda$4959,5007 Emission Lines. The Hβ line was fitted with two gaussians with different widths after the continuum and the FeII template were sustracted.

$$F_{\text{Gauss}}(\lambda) = I_0 e^{\left[-0.5\left(\frac{\lambda-\lambda_c}{\sigma}\right)^2\right]}$$

where

$$\sigma = \frac{FWHM}{2\sqrt{2ln2}} = \frac{FWHM}{2.3}$$

I_0, λ_c, and σ were determined with the χ^2 minimization.

After removing Hβ, two gaussians with identical widths were assigned to the two [OIII]$\lambda\lambda$4959,5007 lines. First we fitted the [OIII]λ5007 line, where we got the values of the central intensity, the central λ and σ. Second, we used this σ as well as the intensity ratio I([OIII]λ5007)/I([OIII]λ4959) = 2.95 for fitting the [OIII]λ4959 line. Finally, we calculated the fluxes for H$\beta\lambda$4860 and [OIII]λ5007,

$$F_{\text{line}} \approx F_{\text{Gauss}} \Delta\lambda$$

as well as the FWHM of the broad Hβ line and the [OIII]λ5007 line.

In order to explain the procedure mentioned above, the final spectrum, best-fit model, and components, are plotted in Figure 3.1. The observed spectrum is represented by the black solid line. The model (red solid line) is composed of a continuum (red dashed line), FeII emission, Hβ, and [OIII] (blue line).

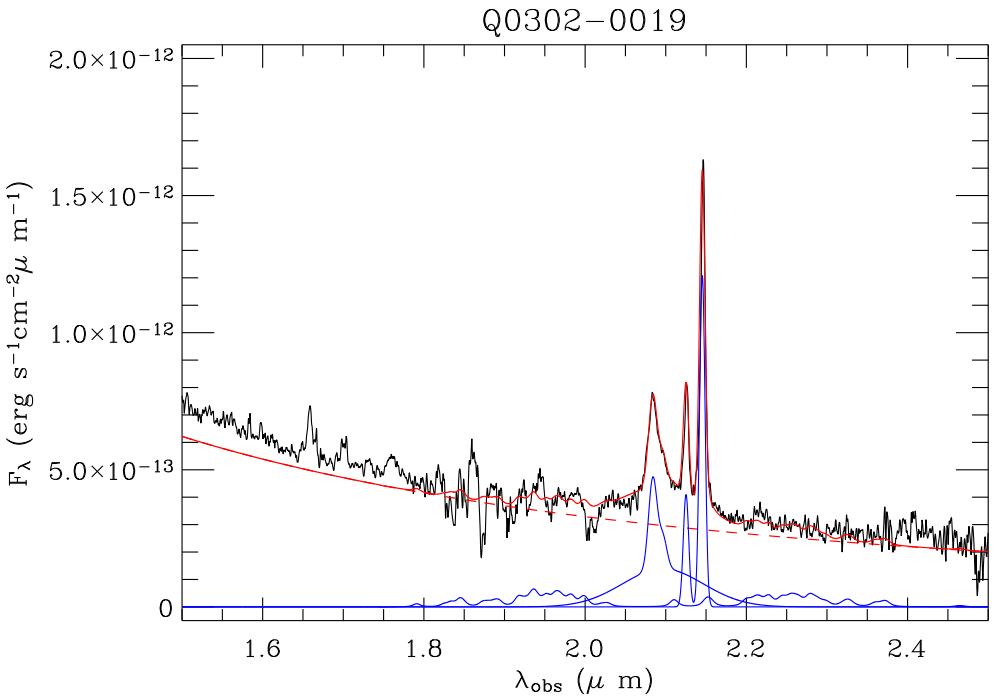

Figure 3.1: Near-IR spectrum of Q0302-0019, a quasar at $z = 3.28$. The black line shows the observed spectrum, while overimposed solid line (red) shows the best fit to the continuum, FeII, Hβ, and [OIII]$\lambda\lambda$4959,5007. The dashed line shows the power-law component. The bottom part of the Figure (blue) shows the FeII bump, Hβ, and [OIII]$\lambda\lambda$4959,5007.

3.2.2 The FIR emission

In order to estimate the FIR luminosity of our quasar sample, we model the FIR continuum with an optically thin graybody. For sources at redshift $z > 1$, the peak of the emission is shifted to submm wavelengths, enabling useful photometric observations with ground-based telescopes in the submm and mm atmospheric windows. Tracing the peak of their SED is crucial for an accurate determination of the IR luminosity and SFR. We adopted a dust temperature of $T_d = 47\,\mathrm{K}$ and an emissivity power law spectral index of $\beta = 1.6$, which is

derived from the mean SED of high redshift quasars (Beelen et al. 2006) as follows:

$$S_\nu(\nu) = B_\nu(T_d)\nu^\beta$$

where B_ν is the Planck function

$$B_\nu(T_d) = \frac{2h}{c^2}\frac{\nu^3}{\exp(h\nu/kT)-1}$$

We normalized the SED to the submm/mm data and integrate the model from rest-frame 40 to 1200 μm to get the total FIR flux.

$$L_{FIR}(SED) = \int_{\nu_1}^{\nu_2} L_\nu d\nu = \int_{\nu_1}^{\nu_2} \nu L_\nu \frac{d\nu}{\nu}$$

$$\lg\nu = \frac{\ln\nu}{\ln 10} \Longrightarrow \ln\nu = 2.3\lg\nu$$

$$2.3\frac{d\lg\nu}{d\nu}d\nu = \frac{d\ln\nu}{d\nu}d\nu = \frac{d\nu}{\nu}$$

$$\frac{d\nu}{\nu} = 2.3 d\lg\nu$$

$$L_{FIR}(SED) = \int_{\nu_1}^{\nu_2} 2.3\nu L_\nu d\lg\nu = 2.3\int_{\nu_1}^{\nu_2} 10^{\lg\nu L_\nu} d\lg\nu$$

$$L_{FIR}(SED) = 2.3\sum_i 10^{[\lg\nu L_\nu]_i}[d\lg\nu]_i$$

where $d\lg\nu$ is the Δ in the frequency (in this case is 0.02) and $i = 40$ to 1200 μm.

On the other hand,

$$\nu_0 S_{\nu_0}(\text{obs}) = \frac{\nu_z L_{\nu_z}(\text{rest})}{4\pi D_L^2}$$

$$\nu_z L_{\nu_z}(\text{rest}) = \nu_0 S_{\nu_0}(\text{obs})4\pi D_L^2$$

Besides,

$$\nu_z = (z+1)\nu_0$$

For 1.2 mm, $\nu_0 = 2.50\times10^{11}$ Hz and for 850 μm, $\nu_0 = 3.45\times10^{11}$ Hz. In order to normalize, we took the ratio

$$\frac{\nu_z L_{\nu_z}(\text{rest})}{\nu L_\nu(SED)}$$

then

$$L_{FIR}(\text{quasar}) = L_{FIR}(SED) \times \frac{4\pi D_L^2 \nu_0 S_{\nu_0}(\text{obs})}{\nu L_\nu(SED)}$$

where D_L is the luminosity distance. This equation was used to calculate the FIR luminosities for all the quasars.

The errors are given by:

$$\sigma_L = \frac{\sigma_{S_{\nu_0}}}{S_{\nu_0}} L_{FIR}(\text{quasar})$$

The FIR luminosity mean was determined from the weighted mean of all data within each bin, i.e., detections (3σ) and non-detections (upper limits, including negative fluxes). For the negative fluxes, we took the FIR luminosity equal to zero, keeping its error.

$$\langle L_{FIR} \rangle = \frac{\sum w_i L_{FIR_i}}{\sum w_i}$$

$$w_i = \frac{1}{\sigma_{L_i}^2}$$

and

$$\sigma_{L_{FIR}} = \left[\sum w_i\right]^{-0.5}$$

In the following, we denote high redshift sources as detected at $850\,\mu$m or 1.2 mm if their flux desities are above three times the rms noise level. In addition, we calculated the FIR luminosity using the Elvis, Arp220, and M82 SEDs (Elvis et al. 1994). Nevertheless, we decided to use the SED of a modified blackbody spectrum (Beelen et al. 2006) because it gave more accurate results.

3.3 Results

The rest frame FIR thermal dust continuum of optically luminous radio-quiet $z > 1$ quasars, has been observed for 168 quasars resulting in 52 detections (Omont et al. (2003, 2001); Priddey et al. (2003a,b); Carilli et al. (2001b); Isaak et al. (2002); Bertoldi et al. (2003a); Wang et al. (2007) and our observations), i.e., they have flux densities three times greater than the rms noise (3σ).

We calculated FIR luminosity, ($L_{\rm FIR}$), for all quasars in the sample. The derived properties of the $z > 1$ radio-quiet quasars are listed in Appendix B. Most of the submm/mm detected sources are very luminous in the FIR band, with implied $L_{\rm FIR} \geq 10^{13} L_{\odot}$, slightly greater than the typical luminosity of ultra-luminous infrared galaxies such as Arp 220 ($L_{\rm FIR} \geq 10^{12} L_{\odot}$). These luminosity values mean that very powerful energy sources, starbursts and/or AGNs, are present but hidden behind dust; energetic radiation from the energy sources is absorbed by the surrounding dust, and the heated dust grains re-emit this energy as IR thermal radiation.

The purpose of this work is also to correlate the submm/mm emission with other quasar properties, such as BH mass, accretion rate, metallicity, [OIII] luminosity, and UV luminosity. This may tell us whether the dust content and star formation in the host galaxy is somehow linked with the mass, accretion rate, metallicity, [OIII] luminosity or UV luminosity.

3.3.1 FIR luminosity as a function of redshift

Figure 3.2 shows the redshift distribution of the entire sample as a function of FIR luminosity (52 detections and 116 non-detections). The sources detected are shown as filled symbols, whereas the down-pointing arrows indicate sources not detected. For sources non detected with negative and positive signal a 2σ upper limit is plotted.

Figure 3.2 (right panel) shows the mean redshift and weighted mean FIR luminosity for the data set (detections and non-detections). For the quasars not detected at submm/mm wavelength showing apparent negative fluxes, we took the FIR luminosity equal to zero, but keeping its error. For sources with positive fluxes, we took its real value and not 2σ, as in Figure 3.2 (left panel). Three redshift bins have been chosen: $1.50 \leq z < 3.0$ (61 objects), $3.0 < z \leq 4.5$ (72 objects), and $4.5 < z \leq 6.4$ (35 objects).

In the left panel of Figure 3.2, we found the comparison of the FIR luminosities of the $z \sim 2$ quasars are only slightly higher than the luminosities of the $z > 4$ quasars, a fact which indicates no clear sign of evolution of the FIR luminosity of optically luminous quasars with redshift. However, in Figure 3.2 (right panel) the evolution seems much clearer. At $z > 4$, galaxies had less time to form dust relative to lower redshift galaxies, hence the former have lower FIR luminosity. Furthermore, at $z \geq 4.5$ alone we have 9 detections. Quasars apparently differ in this respect from radio galaxies (Archibald et al. 2001), from which a dramatic increase of FIR luminosity with redshift was inferred over the whole redshift range $1 < z < 4$.

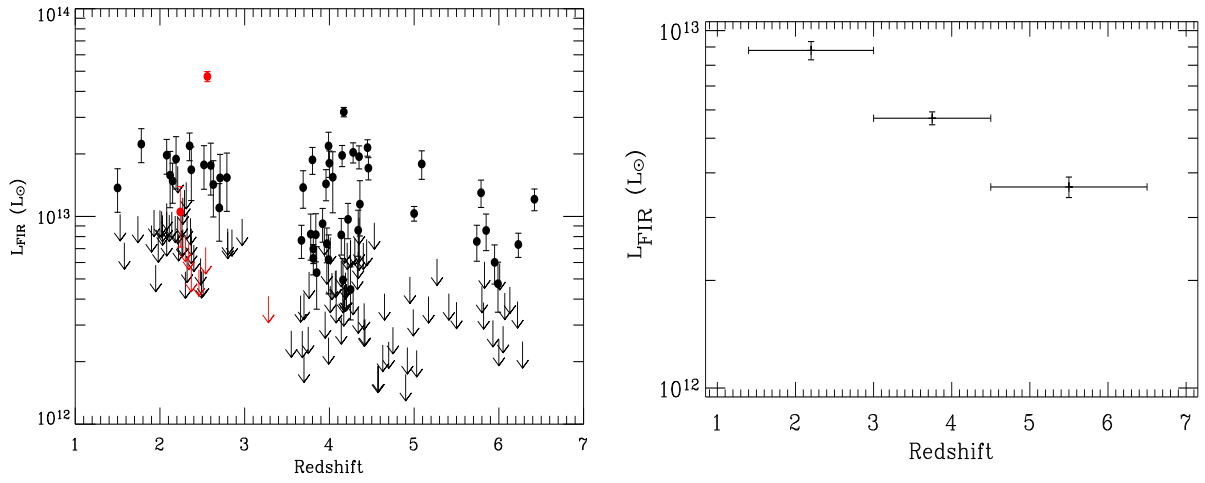

Figure 3.2: (*Left*) Redshift distribution of the quasar sample as a function of FIR luminosity implied by the SCUBA 850-μm and MAMBO 1.2 mm flux densities. The filled symbols represent detections with 3σ errors and the down-pointing arrows denote upper limits. Red: our observations. (*Right*) FIR luminosity as a function of redshift, determined from the weighted mean of all the data within each bin.

In order to better quantify the millimeter properties of high redshift quasars, we need deeper observations with the new generation of sensitive IR/submm/mm observatories: LMT, ALMA, and Herschel.

3.3.2 FIR luminosity as a function of the Black Hole mass and the Eddington ratio

The estimate of BH masses and the ratio of luminosity to the luminosity derived from the black hole mass (the Eddington ratio) are the fundamental parameters in the evolution of active galaxies.

An important question in studies of the early Universe is how the growth of massive BH relates to the formation of early stellar populations. A tight correlation between BH masses and bulge luminosities or velocity dispersions in local galaxies indicates their formation was closely related. The recent detection of strong thermal dust emission from many high-redshift quasars shows that vigorous star formation is coeval with BH masses (Carilli et al.

2001a; Omont et al. 2001; Isaak et al. 2002). In order to verify whether the BH masses correlates with the FIR luminosity, we calculate the BH mass ($M_{\rm BH}$) for the quasars in our sample by using Hβ, CIV, and MgII emission linewidths and fluxes. We can measure Hβ and monochromatic luminosities at the rest-frame 5100 Å from our NIR spectra. Monochromatic luminosities were derived according to

$$\lambda L_{\lambda}(5100) = 4\pi D_L^2 \lambda_{\rm obs} F_{\lambda}({\rm obs})$$

and following Shemmer et al. (2004) the BH masses were determined from the equation

$$M_{\rm BH} = 6.2 \times 10^6 \left[\frac{\lambda L_{\lambda}(5100)}{10^{44}\,{\rm erg\,s^{-1}}}\right]^{0.6} \left[\frac{FWHM(H\beta)}{10^3\,{\rm km\,s^{-1}}}\right]^2 M_{\odot}$$

On the other hand, from the compiled list from literature, we looked for the available spectra in the SDSS database. We found only 50 spectra from which we obtained the BH masses by means of CIV and MgII emission linewidths and fluxes. Warner et al. (2003) expressed the BH mass as

$$M_{\rm BH} = 1.4 \times 10^6 \left[\frac{\lambda L_{\lambda}(1450)}{10^{44}\,{\rm erg\,s^{-1}}}\right]^{0.7} \left[\frac{FWHM(CIV)}{10^3\,{\rm km\,s^{-1}}}\right]^2 M_{\odot}$$

we also apply the formula derived by Willott et al. (2003) to estimate the BH mass

$$M_{\rm BH} = 3.37 \left[\frac{\lambda L_{\lambda}(3000)}{10^{44}\,{\rm erg\,s^{-1}}}\right]^{0.47} \left[\frac{FWHM(MgII)}{{\rm km\,s^{-1}}}\right]^2 M_{\odot}$$

For the objects without available spectra, we took the BH masses from literature (Brotherton et al. 1994; Iwamuro et al. 2002; Shemmer et al. 2004; Barth et al. 2003; Priddey et al. 2003b; Jiang et al. 2007, 2006; Robson et al. 2004; Dietrich & Hamann 2004).

From these obtained BH masses, we conclude that fifteen submm/mm detected quasars have very large BH masses ($M_{\rm BH} > 10^9 M_{\odot}$), and six objects submm/mm detected are at the upper part of known BHs at any redshift; confirming that these BHs are probably hosted by the progenitors of the most massive present-day ellipticals.

In Figure 3.3 (left panel) we plot the FIR luminosities as a function of BH masses, along with a sample of low-z quasars observed at IR wavelengths (Haas et al. 2000, 2003). In Figure 3.3 (right panel), we show the mean BH mass and weighted mean FIR luminosity of all the data within each mass bin. Blue color represents the weighted mean FIR luminosity of low-z quasars. We found a tendency between FIR luminosity with the BH mass. This probably implies the BHs are growing almost continuously throughout periods of vigorous star formation.

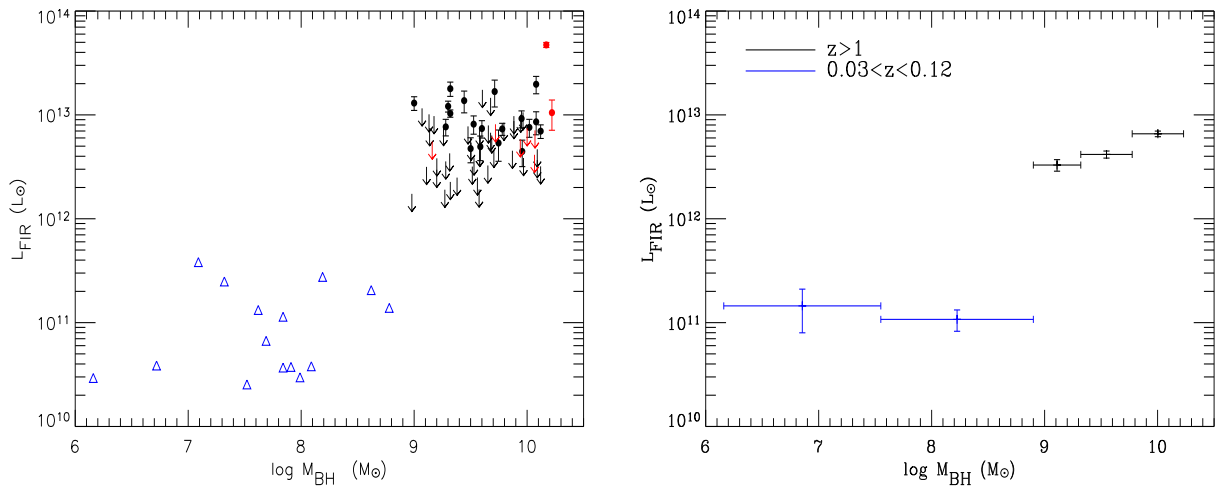

Figure 3.3: *Left panel*: Correlation between FIR luminosity and the BH mass. Symbols are the same as in Figure 3.2. Triangles: detections at IR wavelengths ($z < 0.12$) (Haas et al. 2000, 2003). *Right panel*: L_{FIR} plotted against the $M_{\rm BH}$, determined from the weighted mean of all the data within each bin.

The strong difference between low and high redshift quasars is owing to selection effects: due to limited sensitivity of AGN surveys in terms of minimum detectable flux; at low redshift surveys can sample low luminosity AGN, with low BH masses, while at high redshift only very luminous AGN (which necessarily have large BH masses) can be detected.

We further use the luminosities to estimate Eddington ratios, which can provide insights as to the accretion states of the AGNs. We calculated the Eddington ratio $L_{\rm bol}/L_{\rm Edd}$ (hereafter $L/L_{\rm Edd}$), which is defined as the ratio between the bolometric accretion luminosity $L_{\rm bol}$ and the Eddington luminosity $L_{\rm Edd}$, i.e., the limit where gravitational force and radiation pressure are balanced. The Eddington luminosity is directly proportional to $M_{\rm BH}$, and can be written as

$$L_{\rm Edd} = 1.51 \times 10^{38} \left(\frac{M_{\rm BH}}{M_\odot} \right) \qquad {\rm erg\,s^{-1}}$$

and the bolometric luminosity is calculated from the monochromatic luminosity at 1500 Å as:

$$L_{\rm bol} = 3.15 \times \lambda L_\lambda(1500) \qquad {\rm erg\,s^{-1}},$$

which is a measure of the accretion rate.

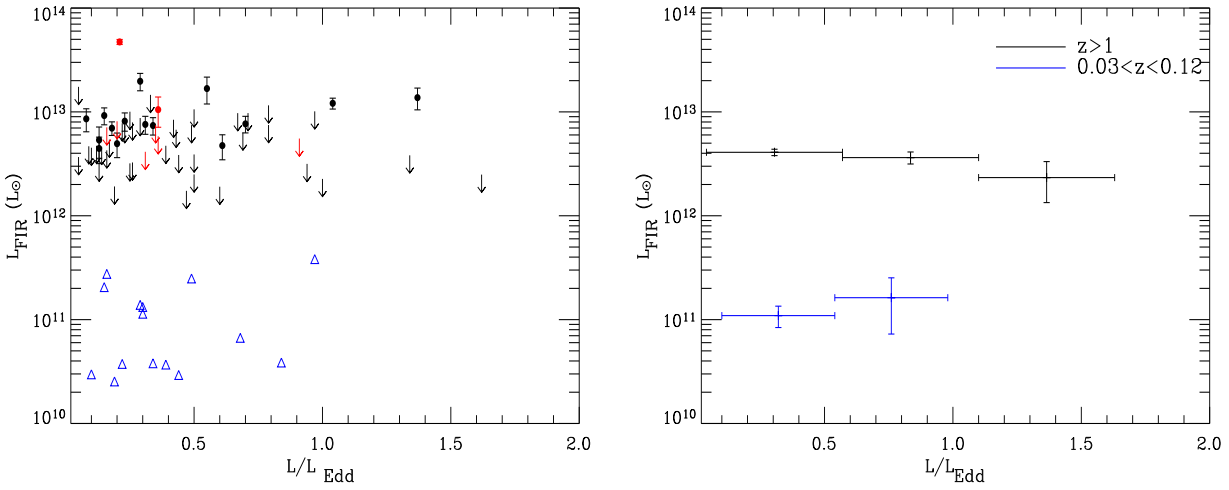

Figure 3.4: *Left*: FIR luminosity againts the Eddington ratio. Symbols are the same as in Figure 3.3. *Right*: FIR luminosity againts the Eddington ratio, determined from weighted mean of all the data within each bin.

Figure 3.4 (left panel) shows the FIR luminosity as a function of the Eddington ratio along with a sample of low-z quasars observed at IR wavelengths. In the right panel (Figure 3.4), we show the mean Eddington ratio and weighted mean FIR luminosity. Blue color represents the weighted mean FIR luminosity of the low-z quasars. We did not find a correlation between the FIR luminosity and the Eddington ratio. The lower luminosity objects can have high Eddington ratio, but low BH mass. There are some quasars with L/L_{Edd} up to 1 (i.e. the maximum value possible), but these have low luminosity, simply because they have low BH masses. In addition, in Figure 3.4 there are a few objects with $L/L_{Edd} > 1$, which is probably due to uncertainties on the BH masses and/or on the luminosity.

3.3.3 FIR luminosity as a function of [OIII] luminosity

Recent quasar surveys have found the NLR strength decreases systematically with increasing luminosity to the extent that they are nearly undetectable in luminous quasars at $z \sim 1$ (Croom et al. 2002). At $z > 2$ the most luminous quasars are also characterized by the total absence of the NLR (specifically [OIII]λ5007). However, some high z quasars have been found to show strong [OIII]λ5007 emission, which probably indicates the population of high redshift quasars is divided into two distinct groups: one containing quasars without NLR

(the continuation of the lower redshift quasar) and a new group of quasars with extremely strong NLR.

A possible explanation could be the host of quasars with strong [OIII]λ5007 are experiencing powerful starburst activity and the large amount of dense gas associated to the starburst enhances the emission of [OIII]. If the quasars with strong NLR (i.e strong [OIII]λ5007 emission) are characterized by vigorous star formation, then they should increase the FIR emission due to warm dust heated by the starburst. In order to test this scenario, we used the submm/mm and NIR data.

For the quasars observed at NIR wavelength, we calculated the [OIII]λ5007 luminosity, according to the expression

$$L_{[OIII]} = 4\pi D_L^2 F_{[OIII]}$$

where D_L is the luminosity distance and $F_{[OIII]}$ is the [OIII]λ5007 flux.

For the objects not observed in the NIR, we took the [OIII] luminosity from Netzer et al. (2004). We calculated the [OIII]λ5007 luminosity using the same procedure described by Shemmer et al. (2004).

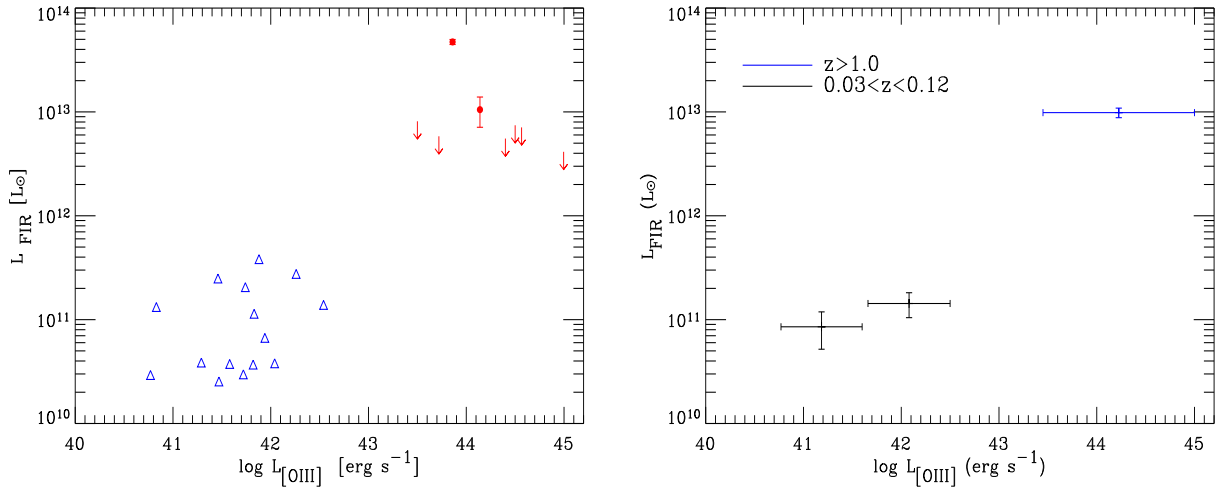

Figure 3.5: *Left:* FIR luminosity as a function of [OIII] luminosity. Symbols are the same as in Figure 3.3. *Right:* FIR luminosity as a function of [OIII] luminosity, determined from the weighted mean of all the data within each bin.

Figure 3.5 (left panel) shows the FIR luminosity as a function of the [OIII]λ5007 luminosity, $L_{[OIII]}$, for the quasars at high redshift ($z > 1$) and at lower redshift ($z < 0.12$). Right panel shows the mean [OIII] luminosity and weighted mean FIR luminosity. Blue color represents the weighted mean FIR luminosity of the low-z quasars. As we can see, the FIR

luminosity increases with the [OIII] luminosity, unfortunately we have very few data and it is not possible to obtain a statistically robust result. However, more observations are needed of the Hβ region for the quasars having submm/mm emission to confirm this possible trend.

3.3.4 FIR luminosity as a function of metallicity

In order to investigate the chemical evolution in quasars, we used the fluxes of the NVλ1240 and CIVλ1545 UV emission lines for our quasar sample. The NV/CIV ratio is an additional metallicity tracer that can be more easily used for these quasars (because several data are already available in the literature). With the SDSS spectra we measured these lines and we complemented the data set with the NV/CIV measurements given in Netzer et al. (2004).

One would expected the most metal-rich quasars (specially in N) correspond to the most submm/mm luminous quasars, because the latter traces star formation (which enriches the ISM through enhanced SN rate). Nevertheless, as we can see in Figure 3.6, there is no strong correlation between FIR luminosity and metallicity. This trend can be explained in two ways: 1) the lack of an obvious trend in the NV/CIV ratio with FIR luminosity suggests that the observed gas metallicity is not due to the ongoing star forming event, but is was mostly produced by previous events of SF, 2) we need more obervations of high metallicity quasars (NV/CIV>2), since our sample only has one submm/mm detected source and cannot be representative of any trend.

3.3.5 FIR luminosity as a function of the UV luminosity

In quasars, the observed UV emission is mostly due to radiation from the accretion disk around the BH, while the FIR emission can instead be partly due to SF and partly to re-radiation of dust heated by the AGN.

In order to check whether there is an evolution in the dust content, we have derived monochromatic luminosities for our quasar sample at the rest-frame 1500 Å using data from the SDSS. For the quasars without SDSS photometry, we used the photometry of the POSS catalog.

In order to infer UV luminosity at rest-frame, we took the observations in the closest optical filter, at rest 1500 Å, then we derived νF_ν from the photometry in that filter, using a spectral index of α =-0.38.

Figure 3.7 (left) displays the FIR luminosity versus UV luminosity. The mean UV luminosity and weighted mean FIR luminosity are plotted in the right panel. We found that the

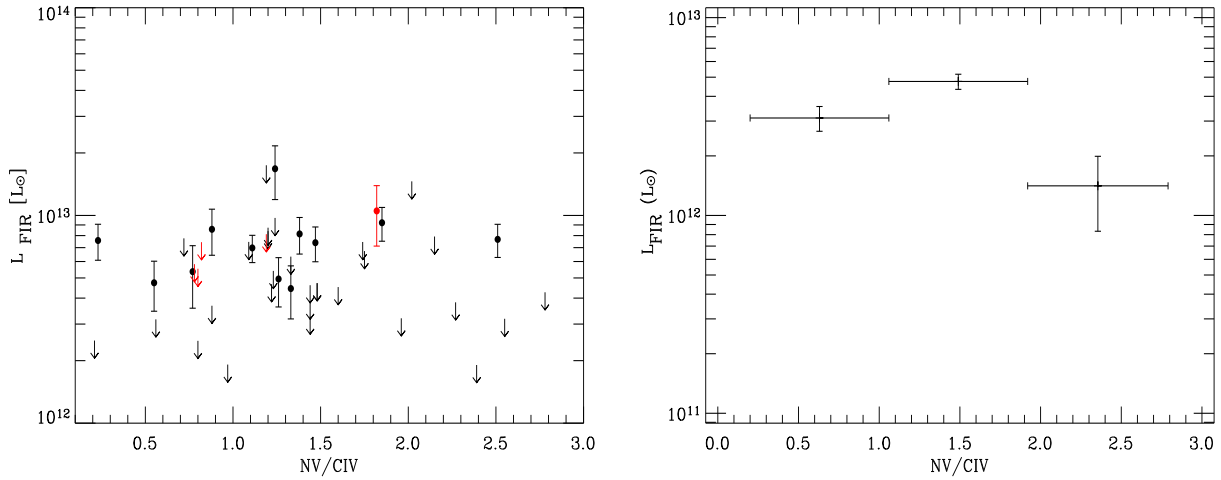

Figure 3.6: *Left panel*: FIR luminosity versus NV/CIV. Symbols are the same as in Figure 3.3. *Right panel*: FIR luminosity versus NV/CIV, determined from the weighted mean of all the data within each bin.

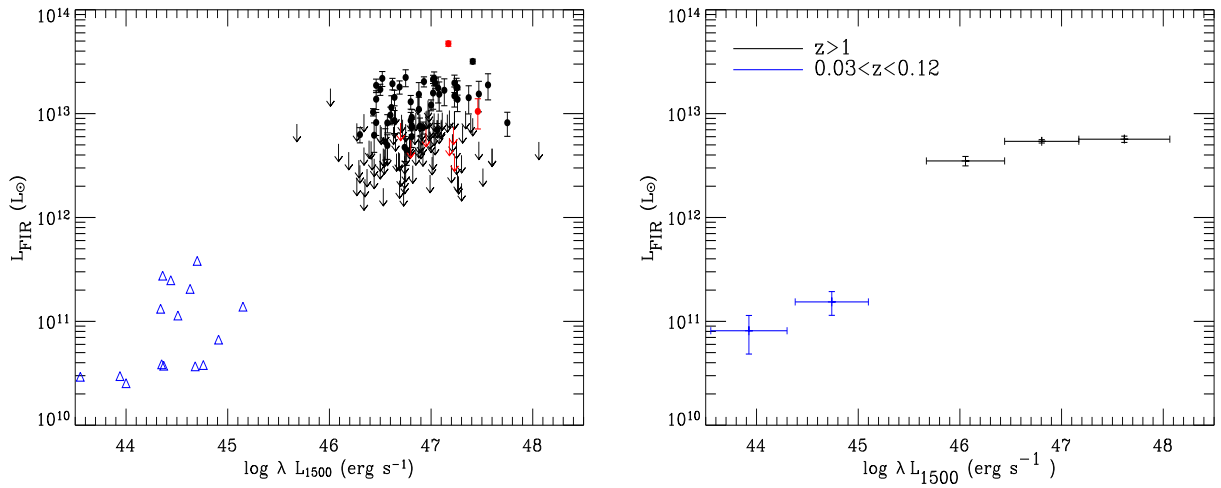

Figure 3.7: *Left*: FIR luminosity as a function of $\lambda L_\lambda(1500\,\text{Å})$. Symbols are the same as in Figure 3.3. *Right*: FIR luminosity as a function of $\lambda L_\lambda(1500\,\text{Å})$, determined from weighted mean of all the data within each bin.

FIR luminosity increases with UV luminosities, confirming evolution in the dust content. Moreover, if FIR emission in quasars traces mostly SF (Lutz et al. 2008; Netzer 2008), then the correlation between UV and FIR suggest a tight relation between BH accretion and SF in the host galaxy, which is expected by BH-galaxy evolutionay models.

3.3.6 FIR/UV luminosity as a function of redshift

The ratio of the FIR to UV luminosities is a measure of the total dust opacity experienced by the UV stellar continuum in a region, therefore, this ratio gives us information about the dust obscuration.

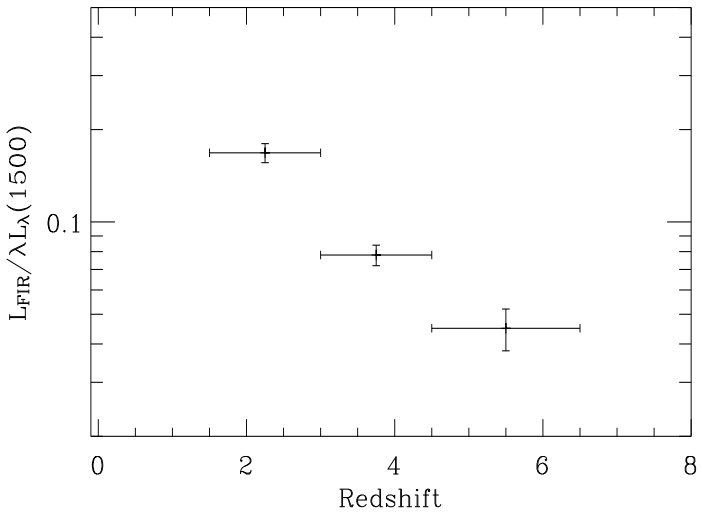

Figure 3.8: Evolution of $L_{\rm FIR}/L_{UV}$ ratio as a function of redshift, for $\lambda L_\lambda(1500\,\text{Å})$ intervals.

We found that the FIR/UV luminosity ratio decreases towards higher redshifts (Figure 3.8), indicating an evolution in the dust mass at $z \sim 5$. This result is predicted by the theory of evolution and formation of dust (Calura et al. 2008; Dwek et al. 2007). This dependency we found is important for the relation between star formation in quasars and dust evolution at high redshift. Thus, as we mentioned before, it is very relevant to confirm this trend with deeper observations. The JWST, LMT and ALMA will allow to obtain the FIR and UV rest frame emissions of galaxies in the early Universe with the resolution and sensitivity needed for this purpose.

According to what discussed above, the fact that FIR/UV decreases with redshift indicates that the correlation between FIR and UV luminosities is not linear, but that SF (traced by FIR) increases more slowly than BH accretion (traced by UV) and hence as a function of redshift.

3.4 Summary

In this chapter, we analyzed a large sample of radio quiet quasars (168 objects) with submm/mm observations in the redshift range $1.5 \leq z \leq 6.4$, in order to check if the submm/mm emission (i.e. due to star formation) correlates with other quasar properties, such as BH mass, accretion rate, [OIII] luminosity, metallicity, and UV luminosity.

We calculated the FIR luminosity using a SED of a graybody spectrum with $T = 47\,K$ and $\beta = 1.6$. The result shows the FIR luminosity of the $z \sim 2$ quasars are marginally higher than the luminosities of the $z \geq 4$ quasars, i.e., there is no strong evolution of the FIR luminosity between $1.5 \leq z \leq 6.4$.

The detection of strong thermal dust emission from many high redshift quasars shows that vigorous star formation is coeval with BH masses. We obtained the BH mass by using CIV, MgII, and Hβ emission linewidths and fluxes. We found a trend between the FIR luminosity and the BH mass. No correlation was found between FIR luminosity and Eddington ratio.

In order to verify if the [OIII] emission, which is observed in some high redshift quasars, is associated with enhanced star formation in the host galaxy (therefore enhanced mm/submm emission), we calculated the [OIII] luminosity and we found that it increases with the FIR luminosity. However, our sample is very small to provide a statistically reliable result. There are needed more observations on the Hβ region of quasars that have submm/mm emission.

With respect to the metallicity, one would expect that more submm/mm luminous quasars would also be more metal-rich, however, no correlation was found between FIR luminosity and metallicity. This probably indicates that current SF in quasar hosts is not a significant source of metal enrichment for the gas.

In order to check whether there is an evolution in the dust content, we derived monochromatic luminosities at the rest-frame 1500 Å. We found that the FIR luminosity increases with UV luminosity, suggesting a tight relation between BH accretion and SF in the host galaxy. Furthermore, we found that FIR/UV ratio diminishes towards higher redshifts, indicating an evolution in the dust mass at $z \sim 5$, which is in a good agreement with the theory of evolution and formation of dust. From here, it is very important to confirm this trend with

observations an order of magnitude deeper in a few years with the coming instruments as the LMT, ALMA and JWST.

CHAPTER 4

MIR AND HARD X-RAY LUMINOSITIES, SILICATES FEATURES AND SFR IN AGNS

IR and X-ray data complement each other and are important to understand the overall AGN energy balance. Hard X-rays, unless extremely absorbed in Compton-thick objects, can provide a direct view to the central engine, and are often believed to be a reasonable isotropic measure of the bolometric luminosity of the AGN. The nuclear IR continuum in AGNs, in contrast, is due to a reprocessing of the AGN emission by the circumnuclear dust, e.g., in the torus. The observed MIR emission is thus a function not only of the AGN luminosity, but also of the distribution of the obscuring matter and of the viewing direction of the observer. In the simplest form this is due to the covering factor, i.e., the fraction of the radiating source covered by the obscuring material and the distance of the obscuring dust.

A quantitative estimate of the contribution of obscured AGNs to the X-ray and IR backgrounds is crucial to infer the star formation history of the universe from galaxy luminosity functions, and it is important to understand the evolution of galaxies and AGNs. While most of the dust emission is continuum radiation, in the MIR two of its spectral features are observable arising near 10 and 18 μm, which are attributed to silicates. Detecting silicate features in emission can identify the dusty medium as optically thin, while deep absorption characterizes optically thick obscuration.

The 5$-$15 μm MIR spectral energy distribution can be decomposed into three main components: 1) emission features from what is thought to be PAH molecules, 2) power law or warm blackbody emission, and 3) extinction characterized by prominent silicate absorption

features. The first is understood to be powered entirely by star formation, while the second is predominantly emission from the AGN. The third component can be found in both starbursts and AGNs since it only requires a dust screen around hot dust emission.

MIR spectroscopy provides a powerful tool for investigating the nature and physical processes in AGNs and in the starburst-dominated regions frequently associated to them. The Infrared Spectrograph (IRS)[1] onboard of the *Spitzer Space Telescope* (Houck et al. 2004) now enables a detailed investigation of physical processes in large samples of AGN and stellar (starburst) power sources. Even at low resolution, the IRS spectra of AGNs showed the diversity of the MIR spectral features: silicate absorption and emission, PAH emission and strong fine-structure lines of neon, oxygen, sulfur, and silicon (Weedman et al. 2005). The silicates features at 9.7 μm and 18 μm are particularly important in the context of the unification model (e.g. Antonucci 1993). It is important, therefore, to investigate the distribution of silicate strengths within a large sample of different types of AGNs. The PAH features provide both an indication of the energy source heating the dust and redshift estimates for sources that are completely obscured at shorter wavelengths. The PAH features can also be used to quantify the SFR in AGN host galaxies (Shi et al. 2007). Finally, MIR fine-structure lines can be used to study three properties of the NLR gas: excitation, electron temperature, and electron density. Besides, ratios of the fine-structure lines can be used to gauge the dominant ionizing source, either hot stars or an active nucleus.

4.1 Data acquisition and data reduction

4.1.1 Sample selection

We gathered a large sample of AGNs from the literature that have been observed with IRS on the *Spitzer Space Telescope*. Our sample includes a variety of objects: radio-quiet quasars, radio-loud quasars, BAL quasars, FR II radio galaxies, Seyfert 1 and Seyfert 2 galaxies. The AGN sample is drawn from Buchanan et al. (2006), Ruiz et al. (2007), Shi et al. (2006), Sirocky et al. (2008), Sturm et al. (2006), Teng et al. (2008), Weedman et al. (2006), as well as some IRAS sources. All these objects have available X-ray data in the literature from different satellites (ASCA, BeppoSAX, Chandra, XMM-Newton), with HI column density from 10^{19} up to $10^{25}\,\mathrm{cm}^{-2}$. The MIR spectra for these AGNs were acquired from the *Spitzer*

[1] The IRS was a collaborative venture between Cornell University and Ball Aerospace Corporation funded by NASA through the Jet propulsion Laboratory and the Ames Research Center.

archival data using the LEOPARD software[2]. The entire sample consists of 127 Astronomical Observation Requests (AORs) and are listed in Appendix C. We downloaded the post-BCD (Basic Calibrated Data) data, BCD-Basic data, and Calibration data frames for each AOR.

The observations were retrieved from the *Spitzer* database of various *Spitzer*/IRS programs. We used only the IRS observations in the standard *staring* mode of sources that include low-resolution (the spectral resolution varies from R$\sim$60$-$120 across each order) modules. There are two wavelength ranges for the low-resolution mode of the IRS spectrograph: Short-Low (SL) and Long-Low (LL) modes that can obtain data sets in the wavelength ranges SL2: 5.2$-$7.7 μm, SL1: 7.4$-$14.5 μm, LL2: 14$-$21.3 μm, and LL1; 19.5$-$38 μm.

4.1.2 Data reduction

Our data reduction starts with two-dimensional BCD produced by the IRS pipeline at the *Spitzer* Science Center (SSC). The processing steps taken by the IRS pipeline include ramp fitting, dark-sky subtraction, droop correction, linearity correction, flat division, and wavelength calibration[3]. At MIR wavelengths, the dominant source of noise is the sky background, mostly from zodiacal light. We perform additional data reduction steps, including subtraction of the residual background in the BCD images and cleansing of bad pixels. All images with the same position on the slit were combined to obtain the source spectrum. We removed the background emission by differencing images with the sources in the SL1 and SL2 or LL1 and LL2 apertures (i.e: SL1$-$SL2, LL1$-$LL2). This resulted in a set of images containing a positive and negative spectrum in each observed order. The individual reduced frames were co-added to produce final 2D spectra at each nod position. After the background subtraction, the 2D spectra were cleaned for bad pixels by visual examination. This was done by using the standard tasks in the IRAF environment.

One-dimensional spectra for both nod positions were then optimally extracted and calibrated by means of SPitzer IRS Custom Extraction (SPICE) software package[4], the post-pipeline IRS package provided by the SSC. SPICE is a Java-based tool that allows the user to interactively display and extract IRS spectra. The spectral extraction aperture can be adjusted to maximize the S/N. For our data, the extraction aperture was set to the SPICE default. Individual spectra were flux-calibrated with SPICE using standard calibrations files.

[2]See http://ssc.spitzer.caltech.edu/propkit/spot/index.html

[3]See the IRS pipeline Handbook at http://ssc.spitzer.caltech.edu/IRS/dh

[4]See http://ssc.spitzer.caltech.edu/postbcd/spice.html for the description of the software and the public release status.

Wavelength calibration is performed by the IRS pipeline. The final spectrum for each source is produced by averaging the two spectra for each module (one for each nod position) and combining the spectra from the first and second orders together using linear interpolation. Different orders have different pixel-to-wavelength scales; therefore, we resample the overlapping spectra onto the smallest scale and produce the final combined spectra using IDL routines. As an example, the final average IRS spectrum obtained in the low-resolution mode (SL and LL) is shown in Figure 4.1.

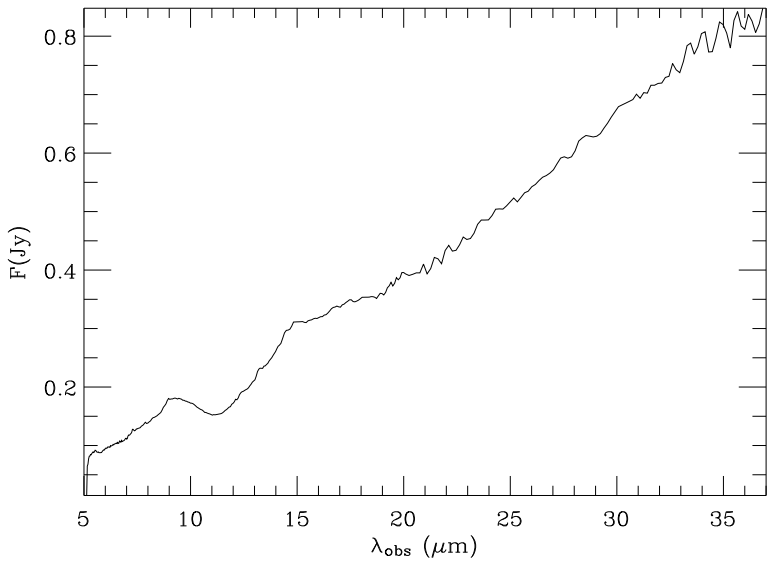

Figure 4.1: *Spitzer* IRS spectrum of IRAS23060+0505 taken in low-resolution mode: SL+LL. The silicate absorption at 9.7 μm is clearly detected.

4.2 Silicate determinations

Dust produces both the MIR continuum and the silicates features. As a first step toward interpreting the silicate absorption/emission features in the AGNs, we attempted to fit their 5.5−14.5 μm rest-frame wavelength spectra by a model consisting of a power-law continuum, M82 starburst template, and silicate strength of the emission or absorption feature.

Continuum Fitting. The silicate features appear characteristically different in the nuclear spectra of various classes of galaxies. In order to quantify these silicate properties, the strength of the emission or absorption must be measured relative to the underlying

continuum. Hence, in order to determine the continuum, we must exclude these emission and absorption features from the fitting intervals. There are three characteristic classes of spectra that requiere modification of the fitting intervals (Spoon et al. 2007): Continuum-dominated spectra, characterized by the presence of a broad emission feature around $\lambda \sim 10\,\mu$m that extends toward longer wavelengths and not showing neither PAH emission nor ice absorption. Absorption-dominated spectra, sources without or with weak PAHs emission but with deep $9.7\,\mu$m silicate absorption feature. PAH-dominated spectra exhibiting strong PAH emission.

In order to accurately estimate the strength of the $9.7\,\mu$m silicate absorption/emission features, a continuum level must be determined using data at $\lambda_{\rm rest} < 8.0\,\mu$m and $>13.5\,\mu$m. For continuum-dominated spectra and absorption-dominated spectra, the $5.5{-}14.5\,\mu$m continuum is estimated from a power law fit between $5.5{-}8.0\,\mu$m and $13.5{-}14.0\,\mu$m. For PAH-dominated spectra the continuum is determined from a power law fit between $5.5{-}5.8\,\mu$m and $13.5{-}14.0\,\mu$m. The wavelength interval used for the continuum determination are, however, far away from the $9.7\,\mu$m silicate feature. We use the IDL routine POLYFIT to obtain the best linear fit to each AGN spectrum in $\log(S_\lambda) - \log(\lambda)$ space.

M82 Template. In order to account for the contribution of star-forming regions to the $5.5{-}14.5\,\mu$m spectra, we use the *ISO* SWS MIR spectrum of M82 from Sturm et al. (2000) as a starburst template spectrum, rebinned to the exact sampling of the individual low resolution spectra. In particular, this template is used to fit the broad PAH emission features found in the *Spitzer* IRS range, which are clearly seen in some of our objects. These features are typical indicators for recent star formation. In order to eliminate non-AGN emission, we subtracted the starburst template scaled with the strength of the aromatic features arising in the host or in circumnuclear SF.

Silicate Strength. We quantify the intensity of the silicate feature using the 'silicate strength', $S_{\rm sil}$ (e.g. Shi et al. 2006; Spoon et al. 2007; Maiolino et al. 2007), defined as:

$$S_{\rm sil} = \ln \frac{f_{\rm obs}(9.7\mu{\rm m})}{f_{\rm cont}(9.7\mu{\rm m})}$$

where $f_{\rm obs}(9.7\,\mu{\rm m})$ is the observed flux density at the peak of the $9.7\,\mu$m feature, and $f_{\rm cont}(9.7\,\mu{\rm m})$ is the underlying continuum flux density at the peak wavelength, extrapolated above the silicate absorption feature or below the emision feature. Positive values of $S_{\rm sil}$ indicate emission above the continuum, while negative values of $S_{\rm sil}$ indicate absorption. In absorption, this definition of feature strength corresponds to the apparent optical depth, i.e., $S_{\rm sil}$ is negative, so $f_{\rm obs} = f_{\rm cont} e^{-\tau_{app}}$, with $\tau_{app} = -S$.

The $9.7\,\mu$m feature has a measured center typically varying from 9.7 to $10.0\,\mu$m in

absorption and often exceeding $10.0\,\mu$m in emission, for this reason, the wavelength at which $S_{\rm sil}$ is evaluated, is not fixed. We evaluated $S_{\rm sil}$ between $9.2-10.3\,\mu$m or $8.0-12.6\,\mu$m, depending on the spectrum type (emission, absorption, or PAH emission). We measure the strength $S_{\rm sil}$ after continuum and scaled M82 template subtraction.

Continuum Emission at 6.7 μm. We determine a continuum at $6.7\,\mu$m rest wavelength evaluating the fitted continuum at that wavelength. At this rest-frame wavelength we have data for all sources. Moreover, it is far from the silicate feature and in-between PAH features. In this manner, the determination of $L(6.7\,\mu{\rm m})$ should be little affected by uncertainties in the subtraction of the starburst component. In order to characterize the energetic output of our sources, we measure the monochromatic flux (f_λ) and luminosity, $L_{6.7} = \lambda L_\lambda(6.7\,\mu{\rm m})$ from our spectra.

The resulting $9.7\,\mu$m silicate strength and derived $\log \lambda L_\lambda(6.7\,\mu{\rm m})$ luminosities for our sample can be found in Table C.1. Figure 4.2 depicts the IRS spectra shifted to the rest frame ($5.0-15.0\,\mu$m) with the best fit of PG0050+124, ESO103-G35, and IC5135, which serve as examples of continuum-, absorption-, and PAH-dominated spectra.

The MIR spectra of the objects in our sample show great variety. The radio-quiet quasar spectra show silicate features in emission and absorption at $10\,\mu$m. For the Seyfert 1 spectra, the $10\,\mu$m silicate feature is in emission and absorption. The spectra of Seyfert 2s indicate even stronger PAH emission features. The silicate feature at $10\,\mu$m is in absorption but also in emission. In the radio-loud quasar spectra, the $10\,\mu$m silicate feature is in emission, the same for BAL quasar. The spectra of LINERs and FR II radio galaxies show emission and absorption at $10\,\mu$m. The silicate strengths reveal features in emission ($S_{\rm Sil} > 0$) in 54 AGNs and features in absorption ($S_{\rm Sil} < 0$) in 68 AGNs.

4.3 Results

In the unified model of AGNs, the differences between types 1 and 2 objects are explained by a torus of dust and gas that obscures the broad line gas from some viewing angles while leaving it exposed from others. The dust in the torus is expected to absorb short-wavelength radiation from the nucleus and re-emit it in the MIR. A strong constraint on models aiming to explain and predict emission from the torus is the Si–O stretching mode near $\sim 10\,\mu$m.

Obscuration in AGNs is caused by a mixture of neutral and ionized gas, as well as dust. Absorption by gas is usually observed in the X-rays through the suppression of soft X-ray emission with an energy cutoff that increases with the gas column density, $N_{\rm H}$. Obscuration

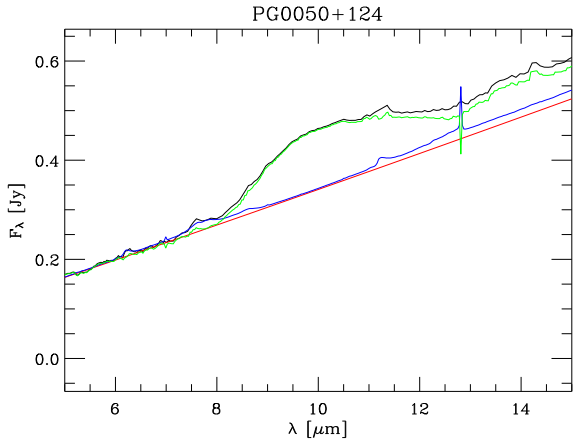

(a) Continuum spectrum

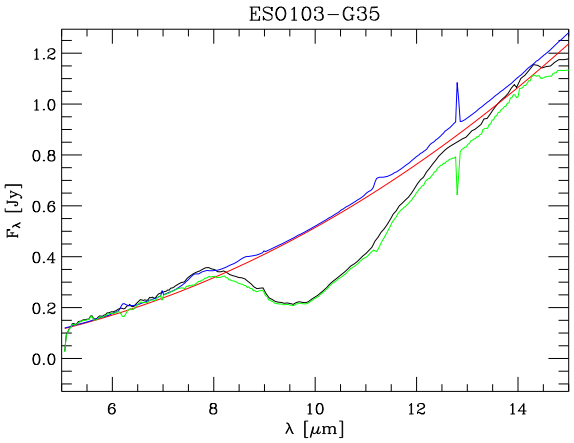

(b) Absorption spectrum

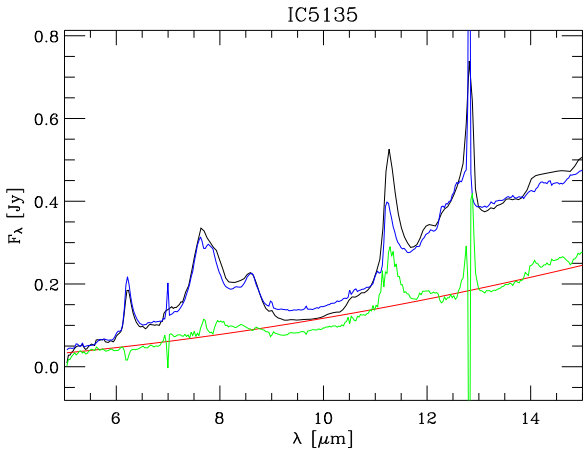

(c) PAH spectrum

Figure 4.2: *Spitzer* IRS spectra (black) of three objects with their corresponding fits. The red line is the fitted continuum, the blue line is the scaled M82 template, and the green line is the residual subtracting the scaled M82 template from the object spectrum.

by dust is usually observed at optical and IR wavelengths where the continuum and broad emission lines are reddened and in some cases, completely suppressed. In the NIR and MIR, dust obscuration interplays with thermal reemission from the parsec-scaled dust torus. Depending on the actual geometry, optical depth, and chemistry, dust absorption features at about 10 and 18 μm due to silicates can be present in the IR.

An edge-on view through cool dust in the torus causes a prominent absorption feature in type 2 AGNs. In type 1 AGNs, where hot dust at the inner surface of the torus is revealed, models often predict strong silicate emission. However, Spitzer observations of quasars have

established not only that the silicate emission feature is common in those objects (Hao et al. 2005, 2007; Siebenmorgen et al. 2005), but also that silicate emission is present in the average type 2 quasar spectrum (Sturm et al. 2006). Furthermore, silicate absorption is seen in some type 1 AGNs (Weedman et al. 2005).

It is very important to investigate the distribution of silicate strengths within a large sample of different types of AGNs. The distribution will provide insights into the geometry of the dusty structure, the optical depth of the clouds and the filling factor along the line of sight. If we combine these data with X-ray observations, we can explore the line of sight toward the central engine. Also, it is interesting to search for correlations between IR continuum and hard X-ray emission in order to test the unification scenario for AGN.

4.3.1 Dust covering factor as a function of X-ray luminosity

The covering factor is generally understood as the fraction of the sky, at the AGN center, covered by obscuring material. The covering factor of the circumnuclear dust can be estimated by comparing the thermal reprocessed emission from the torus and the primary AGN radiation emitted by the accretion disk. The circumnuclear IR emission is due to thermal radiation by dust heated by the nuclear UV source (the accretion disk), therefore, the MIR luminosity is a proxy of the nuclear FIR radiation. Hence, the MIR/UV ratio provides a measure of the nuclear dust covering factor. However, in the case of type 2 AGNs we cannot directly probe the UV luminosity (because are obscured). Yet, we can use the hard X-ray radiation (which can pierce large columns gas), corrected for the absorption measured in the X-ray spectra. Here we use the MIR−to−X-ray luminosity ratio to investigate the dust covering factor in the selected sample.

X-ray luminosity. The X-ray emission from AGNs is generally assigned to the nuclear engine itself. Hard X-rays (2−10 keV), can penetrate high column densities of gas and dust clouds and suffer minimal contamination by emission from the host galaxy. In the case of very high obscuring gas column densities, $>10^{24}\,\mathrm{cm}^{-2}$, Compton scattering by bound electrons becomes important. This mechanism blocks photons with energies below 10 keV at the rest frame. If an AGN lies behind such high columns densities, one can only expect to detect them indirectly in the 2−10 keV band.

The X-ray data used in this work have been carefully selected from published studies. All observed X-ray fluxes in the 2−10 keV band have been converted to absorption corrected

2−10 keV fluxes using the simulation tool PIMMS[5]. In order to get the corrected flux we need the following data: Galactic column density $N_{\rm H}^{\rm gal}$, redshift, intrinsic column density $N_{\rm H}$, and the photon index Γ; these values were taken from the references given in Table C.1.

The calculation of the X-ray luminosity (corrected for intrinsic absorption) is based on the formula

$$L_X = 4\pi D_L^2 F_X[2-10\ \mathrm{keV}]$$

where D_L is the luminosity distance and F_X is the flux corrected for absorption. This should be a measure of the true intrinsic 2−10 keV AGN power responsible for heating the torus clouds. As we can expect, in cases of extreme obscuration, these corrections can have large uncertainties.

The intrinsic X-ray flux cannot be recovered when only a $N_{\rm H}$ lower limit value is inferred; this is the case for a totally Compton thick AGNs (those in which the X-ray obscuring matter has a column density equal to, or larger than, the inverse of the Thomson cross-section, $N_{\rm H} \geq \sigma_T^{-1} = 1.5{\times}10^{24}\,\mathrm{cm}^{-2}$), which are absorbed at all energies or which are lacking data at $E > 10$ keV, i.e., for which any transmitted flux at high energy cannot be probed. These objects were not taken into account when calculating the intrinsic (absorption-corrected) X-ray luminosity, because only a small part of the broad−band X-ray flux is transmitted, therefore to estimate the intrinsic luminosity is highly uncertain.

MIR luminosity. In the MIR range (∼4−10 μm) the contrast between AGN-heated dust emission and other components is maximal. This spectral region contains various spectral features, like PAHs and silicates. By focusing on the continuum emission at 6.7 μm, the uncertainty in the removal of PAH emission is minimized, while the contribution from the silicate features is negligible at this wavelength. If the spectral shape of the AGN-heated dust does not change from object to object, the 6.7 μm emission is a proxy of the global circumnuclear hot dust emission.

The continuum luminosity at the rest frame wavelength of 6.7 μm is given by

$$\lambda L_\lambda(6.7\ \mu\mathrm{m}) = 4\pi \mathrm{D_L^2} \lambda_{\rm obs}(6.7\ \mu\mathrm{m}) \mathrm{F_{obs}}(6.7\ \mu\mathrm{m})$$

The MIR emission of an AGN is dominated by thermal emission of the dust within the torus. As the torus is heated by the accretion disc, one would expect a correlation between MIR and hard X-ray luminosities.

As is commonplace, the X-ray column density can be used to classify AGNs into type 1 (direct view of the AGN; $N_{\rm H} < 10^{22}\,\mathrm{cm}^{-2}$) and type 2 (obscured view of the AGN; $N_{\rm H} >$

[5]See http://heasarc.gsfc.nasa.gov/Tools/w3pimms.html

$10^{22}\,\mathrm{cm}^{-2}$). In Figure 4.3, we plot the rest frame $6.7\,\mu$m luminosity L_{MIR} versus the intrinsic $2-10\,$keV luminosity on a $\log-\log$, split into type 2 AGNs (red triangles) and type 1 AGNs (black triangles).

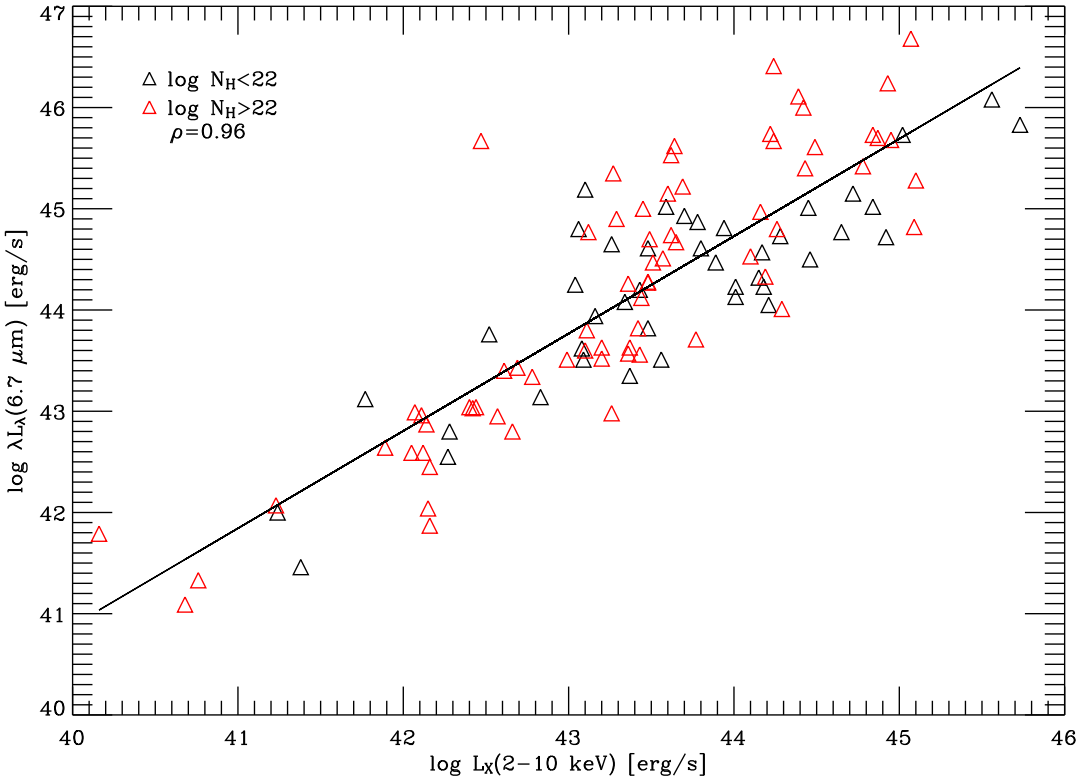

Figure 4.3: Correlation of MIR and intrinsic $2-10\,$keV X-ray luminosities, along with best fit (in $\log-\log$ space). We divided our AGN sample into type 1 (black triangles) and type 2 (red triangles) AGNs.

Nuclear $2-10\,$keV X-ray and MIR continuum luminosities are significantly correlated, suggesting a strong coupling between the X-ray and MIR emission mechanisms. The former is commonly ascribed to a disk-corona system and the latter is due to AGN emission reprocessed by dust. The correlation between these two quantities has a high statistical significance; the Spearman-rank coefficient is $\rho = 0.962$ at a significance level of 9.08×10^{-19}. The best power law fit ($\log L_{\mathrm{MIR}} = a + b \log L_X$) to the whole sample is

$$\log[\lambda L_\lambda(6.7\ \mu\mathrm{m})] = 2.41 + 0.82\log[\mathrm{L_X}(2-10\ \mathrm{keV})]$$

where luminosities are expressed in $\mathrm{erg\,s^{-1}}$, following the non-linear relation $\lambda L_\lambda(6.7\ \mu\mathrm{m}) \propto \mathrm{L_X}(2-10\ \mathrm{keV})^{0.82}$, which indicates that the MIR reprocessed emission increases more slowly than the primary luminosity.

Both type 1 and type 2 AGN closely follow the same correlation, in other words, there is no significant difference between type 1 and type 2 AGN as would be expected from an optically and geometrically thick torus dominating the MIR AGN continuum. Lutz et al. (2004) attributed this similarity to an extended dust component, since significant non-torus contributions to the AGN MIR continuum could mask the expected difference between the two types of AGN. Moreover, we found the slope to be in good agreement with Maiolino et al. (2007), with the difference they used optical luminosities instead of X-ray luminosities.

This result is in agreement with previous studies. Lutz et al. (2004) reported a tight correlation between the rest frame $6\,\mu\mathrm{m}$ luminosity and the absorption-corrected hard X-ray luminosity for a sample of 71 AGNs using ISO low resolution spectra; this sample does not contain Compton thick objects. Recently, Horst et al. (2008) found a strong correlation between the rest frame $12.3\,\mu\mathrm{m}$ and $2-10\,\mathrm{keV}$ luminosities of a sample of 25 AGNs (10 Sy 1, 11 Sy 2 and 4 LINERs); in addition they found that Sy 1 and Sy 2 nuclei have the same distribution of $L_{\mathrm{MIR}} \propto L_{\mathrm{X}}^{1.04}$. Maiolino et al. (2007) found the MIR continuum luminosity at $6.7\,\mu\mathrm{m}$ correlates with the optical continuum luminosity at $5100\,\mathrm{\AA}$ in a sample of 25 high luminosity quasars combined with low luminosity type 1 AGNs, following the non-linear relation $\lambda L_\lambda(6.7\ \mu\mathrm{m}) \propto \lambda \mathrm{L}_\lambda(5100\,\mathrm{\AA})^{0.82}$.

The ratio of $L_\lambda(6.7\,\mu\mathrm{m})$ and $2-10\,\mathrm{keV}$ X-ray luminosity is used as an approximate indicator of dust covering factor. There is a strong debate about the geometry and characteristics of the surrounding dust in AGNs, in particular whether it has a smooth (see Pier & Krolik 1992; Granato & Danese 1994; Schartmann et al. 2005) or clumpy (see Hönig et al. 2006; Krolik & Begelman 1988; Nenkova et al. 2002, 2008b; Schartmann et al. 2008) distribution. The ratio of IR to X-ray luminosity can be used to distinguish between these two distributions and to constrain the dust geometry (Lutz et al. 2004). For example, smooth torus models predict large differences in the IR to X-ray ratio for obscured and unobscured sources due to the significant effects of self-absorption; whilst radiation transfer models of clumpy dust tori predict very small or no differences between the IR to X-ray ratio for obscured and unobscured AGNs.

If the attenuating gas and dust around an AGN was strictly responsible for the thermal IR emission, then a correlation might be expected between the relative strength of the IR flux and the absorbing column density. That is, the most obscured sources should produce

the largest MIR/X-ray luminosity ratio, and a decrease of dust covering factor value for more powerful sources. Figure 4.4 shows the MIR/X-ray luminosity ratio vs. the intrinsic hard X-ray luminosity separated into type 1 and type 2 AGN. We do not find any correlation between the $L_{\rm MIR}/L_X$ and L_X. We compute the Spearman rank coefficient and we obtained a result of ρ =-0.044 at a significance level of 0.64, which clearly means no evidence for a correlation between the two quantities. No differences were found in the MIR to X-ray ratio between type 1 and type 2 AGN, which means there is not a dependency on AGN type and luminosity, according to previous results (Lutz et al. 2004; Sturm et al. 2006). The fact that all types of AGNs follow the same distribution suggest a similar origin of the MIR radiation in all these AGN classes.

Horst et al. (2008) performed an analysis using 25 AGN (Sy 1, Sy2, LINERs) and, in a good agreement with our work, they do not found any dependence of $L_{\rm MIR}/L_X$ on L_X. In their sample, Sy 1 and Sy 2 have the same distribution of $L_{\rm MIR}/L_X$, implying that the similarity is most probably intrinsic to the AGN and not due by extranuclear emission contaminating the MIR flux, which is best explained by clumpy torus model; the result found by Horst et al. (2008) also is seen in our data.

Nevertheless, in the quasar regime Maiolino et al. (2007) analyzed a sample of 25 luminous quasars (type 1) and they combined this sample with lower luminosity, type 1 AGNs. They found an anti-correlation between $L_{\rm MIR}/L_{\rm optical}$ and optical luminosity, i.e., the covering factor of the dust surrounding the AGN decreases with luminosity. A decreasing dust covering factor as a function of luminosity traslates into a decreasing fraction of obscured AGNs as a function of luminosity. Wang et al. (2005) used a sample of 50 radio-quiet PG quasars with $2-10$ keV X-ray and IR observations (IRAS and ISO) from literature to infer their dust covering factor, and they found the covering factor decreases as a function of X-ray luminosity.

If we plotted separately the different types of AGNs, a tendency to decrease the dust covering factor with the intrinsic X-ray luminosity is seen in types 1. On the contrary, there are no trend in types 2. In Figure 4.4b, the black line depicts the best power law fit for type 1 objects, with $\log(L_{\rm MIR}/L_X) = 8.74 + (-0.42)\log L_X$, the Spearman-rank coefficient ρ =-0.19 at a significance level of 0.0057.

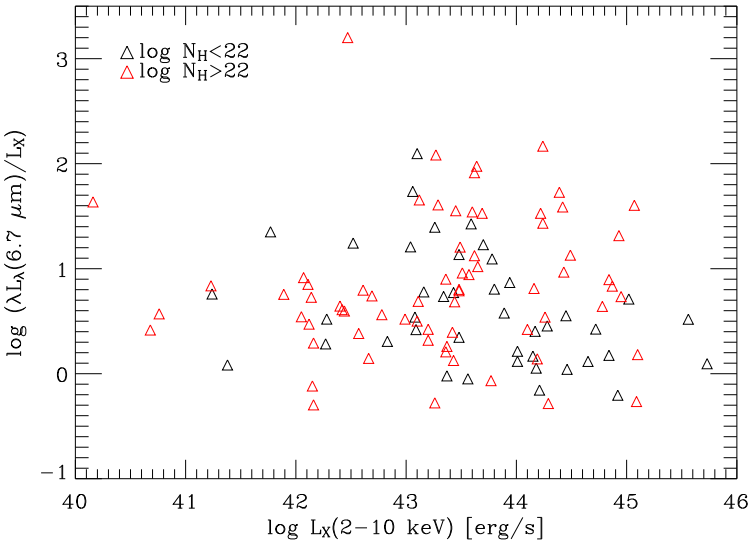

(a) All the sample

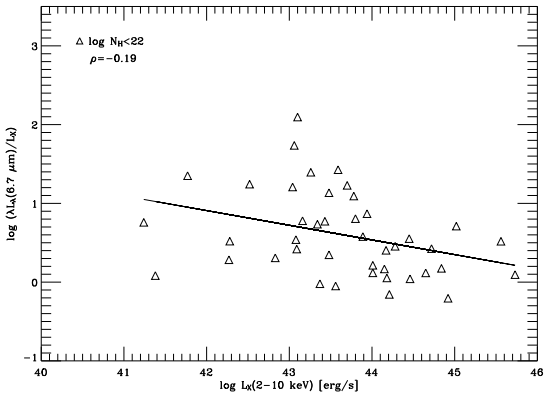

(b) Type 1 AGN

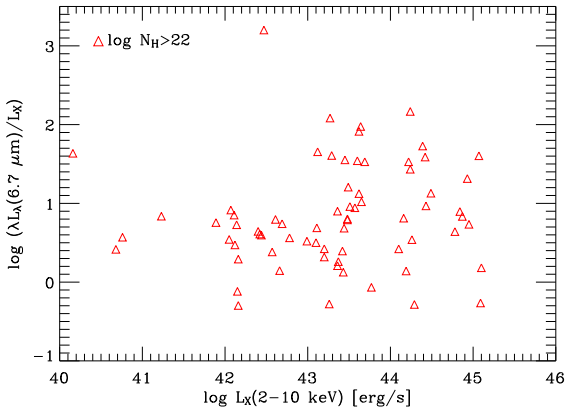

(c) Type 2 AGN

Figure 4.4: Logarithmic luminosity ratio versus X-ray luminosity separated into type 1 and type 2 AGNs.

4.3.2 Strength of the silicate feature as a function of HI column density

Silicates are a major constituent of interstellar and circumstellar dust. Silicate dust specifically dominates the MIR spectra of galaxies. Their presence is indicated by two strong spectral features: one due to an Si−O stretching mode and peaking at around 10 μm and another due to an O−Si−O bending mode and peaking at around 18 μm. A view of a hot,

optically thin surface produces the emission features, and a view through a cold screen shows the absorption features.

It is important to determine the relationship between the gas column density and dust column density in the obscuring material in AGNs. The column density of neutral gas can be directly probed by X-ray observations. The strength of the silicate feature would be a direct measure of the dust optical depth along the line of sight. The intrinsic gas column densities responsible for absorption in the hard X-rays were collected from the literature. In Table C.1 we list the observed X-ray fluxes, the intrinsic column densities and the X-ray luminosities corrected for absorption.

Shi et al. (2006) observed a sample of 97 AGNs with IRS (*Spitzer* Space Telescope) in order to study the 9.7 μm silicate feature. However, they used only 85 objects which have available HI column densities. Measuring the silicate absorption depth they found the HI column density roughly correlates with silicate feature strength.

We investigate the relation between 9.7 μm silicate feature and X-ray column density, which measures directly the absorption in AGNs. We use 76 objects from Shi et al. (2006)'s sample. In addition, we included objects from other samples (Buchanan et al. 2006; Ruiz et al. 2007; Sirocky et al. 2008; Sturm et al. 2006; Teng et al. 2008; Weedman et al. 2006), giving a total of 122 AGNs. We estimated the silicate feature strengths fitting the continuum in a different way to Shi et al. (2006). We also use a starburst template to remove the aromatic features (see §4.2) whereas Shi et al. (2006) only removed the narrow emission lines.

A correlation was found between the silicate feature strength and the X-ray absorption column density in a sense that low HI column densities correspond to silicate emission and high HI column densities correspond to silicate absorption, according to

$$S_{\rm sil} = 2.58 + (-0.050)\log(N_{\rm H})$$

and shown as green line in Figure 4.5. Spearman-rank coefficient is ρ = -0.57 at a significance level of 8.37×10^{-12}. This trend is consistent with the AGN unification scheme, where material surrounding the central supermassive BH obscures both the X-ray and silicate emission.

According to Shi et al. (2006), the features vary from emission to absorption as the X-ray spectra become more heavily obscured. Their lineal fit for all types of AGNs is given by

$$S_{\rm sil} = 3.3 + (-0.15)\log(N_{\rm H})$$

This result disagree with ours; the discrepancy is partly due to the $N_{\rm H}$ value compiled by Shi et al. (2006), which were mistaken because some of the Compton thick sources were

erroneously classified as Compton thin or there were $N_{\rm H}$ simply erroneously compiled, and partly to our much larger statistics. However, the trend is similar in the sense that low HI columns correspond to silicate emission, while high columns correspond to silicate absorption.

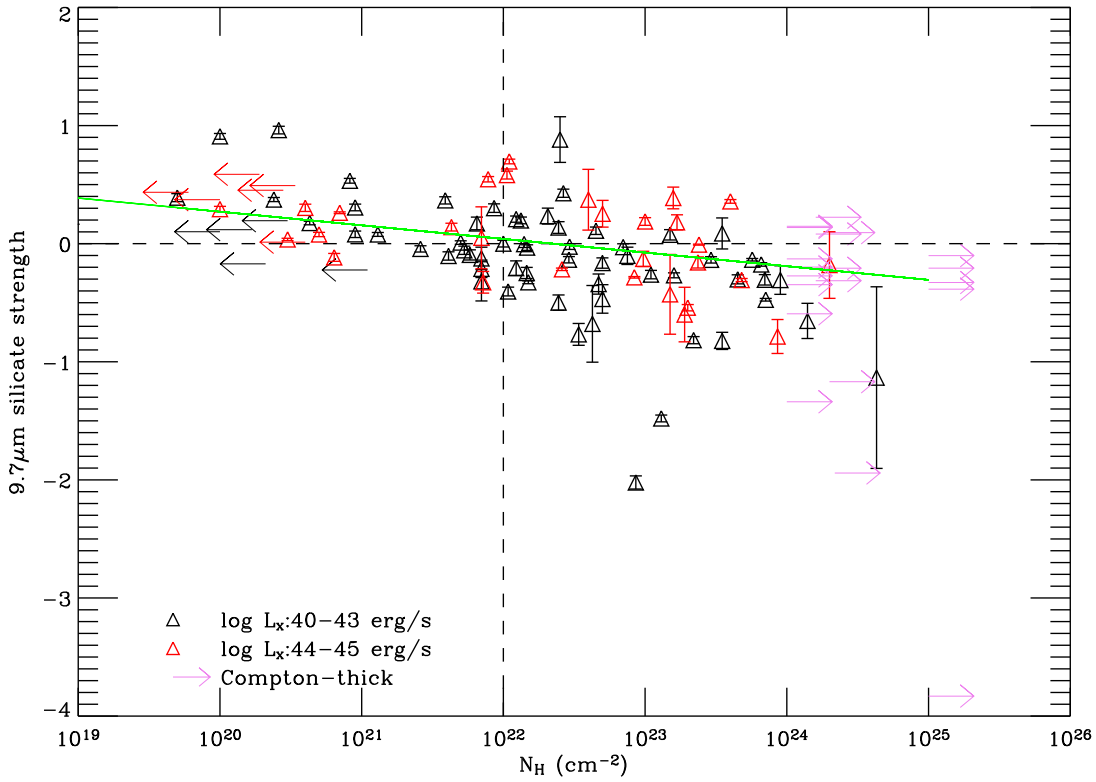

Figure 4.5: Strength of the 9.7 μm silicate feature as a function of intrinsic column density determined from X-ray observations, in X-ray luminosity bins. Right arrows indicate sources consistent with being Compton Thick AGNs. For these sources we plot the lowest limit for the $N_{\rm H}$ parameter. Left arrows indicate sources with upper limit for the $N_{\rm H}$ parameter. The green line represent the linear fit to the data.

In AGN unified theory, type 2 AGN displays silicate absorption bands whereas in type 1 AGN the silicate features are in emission. Figure 4.5 shows several type 2 AGN with emission features at 9.7 μm; also note that some Compton thick AGNs have silicate emission and others do not show deep silicate absorption. These results are not expected from the simplest unification scenario, although some AGN models can accommodate such exceptions (Nenkova et al. 2002, 2008a,b; Schweitzer et al. 2008).

A similar result was obtained by Shi et al. (2006) but with fewer objects. The detection of silicate emission even in type 2 AGNs suggested that part of the silicate emission may originate in the NLR. The presence of dust in the NLR of an AGN nucleus can explain why silicate features appear in emission in both luminous type 2 and type 1 (Efstathiou 2006).

Shi et al. (2006) proposed a circumnuclear disk model to explain the result of Figure 4.5. The model includes an inner accretion disk (<0.1 pc in radius) which produces X-ray and UV radiation ionizing the NEL and BEL clouds, and heating the dust; a middle disk (0.1−10 pc in radius) with a dense diffuse component and with embedded denser clouds; the diffuse component produces the silicate emission, while the embedded clouds obscure the central X-ray emission; and an outer clumpy disk (10−300 pc in radius) with clouds obscuring the silicate and X-ray emission, and responsible for the silicate absorption. The similarity of the behavior of various types of AGNs suggest that this disk geometry may be typical for AGNs in general.

Although the relation between silicate strength and $N_{\rm H}$ absorption obtained by us is somewhat different from Shi et al. (2006), the qualitative behavior is similar, and in particular our result are still consistent and support their model. Moreover, the similarity of the behavior between AGN of different luminosity obtained by us (see Figure 4.5) suggest that this scenario applies at all luminosities.

4.3.3 The 7.7 μm PAH SFR indicator

SF properties of galaxies are essential in assessing their evolutionary histories. Estimates of the SFR in galaxies at all redshifts are key indicators of the efficiency and mechanical feedback effects of SF activity, of chemical evolution of the ISM and intergalactic medium, and of cosmic SF history.

Different tracers for SF are used based on integrated colors, the UV continuum, recombination and forbidden lines, and FIR emission continuum (e.g. Kennicutt 1998, and references therein). PAH emission in the MIR may also provide a convenient tracer of SF activity (Schweitzer et al. 2006; Shi et al. 2007). PAHs are stochastically heated mainly by UV photons produce by massive stars. Assuming fixed emission, absorption and PAH abundance, the PAH emission is a measure of the amount of photons available between 6 and 13.6 eV (the former corresponding to the averaged ionization potential of PAHs) and hence of SF.

PAH emission. Many Galactic and extragalactic objects show strong broad features

at $3-13\,\mu$m, which are thought to originate from small carbonaceous dust particles. These emission features are due to PAH molecules containing $\sim$10 to 1000 carbon atoms. The different features arise from different C−C and C−H stretching/bending vibrational modes. We focus on the $7.7\,\mu$m feature as it is usually the strongest and this spectral region is observed in all of our sample.

SFR are estimated for individual sources from the luminosity of the $7.7\,\mu$m PAH feature. The $7.7\,\mu$m PAH flux is measured by fitting a gaussian profile to the M82 template with continuum subtracted, and a linear continuum computed over a wavelength range of roughly $6.6-6.9\,\mu$m and $9.0-9.5\,\mu$m. The $7.7\,\mu$m PAH flux is then multiplied by the scaled M82 template of each object in order to obtain the final flux. We measure the luminosity of the $7.7\,\mu$m PAH emission to quantify the star formation contribution, which is obtained from F_{PAH}, defined as

$$L(PAH_{7.7\ \mu\mathrm{m}}) = 4\pi D_L^2 F(PAH_{7.7\ \mu\mathrm{m}})$$

The SFR determines the number of young, massive stars, which provide the UV photons to excite both PAH molecules and dust grains. If they are excited by the same photons, PAHs could potentially be used as quantitative tracers of the SFR. In this study, we use the MIR aromatic features to quantify the SFR in AGN host galaxies. We translated the $7.7\,\mu$m PAH luminosity into SFR using (Maiolino et al. 2007)

$$SFR[M_\odot\,\mathrm{yr}^{-1}] = 3.46\times10^{42} L(PAH_{7.7\ \mu\mathrm{m}})[\mathrm{erg\,s}^{-1}]$$

We want to determine how AGN activity and SF are related. In order to investigate such relation, we use the X-ray emission which is associated with the accretion process and known to be originated closer to the BH, and an indicator of the SFR. Figure 4.6 shows the SFRs of our AGN sample, as traced by the PAH luminosity, versus hard X-ray luminosity, these two quantities are indeed positively correlate based a Spearman-rank correlation coefficient of $\rho = 0.71$ and a linear fit with a 0.68 slope. The relation between SFR and X-ray luminosity, which traces BH accretion, is in agreement with the expectation of models on the co-evolution of BH and galaxies.

There have been some recent claims that an obscured phase, coupled with enhanced SF, may represent an early stage in the subsequent evolution of AGN (Polletta et al. 2008). In order to test this scenario, we have separated the objects in type 1 and type 2 AGNs. We find the absorbed sources span the same range of SFR as the unabsorbed AGNs, compatible with the unified model which expects that obscured and unosbcured AGNs have the same SFR. Some luminous type 2 AGNs (associated with nuclear obscuration) show enhanced SFR

possibly due to different physical mechanisms for triggering mass accretion onto supermassive BHs.

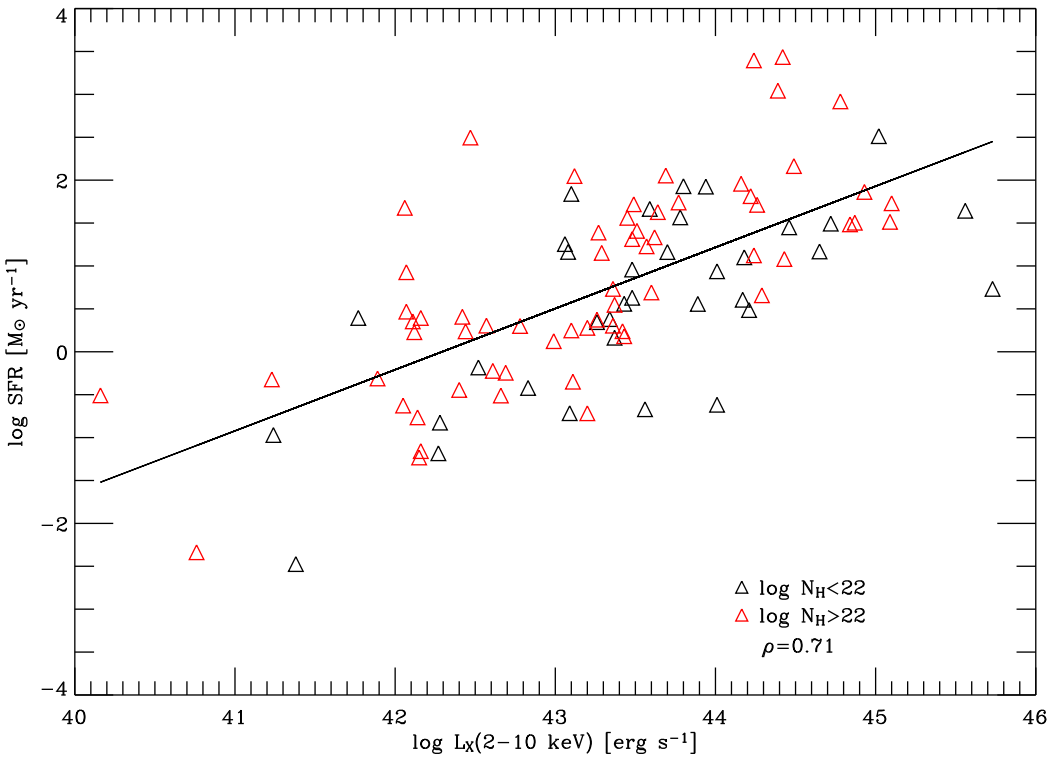

Figure 4.6: Logarithm of the SFR deduced from the PAH luminosity versus logarithm of the absorption-corrected hard X-ray luminosity. Red triangles mark type 2 AGNs and black triangles mark type 1 AGNs. SFR correlates with X-ray luminosities. Line is the best fit from linear regression (in $\log - \log$ space).

Our sample shows weak trend for the dust covering factor as a function of SFR, cf. Figure 4.7. It seems that dust covering factor increases with the SFR, but with significant dispersion. The resulting Spearman-rank coefficient is $\rho = 0.48$ (9.4×10^{-7}), where the number in parenthesis gives the probability for the correlation coefficient to deviate from zero; this means that the correlation is weak. In particular, it is interesting the lack of sources with large covering factor and low SFR.

The Figure 4.7 suggest that SFR in the host galaxy and in the circumnuclear region help to increase the dust covering factor around the nuclear source. Probably SFR through SN stir the ISM allowing clouds to lose angular momentum drifting to the center to cover the

nuclear source more effectively.

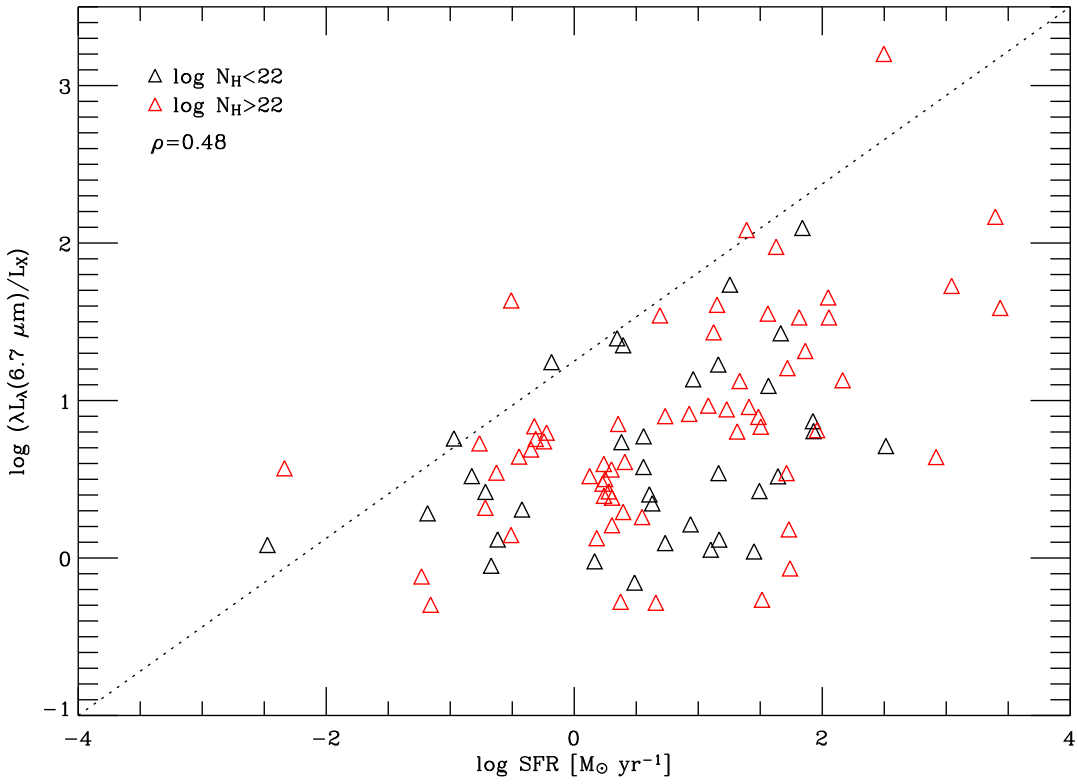

Figure 4.7: MIR to X-ray luminosity $[\lambda L_\lambda(6.7\,\mu\mathrm{m})]/[L_X(2{-}10\,\mathrm{keV})]$ versus SFR. Red triangles mark type 2 AGNs and black triangles mark type 1 AGNs. The dotted line it is not a fit.

As discussed in section §4.3.2, the silicate strength provides a tool to measure the dust absorption towards the nuclear source. Figure 4.8 shows the 9.7 μm silicate feature strength compared with the SFR. In Figure 4.9, we plot the X-ray absorption versus the SFR for our sample of AGNs. There is no clear tendency between N_H and SF. As can be seen from the figure, a number of highly obscured AGNs ($N_\mathrm{H} > 10^{22}\,\mathrm{cm}^{-2}$) do not represent high SFRs.

Figures 4.8 and 4.9 suggest that the column of dust (silicate feature) and column of gas (N_H) we do not correlate with the SFR, although the dust covering factor does show a weak correlation with SFR.

These combined results are somewhat puzzling, and may provide some clues on the way gas and dust are arranged and funneled into the nuclear region. However, more data and larger statistics are required to obtain further insight into this issue.

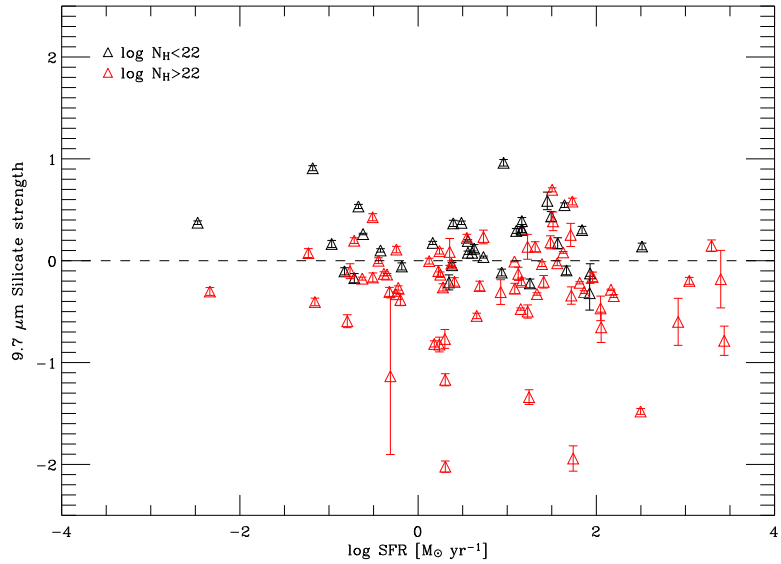

Figure 4.8: Strength of the 9.7μm silicate feature as a function SFR separated into type 1 and type 2 AGNs.

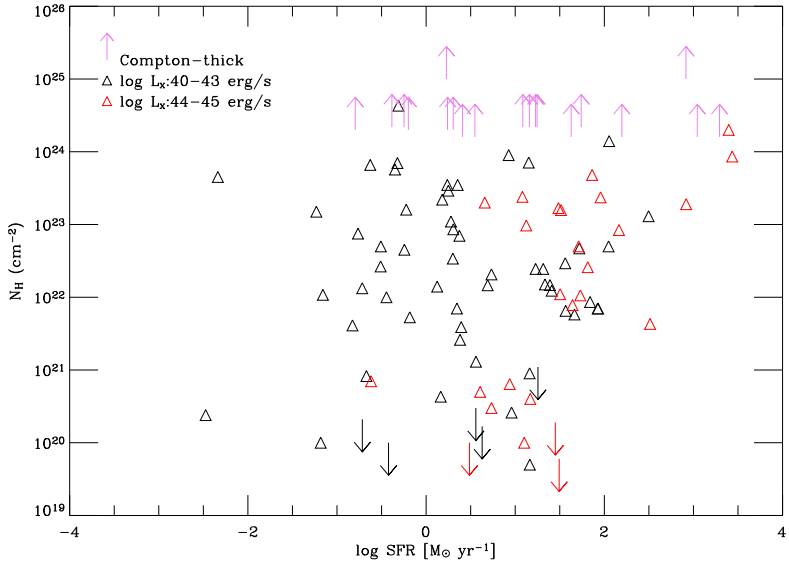

Figure 4.9: X-ray column densities versus SFR separated into two X-ray luminosity bins. Compton thick sources are marked as lower limits (upward arrow).

4.4 Summary

Hundreds of IRS spectra of AGNs are available in the *Spitzer* archive. In this chapter, we collected data from different *Spitzer* programs to summarize a wide variety of AGNs, which have available X-ray data. With the sample of AGNs we examine the MIR and X-ray luminosities, X-ray column densities, strength of silicate features, and SFRs. Our main results are listed as follows:

- The MIR continuum luminosity at $6.7\,\mu$m correlates with the absorption corrected hard X-ray luminosity. This correlation may imply that the gas and the dust are closely coupled together at all powers. Type 1 and type 2 AGNs have the same distribution of $L_{\rm MIR} - L_{\rm X}$, which is in agreement with the dusty torus. For these objects, the dust covering factor is estimated from the ratio between the MIR and X-ray luminosity. We do not find any dependence of $L_{\rm MIR}/L_{\rm X}$ on $L_{\rm X}$.

- We quantify the strength of the silicate feature at $\lambda \sim 9.7\,\mu$m keeping in mind that such measurement requires a careful determination of the continuum. The strength of the $9.7\,\mu$m silicate feature correlates with the intrinsic column density $N_{\rm H}$ estimated from X-ray data, consistent with unification models.

- SFRs are estimated from the luminosity of the $7.7\,\mu$m PAH feature. The AGNs display a relationship between SFR and $L_{\rm X}$, which indicates that more luminous AGNs have large SFRs. The dust covering factor as a function of the SFR shows a trend to increase, but the correlation is weak. No correlation was found between intrinsic column density and SFR nor silicate feature strength with SFR.

CHAPTER 5

CONCLUSIONS

In this work we presented IR and submm/mm observations in order to investigate the metallicity evolution and dust properties of AGNs. In particular, we used the rest-frame UV spectrum as it contains strong diagnostic emission lines useful to study in detail the ISM properties, such as metal abundances. In addition, we took advantage of the strong nuclear continuum to study the dust properties. In the following we summarize the main results obtained in this thesis, followed by some perspectives in future work.

- **The metallicity evolution.** Metallicity information on quasars is inferred from the analysis of their broad emission lines, which are very strong, but are emitted from a very small nuclear region. At $z > 5$ most of the emission lines used to constrain the BLR metallicity are redshifted into the NIR, as a consequence, the investigation of the BLR metallicity has been limited to a small number of objects.

  We investigated the (SiIV+OIV)/CIV ratio in a sample of 27 quasars at $4 \leq z \leq 6.4$. Lines were obtained from NIR spectra. This ratio is a very good metallicity tracer of the BLR, because CIV as a coolant decreases with the BLR metallicity. In particular, the abundances of iron and carbon, which depend on the delayed enrichment relative to α-elements, provide important information on the star formation history in quasar hosts.

  Our study reveals no correlation between this emission line ratio and redshift. We compared our results with the line ratios and metallicities inferred for lower redshift quasars (Nagao et al. 2006b). The relative intensity of the (SiIV+OIV)/CIV ratio remains constant over the wide redshift interval $2.5 \leq z \leq 6.4$, indicating the metallicity

in the observed quasars does not evolve with redshift. The apparent lack of evolution does not imply that the metallicity of the BLR in individual AGNs does not evolve with time. This effect probably results from a combination of the BH−galaxy co-evolution and from selection effects.

We found the BLR metallicity is very high even in quasars at $z \sim 6$. According to the calibration given in Nagao et al. (2006b), the observed ratios correspond to metallicities that are several times solar ($Z_{\rm BLR} \sim 7\, Z_{\odot}$, and in some cases approaching $Z_{\rm BLR} \sim 10\, Z_{\odot}$). These metallicities are not unrealistic, indeed, the BLR is a very small region[1] containing only $\sim 10^4\, {\rm M}_{\odot}$ of gas, it can be enriched to super-solar metallicities within less than 10^8 yrs by having less than one SN explosion every 10^4 yrs. The high metal abundances in quasars at high redshift ($z \sim 6$) require that the host galaxy has undergone a rapid and powerful SF event.

Our analysis also suggest a lack of evolution of the carbon abundance, contrary to the expectation that the carbon abundance should drop at $z > 5$, because stellar evolutionary timescales fall short of time to produce the observed carbon. In order to face this issue it is necessary a more accurate determination of the carbon abundance, which may come from future high spectral resolution optical/NIR or submm observations.

- **Dust mass evolution.** The warm dust, emitting at FIR wavelengths, is mostly heated by the UV radiation field of young massive stars in star forming regions. As a consequence, the FIR luminosity and submm emission are considered good tracers of SF in galaxies.

  We observed a small sample of quasars ($2.23 < z < 3.5$) with SCUBA/MAMBO ($850\,\mu$m/1.2 mm) to investigate their FIR properties. In order to study the FIR emission in a more robust way, we compiled from the literature a list of quasars observed a submm/mm wavelengths. Our final list, including observed and compiled, comprised 168 radio-quiet quasars in the redshift range $1.5 \leq z \leq 6.4$.

  The FIR luminosity ($L_{\rm FIR}$) provides a reasonable measure of the active formation of massive stars. Assuming a dust temperature of 47 K and an emissivity index β =1.6, we estimated the FIR luminosity considering a graybody spectrum. The observational data imply FIR luminosities of $\sim 10^{13}\, L_{\odot}$ in the submm/mm detected sources. We found that there is no apparent differences in the FIR luminosities of quasars at $z \sim 2$

[1] Size less than a few pc in the most luminous quasars.

and $z > 4$, i.e., there is no evidence of a redshift evolution of the FIR luminosity.

There is increasing evidence that the growth of central supermassive BH and the formation of the first stellar populations are closely linked. The relationship between the starburst activity of the host galaxy and the activity of the massive BH in high redshift quasars, can be investigated through the FIR luminosity and determining the BH mass. We estimated the BH mass using the CIV, MgII, and Hβ line witdths and continuum luminosity. We found a correlation between FIR luminosity and BH mass, implying that the most luminous objects have high BH masses.

We calculated the [OIII] luminosity in order to verify if the quasars with strong [OIII] emission are associated with enhanced submm/mm emission (powerful starburst activity). Our results show that the FIR luminosity increases with the [OIII] luminosity. Unfortunately, the sample is very small to provide a statistically robust result. More observations on the Hβ region of quasars are required to verify this trend.

Studies of emission and absorption lines in quasars at high redshift typically show they reside in metal-rich (at least $1\,Z_{\odot}$) environments, and that the more luminous objects may be more metal rich. However, the FIR luminosity shows no correlation against the metallicity, which probably indicates that current SF in quasar hosts is not a significant source of metal enrichment for the gas.

In order to confirm whether there is an evolution in the dust content, we have calculated the monochromatic luminosity at 1500 Å rest-frame. We found an important result: the FIR luminosity increases with UV luminosity, confirming the evolution in the dust content. Even more important, the FIR/UV ratio decreases towards higher redshifts, indicating an evolution in the dust mass at $z \sim 5$, which is in a good agreement with the theory of evolution and formation of dust. Nevertheless, it is mandatory to confirm this trend with observations with the next generation telescopes like LMT and ALMA, which claim to go an order of magnitude deeper and will be in operation in a few years.

- **MIR and hard X-ray luminosities, silicates features, and SFR in AGNs.** We explored the connection between X-ray emission from AGN and the MIR emission from the dust torus. In order to do it, we analyzed MIR *Spitzer* spectra for a sample of 127 AGNs (including radio-quiet quasars, radio-loud quasars, BAL quasars, FR II radio galaxies, Seyfert 1 and Seyfert 2 galaxies) at $0.001 \leq z \leq 2.54$, with available X-ray data. The AGN were grouped into unabsorbed (type 1) and absorbed (type 2) classes, depending on their X-ray absorption, in order to investigate the covering factor of the

circumnuclear dust, the silicate feature strength, and the SFR as traced by the PAH features.

The MIR continuum luminosity at $6.7\,\mu$m correlates with the intrinsic X-ray luminosity. Type 1 and type 2 objects have the same distribution of $L_{\rm MIR}$ vs. $L_{\rm X}$, result which is not compatible with the unified AGN scenario. The dust covering factor, as traced by the $L_{\rm MIR}/L_{\rm X}$ ratio, shows no clear trend with X-ray luminosity, which is in agreement with the clumpy torus models.

We found the silicate feature strength correlates with the HI column density as expected in the unified model, which predicts that low HI column densities correspond to silicate emission, while high columns correspond to silicate absorption. HI column densities are obtained from X-ray data and were collected from literature. This result is consistent with unification models where the large diversity in AGN properties is caused by viewing-angle−dependent obscuration of the nucleus.

We derived the SFR based only on the luminosity of the $7.7\,\mu$m PAH feature. We found that SFR increases with X-ray luminosity, in agreement with the expectation of models on the co-evolution of BH and galaxies. The dust covering factor as a function of the SFR shows a trend to increase. No correlation was found between intrinsic column density and SFR nor between silicate feature strength with SFR.

5.1 What is next?

Some possible areas of future research following the work presented in this thesis, are summarized as follows:

1. Metallicity evolution of high redshift quasars. From the SDSS and other large multiband surveys, there are now more than 20 $z \sim 6$ known quasars (mostly from SDSS, Fan et al. 2001, 2003, 2004, 2006; and Goto 2006; McGreer et al. 2006; Mortlock et al. 2008). In addition, the Canada-France High-z Quasar Survey has now discovered a total of 10 quasars at $z \geq 5.9$ (Willott et al. 2007, 2009). Therefore, NIR spectroscopic observations are necessary, in order to have a complete sample of high redshift quasars. The new high redshift spectra will be useful to measure the BLR metallicity, in order to combine these results with the already existing data. In addition, the central BH masses of high redshift quasars are important in understanding the growth of BHs and quasar accretion rates in the early universe. With the CIV line widths (and MgII) and continuum luminosities, we will be

able to calculate the BH masses, as well as Eddington luminosity ratios, which will provide us a fundamental data set to study luminous quasars at $z \sim 6$ in the context of the growth of early BHs and their relation to galaxy formation.

2. Dust evolution in quasars. A natural extension of this work would be to observe all high redshift quasars ($z > 5$) at submm/mm wavelengths in order to investigate the FIR properties. The quasar sample used in this thesis only includes optically luminous quasars, in order to better quantify the submm/mm properties of high redshift quasars and the contibution of SF to their emission, we need also to observe optically faint quasars.

All these objects can to be observed with the new generation of sensitive IR/submm/mm facilities, which will allow us to take the analysis of quasars to the next step. The up-coming projects are: the Astronomical Thermal Emission Camera (AzTEC), which had a successful run on the JCMT and the Atacama Submillimeter Telescope Experiment (ASTE), and will be mounted on the 50 m diameter LMT for continuum observing at 1.1 mm. Herschel, a 3.5 m telescope, has two imaging instruments, the Spectral and Pothometric Imaging REceiver (SPIRE) and the Photodetector Array Camera and Spectrometer (PACS), which together cover the wavelength range 57−670 μm enabling us to put constraints on both sides of the FIR dust peak. And finally, within the next years we will see the commissioning of the ALMA and the JWST to provide exquisite sensitivity and resolution at the longest submm and shortest IR wavelengths, respectively, to trace the dust in normal to extreme star forming galaxies out to the highest redshifts. These projects will provide a key contribution to understand some issues in AGN evolution.

On the other hand, optical and NIR spectroscopic observations are needed for quasars with no available spectra in the SDSS database or data in the literature, in order to estimate the BH masses and Eddington ratios, because there are only a few objects with available data. This will allow us to confirm the trend found between FIR luminosity and BH mass, and to test if there is any trend between FIR luminosity and Eddington ratio, which was not found with the current available data.

In addition, observations of quasars where the Hβ region is shifted to the NIR or MIR are needed to calculate the [OIII] luminosity, and thus to verify the finding about the [OIII] emission is associated with enhanced SF in the host galaxy. Our sample is very small, but CanariCam[2] would be a good option.

[2]CanariCam is a MIR imager with spectrogroscopic, coronagraphic, and polarimetric capabilities, which will be mounted initially at the Nasmyth focus of the 10 m Gran Telescopio Canarias at the Roque de los Muchachos Observatory in La Palma (Canary Islands, Spain). CanariCam will work in the thermal infrared

between 7.5 and 25 μm.

APPENDIX A

QUASAR SPECTRA AT HIGH REDSHIFT

In this section we displayed the NIR spectra of quasars studied in this work. The green solid lines indicate the best fits to the emission lines, and the green dashed line indicated the best model fit to the power-law continuum. The red lines indicate the sums of all components. The residuum, subtracting the best fit from the quasar spectrum, is displayed at the bottom for each quasar's plot.

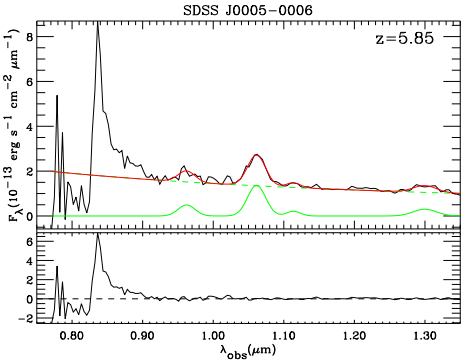

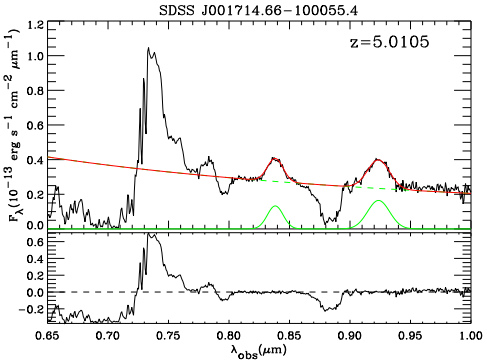

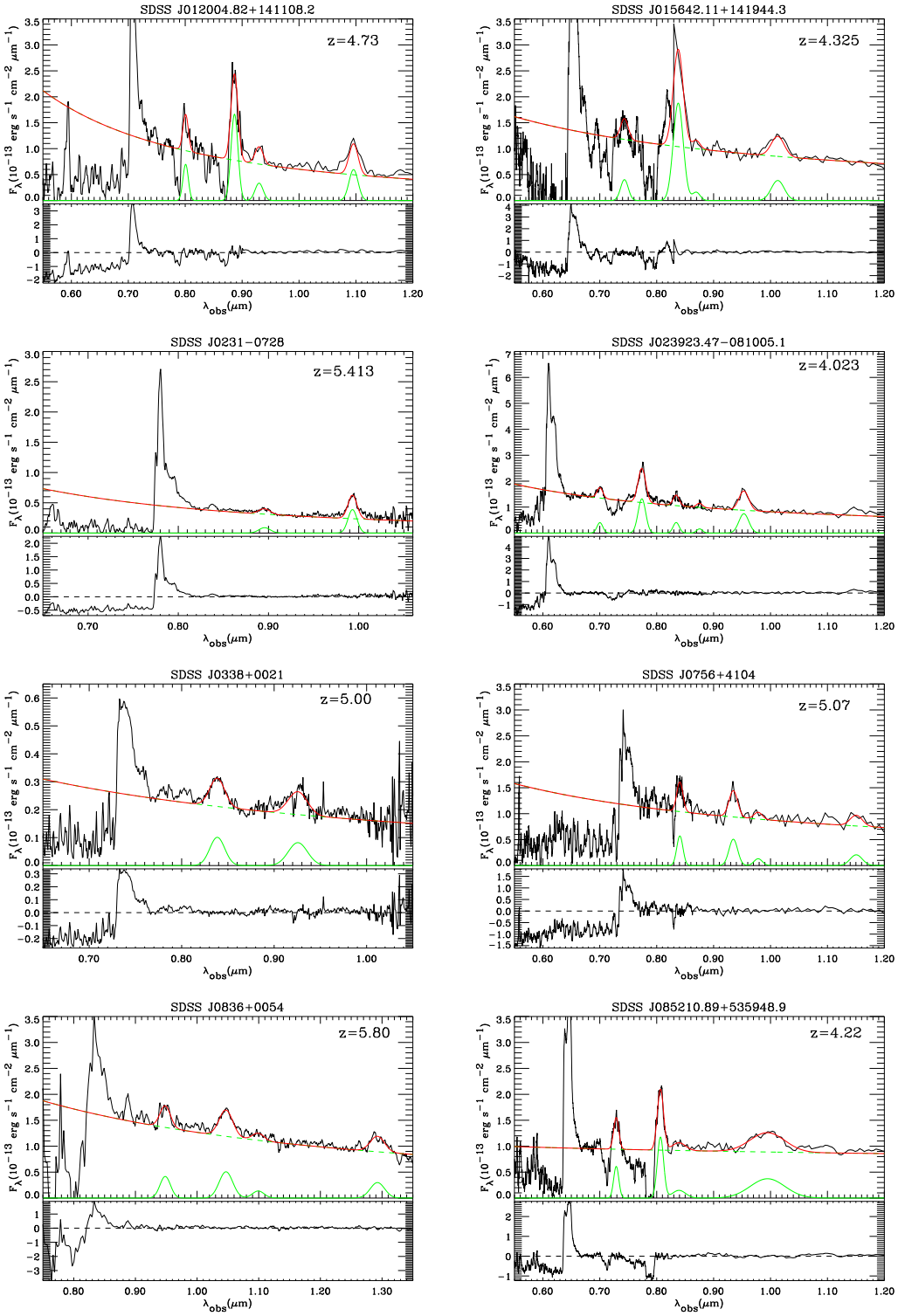
SDSS J012004.82+141108.2
z=4.73
SDSS J015642.11+141944.3
z=4.325
SDSS J0231−0728
z=5.413
SDSS J023923.47−081005.1
z=4.023
SDSS J0338+0021
z=5.00
SDSS J0756+4104
z=5.07
SDSS J0836+0054
z=5.80
SDSS J085210.89+535948.9
z=4.22
$F_\lambda(10^{-13}$ erg s^{-1} cm^{-2} μm^{-1})
$\lambda_{obs}(\mu m)$

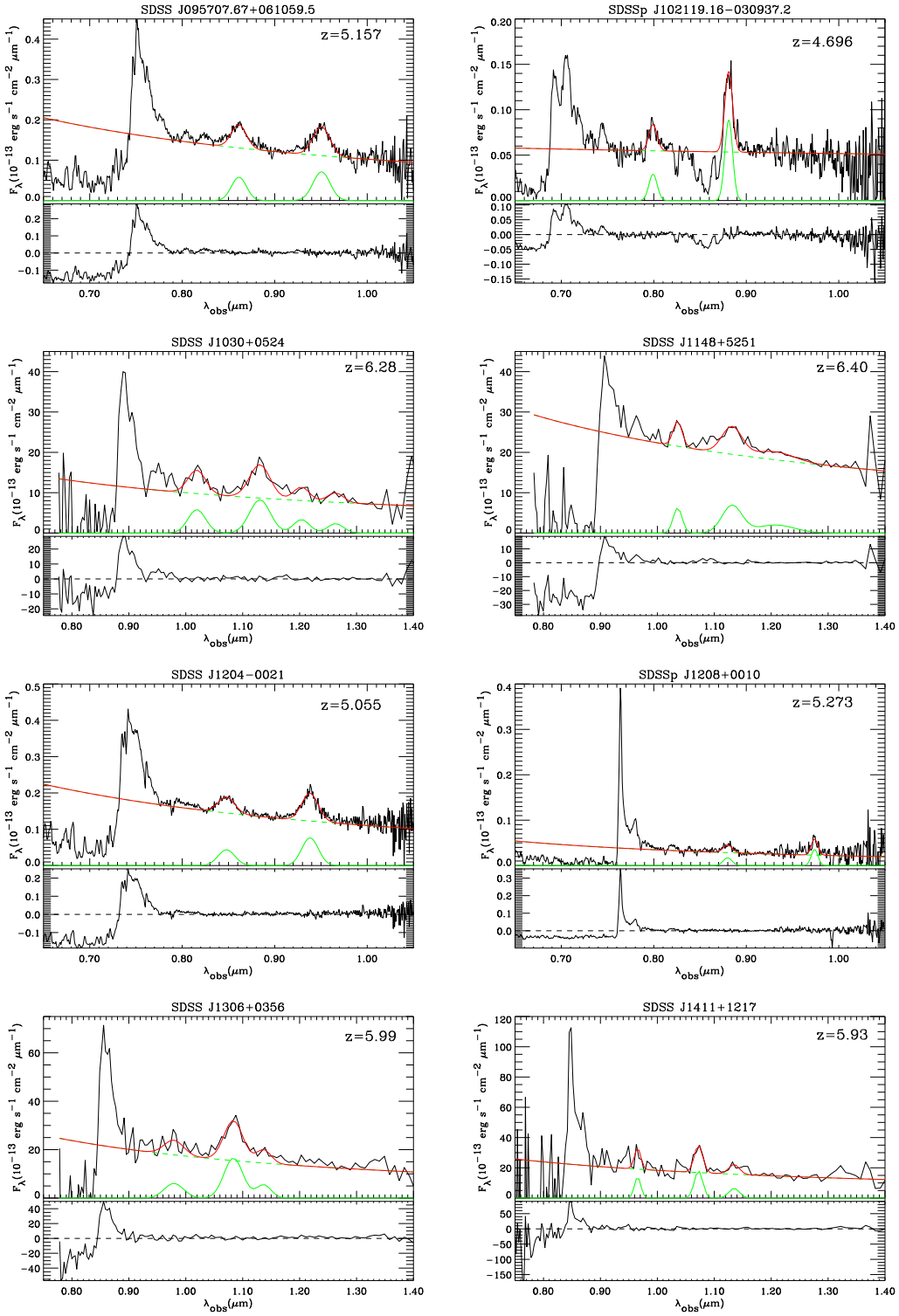
SDSS J095707.67+061059.5
z=5.157
SDSSp J102119.16−030937.2
z=4.696
SDSS J1030+0524
z=6.28
SDSS J1148+5251
z=6.40
SDSS J1204−0021
z=5.055
SDSSp J1208+0010
z=5.273
SDSS J1306+0356
z=5.99
SDSS J1411+1217
z=5.93
$F_\lambda(10^{-13}$ erg s^{-1} cm^{-2} μm$^{-1})$
$\lambda_{obs}(\mu m)$

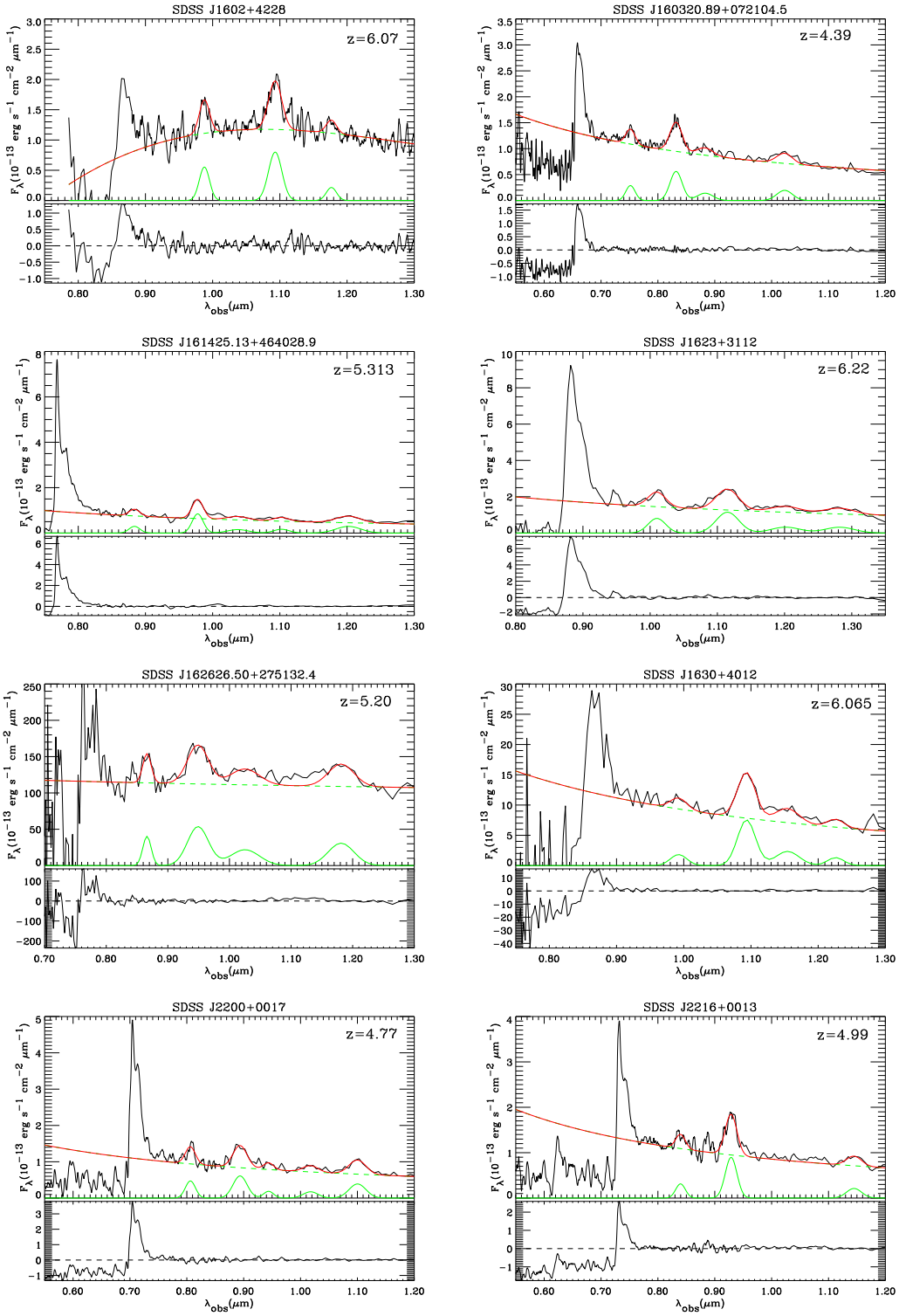
SDSS J1602+4228
z=6.07
SDSS J160320.89+072104.5
z=4.39
SDSS J161425.13+464028.9
z=5.313
SDSS J1623+3112
z=6.22
SDSS J162626.50+275132.4
z=5.20
SDSS J1630+4012
z=6.065
SDSS J2200+0017
z=4.77
SDSS J2216+0013
z=4.99
$F_\lambda(10^{-13}$ erg s^{-1} cm^{-2} μm^{-1})
$\lambda_{obs}(\mu m)$

APPENDIX B

PROPERTIES OF $Z > 1$ RADIO-QUIET QUASARS

Derived properties of the $z > 1$ radio-quiet quasars are shown in the following Tables. Also we collected data at low-z, to have a more complete study. These quasars were observed in the IR by Haas et al. (2000, 2003). Tabla B.4 shows the derived properties for the quasars at low-z (Haas et al. 2000, 2003). For these quasars (z <0.12), we calculated the arithmetic mean and the standard deviation of the mean.

$$\overline{L_{FIR}} = \frac{1}{n}\sum_{i=1}^{n} L_{FIR_i}$$

$$\sigma_{L_{FIR}} = \sqrt{\frac{\sum_{i=1}^{n}(L_{FIR_i} - \overline{L_{FIR}})}{n-1}}$$

and

$$\sigma_{\overline{L_{FIR}}} = \frac{\sigma_{L_{FIR}}}{\sqrt{n}}$$

Table B.1: Quasars observed at submm/mm

name	z	RA (J2000)	DEC (J2000)	$S_{850\mu m}$ (mJy)	$S_{1.2mm}$ (mJy)	Ref.
SDSSJ0002+2550	5.80	00 02 39.39	+25 50 34.8		0.20±0.88	9
LBQS B0009-0138	2.00	00 12 10.91	-01 22 07.7	2.2±2.8		1
LBQS B0013-0029	2.08	00 16 02.41	-00 12 25.2	3.2±3.3		1
LBQS B0025-0151	2.08	00 27 33.82	-01 34 52.4	4.8±2.47		1
J003525.29+004002.8	4.75	00 35 25.29	+00 40 02.8		0.3±0.5	3
HS B0035+4405	2.71	00 37 52.31	+44 21 32.9	9.4±2.8		1
SDSS0058+0115	2.54	00 58 14.31	+01 15 30.4	1.4±2.2	1.12±0.82	6
LBQS0109+0213	2.34	01 12 16.91	+02 29 47.6	4.7±2.2	0.66±0.79	6
J012403.78+004432.7	3.81	01 24 03.78	+00 44 32.7		2.0±0.3	3
J012650.77+011611.8	3.66	01 26 50.77	+01 16 11.8		-0.6±0.6	3
PSS J0134+3307	4.53	01 34 21.5	+33 07 55.4		3.5±1.5	5
J015048.83+004126.2	3.67	01 50 48.83	+00 41 26.2		2.2±0.4	3
J021102.72-000910.3	4.90	02 11 02.72	-00 09 10.3		0.5±0.3	3
SDSS J0231-0728	5.41	02 31 37.65	-07 28 54.5	1.8±1.6		8
J023231.40-000010.7	3.81	02 32 31.40	-00 00 10.7		1.8± 0.3	3
J025112.44-005208.2	3.78	02 51 12.44	-00 52 08.2		2.4±0.6	3
J025518.58+004847.6	3.97	02 55 18.58	+00 48 47.6		2.1± 0.4	3
RD J0301+0020	5.50	03 01 17.01	+00 20 26.0	1.9±1.5		8
BR B0300-0207	4.25	03 02 53.0	-01 56 07	-1.7±2.8		2
Q0302-0019	3.28	03 04 49.9	-00 08 13	-0.5±1.3	0.47±0.54	6
J031036.97-001457.0	4.63	03 10 36.97	-00 14 57.0		-0.5±0.4	3
J032608.12-003340.2	4.16	03 26 08.12	-00 33 40.2		1.5±0.4	3
J033829.31+002156.3	5.00	03 38 29.31	+00 21 56.3	11.9±2.0	3.7±0.3	3,8
BR B0351-1034	4.35	03 53 46.9	-10 25 19	-2.8±3.0		2
PSS J0747+4434	4.44	07 47 49.7	+44 34 16.0		0.1±1.2	5
HS 0749+4259	1.90	07 50 54.7	+42 52 19.0		1.3±0.9	4
HS B0752+3429	2.11	07 55 24.10	+34 21 34.2	2.4±2.8		1
SDSS J0756+4104	5.09	07 56 18.14	+41 04 08.6	13.4±2.1		8
HS B0800+3031	2.02	08 03 42.05	+30 22 54.8	-3.0±3.4	1.8±1.1	1,4
PSS J0808+5215	4.45	08 08 49.4	+52 15 15.0	17.4±2.8	6.6±0.6	2,5
HS 0808+1218	2.26	08 10 57.0	+12 09 14.0	1.1±2.1	1.1±0.9	1,4
KUV 08086+4037	1.78	08 12 00.5	+40 28 14.0		4.3±0.8	4

Table B.1: ... continued

name	z	RA (J2000)	DEC (J2000)	$S_{850\mu m}$ (mJy)	$S_{1.2mm}$ (mJy)	Ref.
HS B0810+2554	1.50	08 13 31.30	+25 45 02.9	7.6±1.8		1
SDSSJ0818+1722	6.00	08 18 27.40	+17 22 51.8		1.45±0.49	9
HS B0821+3613	1.58	08 25 07.66	+36 04 11.5	1.5±2.0		1
HS B0830+1833	2.27	08 32 55.63	+18 23 00.7	-0.5±3.1	1.3±0.9	1,4
SDSSJ0836+0054	5.82	08 36 43.85	+00 54 53.3	1.7±1.5		8
HS B0834+1509	2.51	08 37 12.87	+14 59 17.5	-1.0±2.8	0.6±0.6	1,4
SDSSJ0840+5624	5.85	08 40 35.09	+56 24 19.9		3.20±0.64	9
PSS J0852+5045	4.2	08 52 27.3	+50 45 11.0	1.8±2.2	0.6±0.7	2,5
SBSS 0910+586	1.95	09 14 25.8	+58 25 19.0		0.4±0.6	4
PSS J0926+3055	4.19	09 26 36.3	+30 55 05.0	0.8±1.9	1.0±0.8	2,5
HS B0926+3608	2.14	09 29 52.14	+35 54 49.8	1.2±2.8		1
SDSSJ0927+2001	5.79	09 27 21.82	+20 01 23.7		4.98±0.75	9
HS B0929+3156	2.08	09 32 08.77	+31 43 28.0	5.7±3.0		1
HS B0931+2258	1.74	09 34 42.26	+22 44 39.5	-3.5±2.8		1
HS 0932+2410	2.30	09 35 34.0	+23 57 20.0		1.4±0.6	4
[VV96]J0937+730	2.52	09 37 48.7	+73 01 58.0		3.8±0.9	4
[VV96]J0939+361	2.03	09 39 35.1	+36 40 01.0		1.5±1.0	4
HS B0943+3155	2.79	09 46 23.21	+31 41 30.5	9.6±3.0		1
BRI B0945-0411	4.14	09 47 49.6	-04 25 15.0	2.1±2.2		2
PSS J0950+5801	3.97	09 50 13.9	+58 01 38.0		0.4±0.9	5
PSS J0955+5940	4.34	09 55 11.3	+59 40 30.5		-1.3±1.1	5
PSS J0957+3308	4.25	09 57 44.5	+33 08 20.0	3.7±1.9	0.1±1.2	2,5
[VV96]J0958+470	2.48	09 58 45.5	+47 03 24.0		0.7±0.7	4
HS B1002+4400	2.08	10 05 17.47	+43 46 09.3	8.2±2.9	4.2±0.8	1,4
BRI B1013+0035	4.40	10 15 49.0	+00 20 19.0	5.5±2.7		2
PSS J1026+3828	4.18	10 26 56.7	+38 28 45.0	5.2±2.5	0.4±0.7	2,5
SDSS J1030+0524	6.28	10 30 27.10	+05 24 55.0	1.3±1.0		8
HS B1031+1831	1.53	10 34 28.89	+18 15 32.4	-0.1±2.7		1
SDSS J1044-0125	5.74	10 44 33.04	-01 25 02.2	6.1±1.2		8
J1048+4637	6.23	10 48 45.05	+46 37 18.3		3.0±0.4	7
HS B1049+4033	2.15	10 51 58.71	+40 17 37.0	3.9±3.2	3.2±0.7	1,4
PSS J1058+1245	4.33	10 58 58.4	+12 45 55.0	0.00±2.2	0.1±0.9	2,5

Table B.1: ... continued

name	z	RA (J2000)	DEC (J2000)	$S_{850\mu m}$ (mJy)	$S_{1.2mm}$ (mJy)	Ref.
[VV96]J1106+640	2.19	11 06 10.8	+64 00 08.0		3.9±1.1	4
BRI B1110+0106	3.92	11 12 46.3	+00 49 58.0	7.1±3.4	2.7±0.5	2,3
HS 1110+3813	2.29	11 12 51.0	+37 57 15.0		0.0±1.3	4
HS B1111+4033	2.18	11 13 50.94	+40 17 21.5	2.2±2.8		1
J111401.48-005321.1	4.58	11 14 01.48	-00 53 21.1		0.2±0.3	3
HS B1115+2015	1.93	11 18 00.52	+19 58 53.8	5.3±2.8		1
BR B1117-1329	3.96	11 20 10.2	-13 46 26.2		4.1±0.7	5
J112253.51+005329.8	4.57	11 22 53.51	+00 53 29.8		-0.1±0.3	3
SDSSJ1137+3549	6.01	11 37 17.73	+35 49 56.9		0.10±1.13	9
HS B1140+2711	2.63	11 42 54.27	+26 54 57.8	8.6±2.6		1
HS B1141+4201	2.12	11 43 52.04	+41 45 19.8	8.6±2.6		1
BR B1144-0723	4.15	11 46 35.6	-07 40 05.5		6.0±0.7	5
SDSSJ1148+5251	6.42	11 48 16.64	+52 51 50.3		5.0±0.6	7
KUV 11467+3725	2.22	11 49 20.2	+37 08 29.0		1.0±0.9	4
HS B1155+2640	2.80	11 57 41.91	+26 23 56.2	3.5±2.7		1
PSS J1159+1337	4.07	11 59 06.6	+13 37 37.6		0.9±0.8	5
HS B1200+1539	2.97	12 03 31.28	+15 22 54.4	-5.1±3.1		1
J120441.73-002149.6	5.03	12 04 41.73	-00 21 49.6	4.2±2.0	0.6±0.4	3,8
SDSS J1208+0010	5.27	12 08 23.82	+00 10 27.7	-2±2.5		8
[VV96]J1210+393	2.40	12 10 10.2	+39 39 36.0		0.9±0.8	4
HS B1215+2430	2.36	12 18 10.98	+24 14 10.8	6.0±2.7		1
SDSS J1226+0059	4.25	12 26 00.7	+00 59 24.0	-0.06±3.3	1.4±0.4	2,3
PSS J1226+0950	4.34	12 26 23.8	+09 50 04.7		2.8±0.7	5
PSS J1248+3110	4.35	12 48 20.2	+31 10 44.0	12.7±3.4	6.3±0.8	2,5
[HB89] 1246-057	2.24	12 49 13.8	-05 59 18.0		2.26±0.73	6
SDSSJ1250+3130	6.13	12 50 51.93	+31 30 21.9		0.07±0.90	9
PSS J1253-0228	4.00	12 53 36.4	-02 28 08.3		5.5±0.8	5
[BCF91] 524	2.85	13 04 12.0	+29 53 49.0		0.2±1.0	4
SDSS J1306+0356	5.99	13 06 08.26	+03 56 26.3	3.7±1.0		8
[BBE90]1306+283	2.21	13 09 17.2	+28 14 04.0		-1.6±1.0	4
J131052.52-005533.4	4.14	13 10 52.52	-00 55 33.4		-0.3±0.5	3
HS B1310+4308	2.60	13 12 48.73	+42 52 36.8	10.0±2.8		1

Table B.1: ... continued

name	z	RA (J2000)	DEC (J2000)	$S_{850\mu m}$ (mJy)	$S_{1.2mm}$ (mJy)	Ref.
PSS J1315+2924	4.18	13 15 39.8	+29 24 39.0	4.1±3.3	0.7±0.7	2,5
PSS J1317+3531	4.36	13 17 43.1	+35 31 32.3		3.7±1.1	5
J132110.82+003821.7	4.70	13 21 10.82	+00 38 21.7		0.4±0.4	3
PSS J1326+0743	4.17	13 26 11.8	+07 43 58.0	-0.3±3.9	-0.3±0.6	2,5
HS B1326+3923	2.32	13 28 23.73	+39 08 17.8	7.4±3.0		1
LBQS B1334-0033	2.80	13 36 47.16	-00 48 57.4	2.5±2.6		1
SDSSJ1335+3533	5.95	13 35 50.81	+35 33 15.8		2.34±0.50	9
PSS J1339+5154	4.08	13 39 13.0	+51 54 03.8		1.4±0.6	5
HS B1337+2123	2.70	13 40 10.84	+21 08 44.5	6.8±2.1		1
PSS J1347+4956	4.46	13 47 43.3	+49 56 21.0	8.5±3.9	5.7±0.7	2,5
[HB89] 1346-036	2.37	13 48 44.07	-03 53 24.9		0.80±0.66	6
HS B1356+3113	2.26	13 59 08.39	+30 58 30.8	3.2±3.0		1
PSS J1401+4111	4.01	14 01 32.8	+41 11 50.9		-0.4±1.2	5
[VV96]J1401+543	2.37	14 01 48.4	+54 38 59.0		0.3±0.9	4
UM629	2.46	14 03 23.4	-00 06 07.0		-0.01±0.63	6
PSS J1403+4126	3.85	14 03 55.7	+41 26 16.2		1.5±0.5	5
J140554.07-000037.0	3.55	14 05 54.07	-00 00 37.0		1.0±0.4	3
[VV96]J1409+562	2.56	14 09 55.5	+56 28 27.0		10.7±0.6	4
SDSSJ1411+12 17	5.93	14 11 11.29	+12 17 37.4		1.0±0.62	9
J141315.36+000032.1	4.08	14 13 15.36	+00 00 32.1		2.0±0.8	3
SDSS J1413-0049	4.14	14 13 32.4	-00 49 10.0	-1.0±3.2	2.5±0.5	2,3
PSS J1418+4449	4.28	14 18 31.7	+44 49 38.0	10.4±2.3	6.3±0.7	2,5
SBSS 1417+596	2.31	14 19 06.4	+59 23 12.0		-3.1±1.6	4
HS B1417+4722	2.27	14 19 51.84	+47 09 01.1	8.8±3.4		1
J142329.98+004138.4	3.76	14 23 29.98	+00 41 38.4		0.4±0.8	3
HS B1422+4224	2.21	14 24 35.96	+42 10 30.6	10.7±4.7		1
J142647.82+002740.4	3.69	14 26 47.82	+00 27 40.4		3.9±0.8	3
PSS J1430+2828	4.30	14 30 31.6	+28 28 34.3		3.2±1.2	5
PSS J1432+3940	4.28	14 32 24.8	+39 40 24.0	-1.4±3.3	-1.0±0.7	2,5
PSS J1435+3057	4.35	14 35 23.5	+30 57 22.1		2.4±1.6	5
SDSSJ1436+5007	5.83	14 36 11.74	+50 07 06.9		-0.21±1.14	9
PSS J1443+5856	4.42	14 43 40.7	+58 56 53.3		0.7±0.6	5

Table B.1: ... continued

name	z	RA (J2000)	DEC (J2000)	$S_{850\mu m}$ (mJy)	$S_{1.2mm}$ (mJy)	Ref.
J144428.67-012344.1	4.16	14 44 28.67	-01 23 44.1		-0.4±0.7	3
J144758.46-005055.4	3.80	14 47 58.46	-00 50 55.4		5.4±0.8	3
PSS J1500+5829	4.22	15 00 07.7	+58 29 37.7		0.4±0.9	5
BR B1500+0824	3.94	15 02 45.4	+08 13 06.0	6.2±3.0		2
PSS J1506+5220	4.18	15 06 54.6	+52 20 04.6		3.2 ±1.2	5
J151618.44-000544.3	3.70	15 16 18.44	-00 05 44.3		-0.1±0.6	3
J152740.52-010602.6	4.41	15 27 40.52	-01 06 02.6		-0.1±0.5	3
PSS J1531+4517	4.20	15 31 29.9	+45 17 07.9		0.9±0.7	5
J153259.96-003944.1	4.65	15 32 59.96	-00 39 44.1		0.2±0.7	3
PSS J1535+2943	3.99	15 35 53.9	+29 43 13.0		1.9±0.6	5
PSS J1543+3417	4.41	15 43 40.4	+34 17 44.5		0.3±0.6	5
[VV96]J1543+535	2.37	15 43 59.3	+53 59 03.0		3.8±1.1	4
PSS J1554+1835	3.99	15 54 09.9	+18 35 51.0		6.7±1.1	5
PSS J1555+2003	4.22	15 55 02.6	+20 03 24.4		3.1±0.6	5
SDSSJ1602+4228	6.07	16 02 53.98	+42 28 24.9		1.82±0.86	9
J160501.21-011220.0	4.92	16 05 01.21	-01 12 20.0		0.1±0.4	3
[VV96]J1606+173	2.32	16 06 37.6	+17 35 16.0		1.6±0.7	4
HS 1611+4719	2.35	16 12 39.9	+47 11 58.0		4.6±0.7	4
WF J1612+5255	4.95	16 12 53.10	+52 55 43.5	2.1±1.9		8
PSS J1615+1803	4.01	16 15 22.9	+18 03 56.0		-0.1±0.7	5
HS 1616+3708	2.49	16 18 15.5	+37 01 03.0		1.0±0.6	4
PSS J1618+4125	4.21	16 18 22.7	+41 25 59.7		1.2±1.1	5
J161926.87-011825.2	3.84	16 19 26.87	-01 18 25.2		2.3±0.6	3
J162116.91-004251.1	3.70	16 21 16.91	-00 42 51.1		0.1±0.3	3
SDSSJ1623+3112	6.22	16 23 31.81	+31 12 00.5		0.17±0.80	9
J1630+4012	6.05	16 30 33.9	+40 12 09.6		0.8±0.6	7
PSS J1633+1411	4.35	16 33 19.6	+14 11 42.3		1.1±1.2	5
PSS J1646+5514	4.04	16 46 56.5	+55 14 46.0	9.5±2.5	4.6±1.5	2,5
J165527.61-000619.2	3.99	16 55 27.61	-00 06 19.2		-0.1±0.4	3
SDSS1701+623	2.30	17 01 02.18	+61 23 01.0		-0.38±0.9	6
HS B1703+5350	2.37	17 04 06.74	+53 46 53.6	-0.1±2.6		1
HS 1707+4602	2.29	17 09 04.9	+45 59 08.0		2.1±1.5	4

Table B.1: ... continued

name	z	RA (J2000)	DEC (J2000)	$S_{850\mu m}$ (mJy)	$S_{1.2mm}$ (mJy)	Ref.
PSS J1721+3256	4.03	17 21 06.7	+32 56 35.9		-0.8±0.8	5
[VV96]J1838+510	1.98	18 37 25.3	+51 05 59.0		-1.0±0.8	4
SDSS J2216+0013	4.99	22 16 44.02	+00 13 48.3	1.7±1.4		8
WF J2245+0024	5.17	22 45 24.28	+00 24 14.6	2.3±1.6		8
LBQS B2244-0105	2.03	22 46 49.30	-00 49 53.9	0.2±2.8		1
J225419.23-000155.0	3.68	22 54 19.23	-00 01 55.0		0.3±0.4	3
J225759.67+001645.7	3.75	22 57 59.67	+00 16 45.7		0.4±0.4	3
J230952.29-003138.9	3.95	23 09 52.29	-00 31 38.9		-0.2±0.5	3
PSS J2322+1944	4.17	23 22 07.2	+19 44 23.0	22.5±2.5	9.6±0.5	2,4
J235718.35+004350.4	4.34	23 57 18.35	+00 43 50.4		1.8±0.6	3

References: 1 Priddey et al. (2003a), 2 Isaak et al. (2002), 3 Carilli et al. (2001b), 4 Omont et al. (2003), 5 Omont et al. (2001), 6 Our observations, 7 Bertoldi et al. (2003a), 8 Priddey et al. (2003b), and 9 Wang et al. (2007).

Table B.2: Derived properties of the quasars observed at submm/mm wavelength

name	L_{FIR} $10^{12}L_{\odot}$	log λL_{λ}(1500Å) (erg s^{-1})	log M_{BH} [$M_{\odot}$]	$L/L_{\rm Edd}$ [erg/s]	log $L_{[OIII]}$	$\frac{NV}{CIV}$	Ref.
SDSSJ0002+2550	0.52±2.31	47.60					
LBQS B0009-0138	4.20±5.34	46.96	8.85				2
LBQS B0013-0029	5.61±5.78	46.65	9.07	0.79			2
LBQS B0025-0151	8.41±4.33	46.64					
J003525.29+004002.8	0.88±1.46	46.37					
HS B0035+4405	15.33±4.57	46.88					
SDSS0058+0115	4.85±3.55	46.95	10.07	0.16	44.57		4
LBQS0109+0213	3.11±3.72	47.22	10.00	0.35	44.50	0.82	5
J012403.78+004432.7	6.98±1.05	47.06	10.12	0.18		1.11	1
J012650.77+011611.8	0.00±2.08	46.69					
PSS J0134+3307	10.89±4.67						
J015048.83+004126.2	7.67±1.39	46.81	9.28	0.70		2.51	1
J021102.72-000910.3	1.45±0.87	46.34	8.98	0.47			3
SDSS J0231-0728	2.39±2.13	46.68					
J023231.40-000010.7	6.28±1.05	46.30					
J025112.44-005208.2	8.22±2.05	46.46					
J025518.58+004847.6	7.39±1.41	46.81	9.60	0.34		1.47	1
RD J0301+0020	2.45±1.93	46.54	7.78				7
BR B0300-0207	0.00±3.85	47.31					
Q0302-0019	1.79±2.07	47.23	10.06	0.31	44.99		
J031036.97-001457.0	0.00±1.20	46.27					
J032608.12-003340.2	4.94±1.32	46.57	9.58	0.20		1.26	1
J033829.31+002156.3	10.33±0.84	46.43	9.32				7
BR B0351-1034	0.00±4.03						
PSS J0747+4434	0.32±3.88	46.50	9.48	0.22		0.72	1
HS 0749+4259	6.53±4.52	47.41					
HS B0752+3429	4.36±5.08	46.85					
SDSS J0756+4104	17.89±2.80	47.26	9.32				7
HS B0800+3031	8.66±5.29	47.34	9.96	0.50			1
PSS J0808+5215	21.45±1.95	47.02					
HS 0808+1218	5.23±4.28	46.98					
KUV 08086+4037	22.30±4.15	46.75					
HS B0810+2554	13.72±3.25	47.26	9.44	1.37			1
SDSSJ0818+1722	3.80±1.28	46.99					
HS B0821+3613	2.80±3.74	46.84	9.26	0.79			1
HS B0830+1833	6.25±4.33	47.06					
SDSSJ0836+0054	2.18±1.92	47.25	9.97	0.44		1.44	8

Table B.2: ... continued

name	L_{FIR} $10^{12}L_\odot$	log $\lambda L_\lambda(1500Å)$ (erg s^{-1})	log M_{BH} [$M_\odot$]	$L/L_{\rm Edd}$ [erg/s]	log $L_{[OIII]}$	$\frac{NV}{CIV}$	Ref.
HS B0834+1509	2.77±2.77	46.88					
SDSSJ0840+5624	8.56±1.71	46.80					
PSS J0852+5045	2.02±2.36	46.85	9.58	0.39		1.48	1
SBSS 0910+586	1.94±2.91	46.80					
PSS J0926+3055	3.35±2.68	47.47					
HS B0926+3608	2.25±5.26	47.23					
SDSSJ0927+2001	13.0±1.96	46.80					
HS B0929+3156	9.99±5.26	46.95					
HS B0931+2258	0.00±5.02	47.07					
HS 0932+2410	6.32±2.71	46.79					
[VV96]J0937+730	17.71±4.19	47.25					
[VV96]J0939+361	7.30±4.87	46.71	9.18	0.71			1
HS B0943+3155	15.39±4.81	47.08					
BRI B0945-0411	2.93±3.07						
PSS J0950+5801	1.41±3.17	47.21	9.69	0.69		1.33	1
PSS J0955+5940	0.00±3.37	46.99	9.68	0.43		1.75	1
PSS J0957+3308	0.32±3.81	47.08					
[VV96]J0958+470	3.14±3.14	46.90					
HS B1002+4400	19.73±3.76	47.23	10.08	0.29			1
BRI B1013+0035	7.59±3.72	46.63	9.58	0.23		1.74	1
PSS J1026+3828	1.33±2.33	46.75	10.09	0.09		1.22	1
SDSS J1030+0524	1.62±1.25	46.74	9.56	0.50		0.21	8
HS B1031+1831	0.00±5.12	47.11					
SDSS J1044-0125	7.58±1.49	46.89	10.02	0.31		0.23	8
J1048+4637	7.33±0.98	46.92	9.78				10
HS B1049+4033	14.81±3.24						
PSS J1058+1245	0.33±2.99	46.92					
[VV96]J1106+640	18.88±5.33	47.56					
BRI B1110+0106	9.22±1.71	46.81	9.95	0.15		1.85	1
HS B1111+4033	3.95±5.02	47.03	9.94	0.25			1
J111401.48-005321.1	0.64±0.96	46.53	9.57	0.19		0.97	1
HS B1115+2015	10.17±5.37	47.18					
BR B1117-1329	14.35±2.45						
J112253.51+005329.8	0.00±0.95	46.73	9.27	0.60		2.39	1
SDSSJ1137+3549	0.26±2.97	47.04					
HS B1140+2711	14.24±4.31	47.37					
HS B1141+4201	15.79±4.77	47.02					

Table B.2: ... continued

name	L_{FIR} $10^{12}L_{\odot}$	log λL_{λ}(1500Å) (erg s^{-1})	log M_{BH} [$M_{\odot}$]	$L/L_{\rm Edd}$ [erg/s]	log $L_{[OIII]}$	$\frac{NV}{CIV}$	Ref.
BR B1144-0723	19.67±2.29						
J1148+5251	12.10±1.45	47.00	9.30	1.04			6
KUV 11467+3725	4.55±4.09	46.91					
HS B1155+2640	5.66±4.36	47.02	9.88	0.29		1.20	1
PSS J1159+1337	3.07±2.73	47.25					
HS B1200+1539	0.00±4.86	47.39	9.88	0.67		1.24	1
J120441.73-002149.6	1.70±1.13	46.69	9.32	1.0			11
SDSS J1208+0010	0.00±3.12	47.00					
[VV96]J1210+393	4.10±3.64	47.03					
HS B1215+2430	10.89±4.90	47.16					
SDSS J1226+0059	4.45±1.27	46.76	9.96	0.13		1.33	1
PSS J1226+0950	8.58±2.14	46.64	10.08	0.08		0.88	1
PSS J1248+3110	19.40±2.46	46.62					
[HB89] 1246-057	10.52±3.40	47.46	10.22	0.36	44.14	1.82	4
SDSSJ1250+3130	0.178±2.29	47.60					
PSS J1253-0228	18.04±2.62	46.69					
[BCF91] 524	0.86±4.32	47.06					
SDSS J1306+0356	4.74±1.28	46.74	9.50	0.61		0.55	8
[BBE90]1306+283	0.00±4.95	46.34					
J131052.52-005533.4	0.00±1.63	46.75	9.65	0.26		1.44	1
HS B1310+4308	17.60±4.93	47.07					
PSS J1315+2924	2.33±2.33	46.57					
PSS J1317+3531	11.46±3.41	46.61					
J132110.82+003821.7	1.24±1.24	47.27	9.38	1.62		0.80	1
HS B1326+3923	12.89±5.22	47.23					
LBQS B1334-0033	4.04±4.20	47.10	9.79	0.42		1.20	1
SDSSJ1335+3533	6.01±1.28	46.81					
PSS J1339+5154	4.81±2.06	46.66					
HS B1337+2123	10.99±3.39	46.88					
PSS J1347+4956	17.09±2.10	46.50					
[HB89] 1346-036	3.53±2.91	47.18	9.94	0.36	43.72	0.78	4
HS B1356+3113	5.72±5.37	46.98					
PSS J1401+4111	0.00±3.96	46.75	9.66	0.26		2.15	1
[VV96]J1401+543	1.32±3.97	45.68					
UM629	0.00±2.77	46.80	9.16	0.91	44.40	0.80	5
PSS J1403+4126	5.36±1.79	46.55	9.75	0.13		0.77	1
J140554.07-000037.0	3.52±1.41	46.74					

Table B.2: ... continued

name	L_{FIR} $10^{12}L_{\odot}$	log $\lambda L_{\lambda}(1500\text{Å})$ (erg s^{-1})	log M_{BH} [$M_{\odot}$]	L/L_{Edd} [erg/s]	log $L_{[OIII]}$	$\frac{NV}{CIV}$	Ref.
[VV96]J1409+562	47.19±2.65	47.17	10.17	0.21	43.86		4
SDSSJ1411+1217	2.55±1.58	46.82	9.11	0.94		0.56	8
J141315.36+000032.1	6.87±2.75	46.39					
SDSS J1413-0049	8.15±1.63	46.57	9.53	0.23		1.38	1
PSS J1418+4449	20.35±2.26	46.93					
SBSS 1417+596	0.00±7.30	46.87	9.68	0.33		2.67	1
HS B1417+4722	15.92±6.15	46.87					
J142329.98+004138.4	1.35±2.70	46.41	9.50	0.17		1.23	1
HS B1422+4224	19.85±8.72	46.01	9.60	0.05		1.19	1
J142647.82+002740.4	13.78±2.82	46.46					
PSS J1430+2828	10.45±3.92	46.55					
PSS J1432+3940	0.00±2.26	46.54	9.87	0.10		1.60	1
PSS J1435+3057	7.39±4.93	46.89					
SDSSJ1436+5007	0.00±3.02	46.79					
PSS J1443+5856	0.00±1.60	47.20	10.12	0.25		1.96	1
J144428.67-012344.1	0.00±2.31	46.53	9.71	0.14		1.44	1
J144758.46-005055.4	18.72±2.77	46.46					
PSS J1500+5829	1.25±2.81	46.79					
BR B1500+0824	9.03±4.37	46.72					
PSS J1506+5220	10.67±4.00	46.98					
J151618.44-000544.3	0.00±2.13	46.19	9.31	0.16		2.78	1
J152740.52-010602.6	0.00±1.59	46.30	9.51	0.13		2.55	1
PSS J1531+4517	3.03±2.36	46.34	9.58	0.12		1.48	1
J153259.96-003944.1	0.61±2.12	46.42					
PSS J1535+2943	6.19±1.96	46.44					
PSS J1543+3417	0.95±1.91	47.01	9.20	1.34		2.27	1
[VV96]J1543+535	16.78±4.86	47.13	9.71	0.55		1.24	1
PSS J1554+1835	21.84±3.59	46.52					
PSS J1555+2003	9.68±1.87	46.60					
SDSSJ1602+4228	4.53±2.14	47.02					
J160501.21-011220.0	0.29±1.17	46.35					
[VV96]J1606+173	7.37±3.23	46.65					
HS 1611+4719	21.88±3.33	47.03					
WF J1612+5255	2.83±2.56	46.09					
PSS J1615+1803	0.00±2.31						
HS 1616+3708	4.53±2.72	46.90					
PSS J1618+4125	4.07±3.73	46.51	9.14	0.49		1.09	1

Table B.2: ... continued

name	L_{FIR} $10^{12}L_{\odot}$	log λL_{λ}(1500Å) (erg s^{-1})	log M_{BH} [$M_{\odot}$]	$L/L_{\rm Edd}$ [erg/s]	log $L_{[OIII]}$	$\frac{NV}{CIV}$	Ref.
J161926.87-011825.2	8.17±2.13	47.75					
J162116.91-004251.1	0.35±1.07	47.30					
SDSSJ1623+3112	0.41±1.95	46.74	9.53	0.50			9
J1630+4012	1.97±1.48	47.51	9.20				10
PSS J1633+1411	3.39±3.69	46.91					
PSS J1646+5514	15.45±5.04	47.47					
J165527.61-000619.2	0.00±1.30	47.26					
SDSS1701+623	0.00±4.06	46.70	9.72	0.20	43.50	1.19	5
HS B1703+5350	0.00±4.36	47.10					
HS 1707+4602	9.38±6.70	46.97					
PSS J1721+3256	0.00±2.67	48.06					
[VV96]J1838+510	0.00±4.03	46.27					
SDSS J2216+0013	2.17±1.78	46.29	9.28				7
WF J2245+0024	2.96±2.06	46.50					
LBQS B2244-0105	0.36±5.06	46.80	9.13	0.97			1
J225419.23-000155.0	1.05±1.40	46.44					
J225759.67+001645.7	1.47±1.47	46.70					
J230952.29-003138.9	0.00±1.74	46.50					
PSS J2322+1944	31.83±1.66	47.41					
J235718.35+004350.4	5.51±1.84	46.44	10.08	0.05		0.88	1

References: 1 SDSS spectra, 2 Brotherton et al. (1994), 3 Iwamuro et al. (2002), 4 Our data, 5 Shemmer et al. (2004), 6 Barth et al. (2003), 7 Priddey et al. (2003b), 8 Jiang et al. (2007), 9 Jiang et al. (2006), 10 Robson et al. (2004), and 11 Dietrich & Hamann (2004).

Table B.3: Derived properties of the quasars observed at IR wavelength

Name	z	L_{FIR} 10^9 $L_\odot$	log $\lambda L_\lambda(1500\text{Å})$ (erg s^{-1})	log $M_{\rm BH}$ ($M_\odot$)	$L/L_{\rm Edd}$	log $L_{\rm [OIII]}$ (erg s^{-1})	Ref.
PG0007+106	0.089	275	44.36	8.19	0.16	42.26	1, 3
PG0804+761	0.100	38	44.76	8.09	0.34	42.04	1, 3
PG1149-110	0.049	25	44.00	7.52	0.19	41.47	1, 3
PG1211+143	0.084	67	44.91	7.69	0.68	41.94	1, 3
PG1229+204	0.063	37	44.37	7.91	0.22	41.58	1, 3
PG1244+026	0.048	29	43.55	6.16	0.44	40.77	1, 3
PG1351+640	0.088	139	45.15	8.78	0.29	42.54	1, 3
PG1404+226	0.098	39	44.35	6.72	0.84	41.29	1, 3
PG1415+451	0.114	132	44.34	7.62	0.30	40.83	1, 3
PG1426+015	0.086	206	44.63	8.62	0.15	41.74	1, 3
PG1440+356	0.079	249	44.44	7.32	0.49	41.46	1, 3
PG1501+106	0.036	30	43.94	7.99	0.10	41.72	1, 3
PG2130+099	0.062	114	44.51	7.84	0.30	41.83	1, 3
PG0050+124	0.061	382	44.70	7.09	0.97	41.88	2, 3
PG1411+442	0.090	37	44.68	7.84	0.39	41.82	2, 3

1 Haas et al. (2003), 2 Haas et al. (2000), and 3 Marziani et al. (2003)

APPENDIX C

AGNS IRS SPECTRA

In this section we displayed the IRS spectra for objects with available X-ray data in order of the HI column density. The black line is the observed spectrum. The blue line shows the starburst component, which is formally requiered by the fit. The red line is the power-law component of the fit, and the green line indicates the residuum by subtracting the starburst component. In all the plots the y-axis corresponds to the flux in units of Jy and the x-axis corresponds to the rest-frame wavelength in μm. In addition, derived properties of the AGNs are shown in Table C.1.

Table C.1: MIR and hard X-ray data for AGNs IRS spectra

Name	z	RA (J2000)	DEC (J2000)	Si strength	$\log \lambda L_\lambda(6.7\mu m)$ erg/s	$\log L(PAH_{7.7\mu m})$ erg/s	N_H^a	$F_{2-10keV}^b$	$L_{2-10keV}^c$	Type[d]	Ref. (X-ray data)
Mrk335	0.0258	00 06 19.5	+20 12 10	0.079±0.027	43.94		0.009	94.4	43.16	Sy 1	George et al. (2000)
2MASX J0007	0.114	00 07 03.6	+15 54 24	0.137±0.049	44.28	42.77	2.45	7.75	43.48	RQQ	Wilkes et al. (2002)
IIIZW2	0.090	00 10 30.8	+10 58 13	0.078±0.018	44.57	42.07	0.05	72.0	44.17	Sy 1	Piconcelli et al. (2005)
Mrk0938	0.0198	00 11 06.5	-12 06 26			43.14	40.00	3.30	42.06	Sy 2	Guainazzi et al. (2005)
IRAS 00182-7112	0.327	00 20 34.7	-70 55 27	-3.831±0.287	45.77	44.38	>1000.0	1.58		RQQ	Ruiz et al. (2007)
ESO12-G21	0.030	00 40 46.1	-79 14 24	0.389±0.034	43.62	42.63	0.005	58.0	43.08	Sy 2	Ghosh (1992)
Mrk348	0.0150	00 48 47.1	+31 57 25	-0.268±0.021	43.40	41.24	16.00	38.11	42.61	Sy 1	Risaliti (2002)
2MASX J0050	0.136	00 50 55.7	+29 33 28	-0.207±0.061	44.47	42.87	1.23	6.15	43.51	RQQ	Wilkes et al. (2002)
PG0050+124	0.061	00 53 34.9	+12 41 36	0.307±0.028	44.93	42.62	0.09	84.4	43.70	RQQ	Piconcelli et al. (2005)
PG0052+251	0.155	00 54 52.1	+25 25 38	0.303±0.031	44.77	42.63	0.04	67.7	44.65	RQQ	D'Ammando et al. (2008)
2MASSi J0108	0.285	01 08 35.1	+21 48 18	-0.033±0.024	45.35	42.85	1.47	0.68	43.27	RQQ	Wilkes et al. (2002)
NGC424	0.0118	01 11 27.6	-38 05 00	0.093±0.028	43.82	41.70	200.00	16.0	43.42	Sy 2	Matt et al. (2003)
FAIRALL9	0.046	01 23 45.8	-58 48 20	0.194±0.011	44.47	42.02	0.03	156.0	43.89	Sy 1	Gondoin et al. (2001)
NGC526a	0.019	01 23 54.4	-35 03 56	0.197±0.028	43.52	40.74	1.33	172.0	43.20	Sy 1	Risaliti (2002)
3C48	0.367	01 37 41.3	+33 09 35	0.140±0.033	45.73	43.97	0.43	22.0	45.02	RLQ	Siemiginowska et al. (2003)
IRAS F01475-0740	0.0176	01 50 02.7	-07 25 48	0.367±0.031	43.12	41.85	0.389	8.20	41.77	Sy 2	Guainazzi et al. (2005)
2MASSi J0157	0.213	01 57 21.0	+17 12 48	-0.319±0.166	44.81	43.39	0.70	6.36	43.94	RQQ	Wilkes et al. (2002)
2MASX J0221	0.140	02 21 50.5	+13 27 40	-0.213±0.074	44.65	41.81	0.70	3.201	43.26	RQQ	Wilkes et al. (2002)
NGC931	0.0166	02 28 14.5	+31 18 42	-0.056±0.035	43.76	41.28	0.53	51.0	42.52	Sy 1	Reynolds et al. (1995)
2MASX J0234	0.310	02 34 30.6	+24 38 35	0.301±0.036	45.19	43.30	0.86	0.387	43.10	RQQ	Wilkes et al. (2002)
Mkn1066	0.012	02 59 58.6	+36 49 14	-0.308±0.121	42.99	42.39	90.00	3.60	42.07	Sy 2	Guainazzi et al. (2005)
IRAS F03158+4227	0.134	03 19 12.4	+42 38 28		44.65	43.65	100.00	5.40		Sy 2	Risaliti et al. (2000)
NGC1365	0.0054	03 33 36.4	-36 08 25	0.086±0.131	42.96	41.82	35.00 12.00	90.7	42.11	Sy 1	Risaliti et al. (2005)
NGC1386	0.003	03 36 46.2	-35 59 57	-0.594±0.063	42.18	40.67	>100.00	2.70		Sy 2	Guainazzi et al. (2005)
IRAS 04103-2838	0.11746	04 12 19.4	-28 30 35	-0.347±0.014	44.40	43.66	100.00	0.38		LINER	Teng et al. (2008)
ESO33-G2	0.0181	04 55 58.9	-75 32 28	-0.004±0.029	43.51	41.59	1.40	120.0	42.99	Sy 2	Vignali et al. (1998)
PictorA	0.034	05 19 49.7	-45 46 44	0.533±0.020	43.51	40.79	0.0825	134.0	43.56	FRII	Sambruna et al. (1999)
IRAS F05189-2524	0.0426	05 21 01.5	-25 21 45	-0.342±0.085	44.70	43.18	4.70	53.0	43.49	Sy 2	Risaliti et al. (2000)
NGC2110	0.008	05 52 11.4	-07 27 22	0.427±0.035	42.80	40.95	2.65	259.3	42.66	Sy 2	Risaliti (2002)
NGC2273	0.006	06 50 08.6	+60 50 45	-0.101±0.054	42.59	41.69	1000.00	6.90	42.12	Sy 2	Guainazzi et al. (2005)
Mrk6	0.0188	06 52 12.2	+74 25 37	-0.262±0.036	43.63	41.74	11.00	109.1	43.20	Sy 1	Immler et al. (2003)
IR07145-2914	0.006	07 16 31.2	-29 19 29	-0.385±0.056	42.50	41.26	>1000.0	3.80		Sy 2	Levenson et al. (2006)
Mrk79	0.022	07 42 32.8	+49 48 35	0.118±0.039	43.82	42.09	<0.0168	271.0	43.48	Sy 1	Gallo et al. (2006)
IRAS 07598+6508	0.1483	08 04 33.1	+64 59 49	0.082±0.009	45.62	43.09	160.00	0.458	43.64	BALQ	Watson et al. (2009)
PG0804+761	0.100	08 10 58.6	+76 01 51	0.452±0.016	45.01		<0.028	111.0	44.45	RQQ	Piconcelli et al. (2005)
AXJ0843+2932	0.398	08 43 09.9	+29 44 04	0.387±0.092	44.82	42.97	15.80	14.2	45.09	RQQ	Della Ceca et al. (2003)
IRAS 09104+4109	0.442	09 13 45.4	+40 56 28	-0.308±0.013	46.24	43.32	48.00	4.68	44.93	RQQ	Piconcelli et al. (2007)
HydraA	0.054	09 18 05.7	-12 05 44		42.45	41.86	2.09	1.80	42.16	FRII	Sambruna et al. (2000)
Mrk704	0.029	09 18 26.0	+16 18 19	0.078±0.016	44.20	42.02	0.130	138.0	43.43	Sy 1	Landi et al. (2007)
2MASSiJ0918	0.149	09 18 48.6	+21 17 17	-0.223±0.043	44.80	42.72	0.110	1.90	43.06	RQQ	Wilkes et al. (2002)
3C220	0.610	09 32 39.6	+79 06 32	0.049±0.262	44.72		0.70	2.70	44.92	FRII	Belsole et al. (2006)
PG0946+301	1.216	09 49 41.1	+29 55 19	0.147±0.057	46.52	44.75	>100.00	7.20		BALQ	Mathur et al. (2000)
2MASSiJ0955	0.139	09 55 04.5	+17 05 56	0.233±0.067	44.26	42.19	2.06	3.96	43.36	RQQ	Wilkes et al. (2002)
PG0953+414	0.234	09 56 52.4	+41 15 22	0.435±0.048	45.15	42.95	0.006	32.1	44.72	RQQ	Piconcelli et al. (2005)
NGC3081	0.008	09 59 29.5	-22 49 35	-0.176±0.015	42.59	40.83	66.00	13.0	42.05	Sy 2	Bassani et al. (1999)

Table C.1: ... continued

Name	z	RA (J2000)	DEC (J2000)	Si strength	$\log \lambda L_\lambda(6.7\mu m)$ erg/s	$\log \mathrm{L(PAH}_{7.7\mu\mathrm{m}})$ erg/s	$N_{\mathrm{H}}^{\mathrm{a}}$	$F_{2-10\mathrm{keV}}^{\mathrm{b}}$	$L_{2-10\mathrm{keV}}^{\mathrm{c}}$	Type[d]	Ref. (X-ray data)
3C234	0.185	10 01 49.5	+28 47 09	-0.008±0.004	45.40	42.54	24.00	13.0	44.43	Sy 2	Piconcelli et al. (2008)
NGC3079	0.0037	10 01 57.8	+55 40 47			41.93	1000.00	14.69	42.07	Sy 2	Della Ceca et al. (2008)
2MASSiJ1027	0.231	10 27 24.9	+12 19 20	-0.248±0.047	45.15	42.15	1.46	2.351	43.60	RQQ	Wilkes et al. (2002)
NGC3281	0.011	10 31 52.1	-34 51 13	-1.169±0.059	43.57	41.76	200.00	29.0	43.36	Sy 2	Vignali & Comastri (2002)
SJ10447 (A2)	0.555	10 44 07.9	+58 44 37	-0.468±0.120	44.77	43.51	5.00	0.093	43.12	RQQ	Polletta et al. (2006)
SJ10449 (A4)	2.540	10 44 09.9	+58 52 24	-0.181±0.282	46.41	44.86	200.00	0.031	44.24	RQQ	Lanzuisi et al. (2009)
SJ10445 (A5)	1.89	10 44 53.0	+58 54 53	-0.600±0.231	45.42	44.38	19.00	0.210	44.78	RQQ	Polletta et al. (2006)
SJ10452 (A8)	2.31	10 45 28.3	+59 13 26	-0.786±0.144	46.00	44.90	86.00	0.044	44.42	RRQ	Polletta et al. (2006)
SJ10461 (A6)	2.10	10 46 13.4	+58 59 41	-0.429±0.338	45.68		15.00	0.249	44.95	RQQ	Polletta et al. (2006)
NGC3393	0.013	10 48 23.4	-25 09 43	-0.329±0.021	42.60	41.21	>1000.0	0.730		Sy 2	Levenson et al. (2006)
2MASX J1051	0.158	10 51 44.2	+35 39 30	-0.327±0.092	44.32		0.720	20.0	44.15	RQQ	Wilkes et al. (2005)
LH12A	0.990	10 51 48.8	+57 32 48	0.253±0.113	44.80	43.17	5.01	0.329	44.26	RQQ	Mainieri et al. (2002)
LH14z	1.380	10 52 42.2	+57 31 58	0.372±0.257	44.33		3.98	0.128	44.19	RQQ	Mainieri et al. (2002)
LHH57	0.792	10 53 05.7	+57 28 10	0.881±0.193	44.12		2.51	0.088	43.44	RQQ	Mainieri et al. (2002)
3C249.1	0.312	11 04 13.7	+76 58 58	0.581±0.033	45.28	43.19	1.06	38.30	45.10	RLQ	Piconcelli et al. (2005)
NGC3516	0.0088	11 06 47.5	+72 34 07	0.0002±0.028	43.04	41.02	1.00	134.9	42.40	Sy 1	Panessa et al. (2006)
PG1116+215	0.176	11 19 08.6	+21 19 18	0.587±0.086	44.50	42.91	0.019	33.00	44.46	RQQ	Piconcelli et al. (2005)
NGC3982	0.0037	11 56 28.1	+55 07 31	-0.314±0.272	41.09		160.00	0.500	40.68	Sy 2	Guainazzi et al. (2005)
NGC3783	0.010	11 39 01.7	-37 44 19	-0.171±0.045	43.51	40.74	0.021	551.0	43.09	Sy 1	Kaspi et al. (2001)
3C265	0.811	11 45 29.0	+31 33 49	0.181±0.064	45.73	42.95	16.80	1.80	44.84	FRII	Belsole et al. (2006)
NGC3998	0.003	11 57 56.1	+55 27 13	0.373±0.017	41.46	38.99	0.024	120.0	41.38	LINER	Pellegrini et al. (2000)
NGC4051	0.0023	12 03 09.6	+44 31 53	0.165±0.034	42.00	40.49	0.001	149.8	41.24	Sy 1	Pounds et al. (2004)
NGC4151	0.003	12 10 32.6	+39 24 21	-0.103±0.073	42.87	40.70	7.50	451.0	42.14	Sy 1	Cappi et al. (2006)
NGC4388	0.008	12 25 46.7	+12 39 44	-0.823±0.072	43.04	41.70	35.00	55.80	42.44	Sy 2	Iwasawa et al. (2003)
3C273	0.158	12 29 06.7	+02 03 09	0.036±0.010	45.83	42.19	0.030	787.0	45.73	RLQ	Piconcelli et al. (2005)
NGC4507	0.012	12 35 36.6	-39 54 33	-0.137±0.027	43.60	41.71	29.20	128.0	43.10	Sy 2	Matt et al. (2004)
NGC4593	0.009	12 39 39.4	-05 20 39	0.101±0.017	43.14	41.04	0.010	377.9	42.83	Sy 1	Perola et al. (2002)
TOL1238-364	0.0109	12 40 52.8	-36 45 21	-0.208±0.041	43.03	41.87	>160.00	0.80	42.42	Sy 2	Guainazzi et al. (2005)
IRAS 12514+1027	0.30	12 54 00.8	+10 11 12	-1.480±0.029	45.67	43.96	0.130	0.063	42.47	Sy 2	Ruiz et al. (2007)
Mkn231	0.042	12 56 14.2	+56 52 25	-0.654±0.149	45.22	43.51	140.00	7.00	43.69	BALQ	Braito et al. (2004)
3C280	0.996	12 56 57.1	+47 20 20	-0.129±0.064	45.67	42.59	9.70	0.30	44.24	FRII	Belsole et al. (2006)
2MASX J1300	0.080	13 00 05.3	+16 32 15	-0.136±0.027	44.67		2.90	23.5	43.65	RQQ	Wilkes et al. (2005)
NGC4941	0.003	13 04 13.1	-05 33 06	-0.302±0.038	41.33	39.12	45.00	7.00	40.76	Sy 2	Bassani et al. (1999)
NGC4939	0.010	13 04 14.4	-10 20 23	0.075±0.044	42.04	40.23	15.00	33.00	42.15	Sy 2	Guainazzi et al. (2005)
NGC5005	0.003	13 10 56.2	+37 03 33	-0.164±0.044	41.79	40.95	5.00	5.10	40.16	Sy 2	Guainazzi et al. (2005)
PG1309+355	0.184	13 12 17.8	+35 15 21	0.492±0.051	45.02		0.0340	7.30	44.84	RQQ	Piconcelli et al. (2005)
NGC5135	0.014	13 25 44.0	-29 50 01	0.137±0.122	43.20	42.69	>100.00	1.60		Sy 2	Guainazzi et al. (2005)
M-6-30-15	0.006	13 35 53.8	-34 17 44	-0.104±0.035	42.80	40.63	0.410	230.0	42.28	Sy 1	Wilms et al. (2001)
NGC5256	0.0278	13 38 17.5	+48 16 37			43.02	>1000.0	5.60		SY 2	Risaliti et al. (2000)
IRAS 13451+1232	0.122	13 47 33.3	+12 17 24	-0.327±0.012	44.74	42.79	1.50	10.00	43.62	Sy 2	Risaliti et al. (2000)
IC4329A	0.016	13 49 19.2	-30 18 34	-0.044±0.026	44.08	41.84	0.260	370.0	43.34	Sy 1	Bianchi et al. (2004)
PG1351+640	0.088	13 53 15.8	+63 45 45	0.962±0.032	44.61	42.42	0.0260	15.50	43.48	RQQ	Watson et al. (2009)
NGC5347	0.008	13 53 17.8	+33 29 27	-0.129±0.020	42.74	41.08	>100.00	2.20		Sy 2	Levenson et al. (2006)
Mrk463E	0.050	13 56 02.9	+18 22 19	-0.475±0.011	44.90	42.61	71.00	4.10	43.29	Sy 2	Bianchi et al. (2008)
2MASX J1402	0.187	14 02 51.2	+26 31 17	0.013±0.086	44.73		0.040	19.0	44.28	RQQ	Wilkes et al. (2005)
Circinus	0.001	14 13 09.9	-65 20 21	-1.134±0.769	42.64	41.15	430.00	140.0	41.89	Sy 2	Matt et al. (1999)

Table C.1: ... continued

Name	z	RA (J2000)	DEC (J2000)	Si strength	$\log \lambda L_\lambda(6.7\mu m)$ erg/s	$\log$ L(PAH$_{7.7\mu m}$) erg/s	N_H^a	$F_{2-10keV}^b$	$L_{2-10keV}^c$	Type[d]	Ref. (X-ray data)
NGC5506	0.006	14 13 14.8	-03 12 27	-0.768±0.092	43.34	41.76	3.40	580.0	42.78	Sy 2	Bianchi et al. (2003)
NGC5548	0.017	14 17 59.5	+25 08 12	0.175±0.015	43.35	41.62	0.042	359.3	43.37	Sy 1	Perola et al. (2002)
NGC5643	0.004	14 32 40.8	-44 10 29	-0.306±0.044	42.07	41.14	70.00	8.40	41.23	Sy 2	Guainazzi et al. (2004)
NGC5674	0.025	14 33 52.2	+05 27 30	-0.029±0.028	42.98	41.84	7.0	84.0	43.26	Sy 2	Bassani et al. (1999)
2MASX J1501	0.258	15 01 13.2	+23 29 08	-0.095±0.043	45.02	43.13	0.580	1.86	43.59	RQQ	Wilkes et al. (2002)
2MASSi J1516	0.190	15 16 53.2	+19 00 48	0.208±0.026	45.53		1.23	3.765	43.62	RQQ	Wilkes et al. (2002)
NGC5929	0.083	15 26 06.1	+41 40 14	-0.679±0.325	44.27		4.25	13.50	43.48	Sy 2	Shu et al. (2007)
IRAS F15307+3252	0.926	15 32 44.0	+32 42 47	-0.198±0.034	46.11	44.50	>100.00	0.350	44.39	Sy 2	Iwasawa et al. (2005)
IRAS F15480-0344	0.0303	15 50 41.5	-03 53 18	0.224±0.036	43.63	42.01	>160.00	3.70	43.37	Sy 2	Guainazzi et al. (2005)
3C330	0.550	16 09 36.6	+65 56 44	-0.159±0.047	44.97	43.42	23.6	0.70	44.16	FRII	Belsole et al. (2006)
2MASSi J1637	0.211	16 37 00.2	+22 21 14	-0.125±0.095	44.61	43.39	0.70	4.714	43.80	RRQ	Wilkes et al. (2002)
NGC6240	0.02448	16 52 58.9	+02 24 03	-1.942±0.124	43.71	43.20	218.00	16.9	43.77	LINER	Bassani et al. (1999)
2MASSi J1659	0.170	16 59 39.7	+18 34 36	-0.025±0.024	45.00	43.02	2.93	3.003	43.45	RRQ	Wilkes et al. (2002)
3C351	0.372	17 04 41.4	+60 44 31	0.696±0.020	45.70	42.96	1.10	15.00	44.87	RLQ	Hardcastle et al. (2002)
3C371	0.051	18 06 50.7	+69 49 28	0.009±0.015	44.25		0.50	17.00	43.04	RLQ	Donato et al. (2005)
IRAS 18216+6418	0.297	18 21 57.3	+64 20 36	0.546±0.023	46.08	43.10	0.78	124.0	45.56	RQQ	Jiménez-Bailón et al. (2007)
ESO103-G035	0.013	18 38 20.3	-65 25 39	-0.817±0.030	43.56	41.61	22.00	266.0	43.43	Sy 2	Risaliti (2002)
3C390	0.052	18 42 09.0	+79 46 17	0.262±0.007	44.13	40.84	0.070	160.0	44.01	FRII	Sambruna et al. (1999)
H1846-786	0.074	18 47 02.8	-78 31 50	-0.116±0.033	44.23	42.40	0.064	76.00	44.01	Sy 1	Quadrelli et al. (2003)
IRAS 19254-7245S	0.0637	19 31 21.4	-72 39 18	-1.339±0.072	44.70	42.71	100.00	2.30		Sy 2	Braito et al. (2003)
CygnusA	0.056	19 59 28.3	+40 44 02	-0.542±0.027	44.01	42.12	20.00	121.4	44.29	FRII	Young et al. (2002)
NGC6860	0.0149	20 08 46.9	-61 06 01	0.109±0.031	43.43	41.22	4.50	89.90	42.69	Sy 1	Winter et al. (2008)
Mrk509	0.034	20 44 09.7	-10 43 25	0.292±0.024	44.23	42.56	0.010	566.5	44.18	Sy 1	Perola et al. (2002)
IRAS 20460+1925	0.181	20 48 17.3	+19 36 54	-0.217±0.011	45.74	43.28	2.59	15.30	44.22	Sy 2	Ogasaka et al. (1997)
IC5135	0.016	21 48 19.5	-34 57 05	-0.273±0.051	43.16	42.55	>100.00	1.60		Sy 2	Levenson et al. (2005)
NGC7172	0.009	22 02 01.9	-31 52 11	-2.022±0.055	42.95	41.77	8.60	130.0	42.57	Sy 2	Bassani et al. (1999)
NGC7213	0.006	22 09 16.2	-47 10 00	0.908±0.024	42.55	40.28	0.010	232.0	42.27	Sy 1	Bianchi et al. (2003)
3C445	0.056	22 23 49.6	-02 06 12	0.358±0.015	44.53		40.00	49.69	44.10	FRII	Grandi et al. (2007)
							7.00				
2MASX J2225	0.147	22 25 54.2	+19 58 37	-0.499±0.065	44.51	42.69	2.45	5.585	43.57	RQQ	Wilkes et al. (2002)
PHL5200	1.981	22 28 30.4	-05 18 55	0.188±0.033	46.68		10.00	0.391	45.07	BALQ	Brinkmann et al. (2002)
NGC7314	0.005	22 35 46.2	-26 03 01	-0.405±0.037	41.87	40.30	1.08	239.0	42.16	Sy 2	Risaliti (2002)
3C452	0.081	22 45 48.8	+39 41 16	-0.136±0.011	43.80	41.11	57.00	1.79	43.11	FRII	Evans et al. (2006)
MCG-2-58-22	0.047	23 04 43.5	-08 41 09	0.372±0.017	44.05	41.95	0.010	310.0	44.21	Sy 1	Bianchi et al. (2004)
IRAS 23060+0505	0.173	23 08 34.2	+05 21 29	-0.285±0.006	45.61	43.63	8.40	15.00	44.49	Sy 2	Risaliti et al. (2000)
NGC7674	0.0289	23 27 56.7	+08 46 45	-0.207±0.038	44.17	42.62	>1000.0	5.00		Sy 2	Bassani et al. (1999)
2MASX J2344	0.199	23 44 49.5	+12 21 43	0.171±0.054	44.87	43.03	0.650	5.10	43.78	RRQ	Wilkes et al. (2005)

[a] Intrinsic column density in units of 10^{22} cm^{-2}. [b]Observed 2-10 keV flux in units of 10^{-13} erg cm^{-2} s^{-1}. [c]Logarithm of intrinsic 2-10 keV luminosity in units of erg s^{-1}. [d] Sy 1 = Seyfert 1 galaxy; Sy 2 = Seyfert 2 galaxy; BALQ = broad absorption-line quasar; FRII = Fanaroff and Riley Class II radio galaxy; RQQ = radio-quiet quasar; RLQ = radio-loud quasar; LINER = low-ionization nuclear emission-line region.

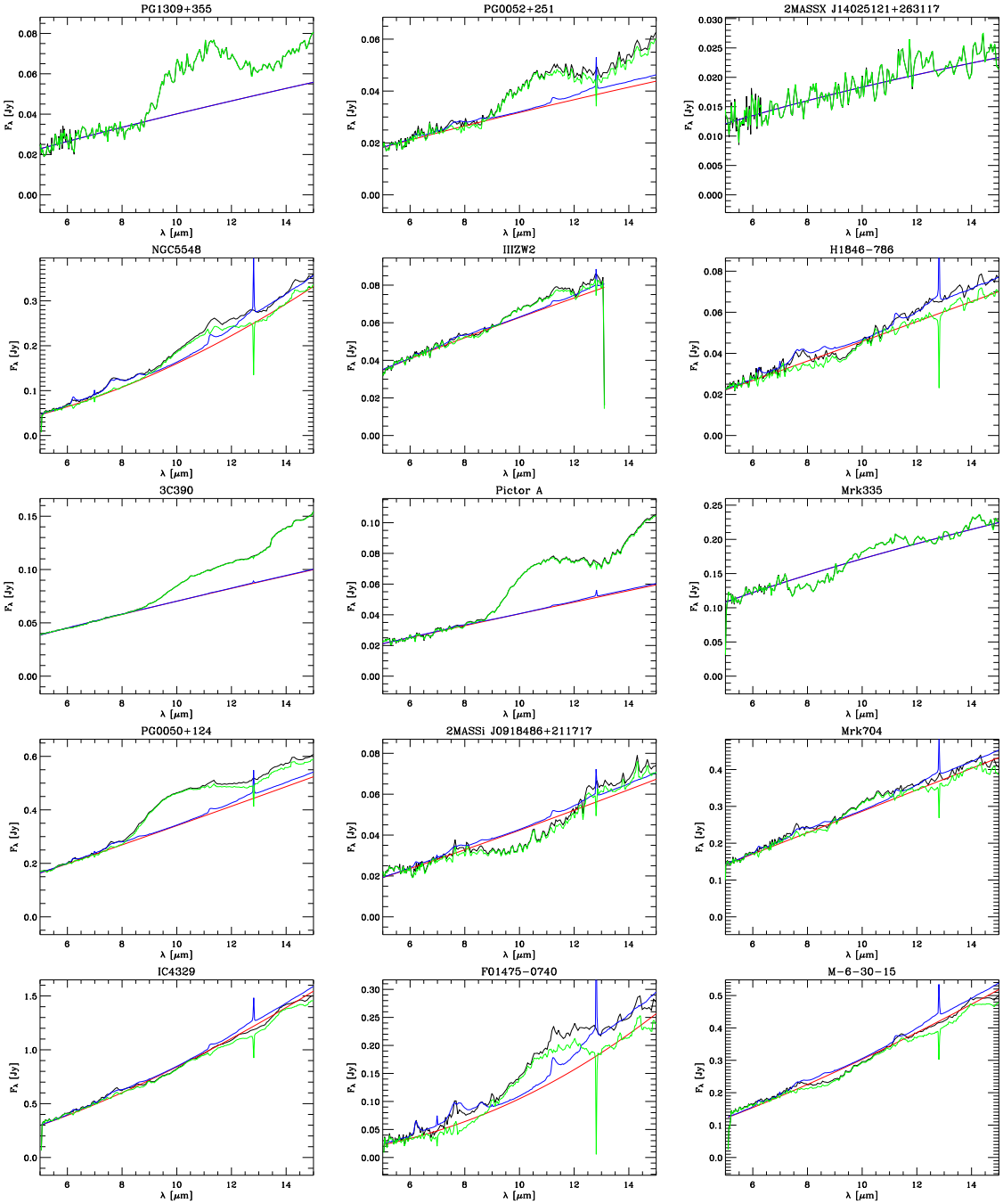
PG1309+355
PG0052+251
2MASSX J14025121+263117
NGC5548
IIIZW2
H1846−786
3C390
Pictor A
Mrk335
PG0050+124
2MASSi J0918486+211717
Mrk704
IC4329
F01475−0740
M−6−30−15
λ [μm]
Fλ [Jy]

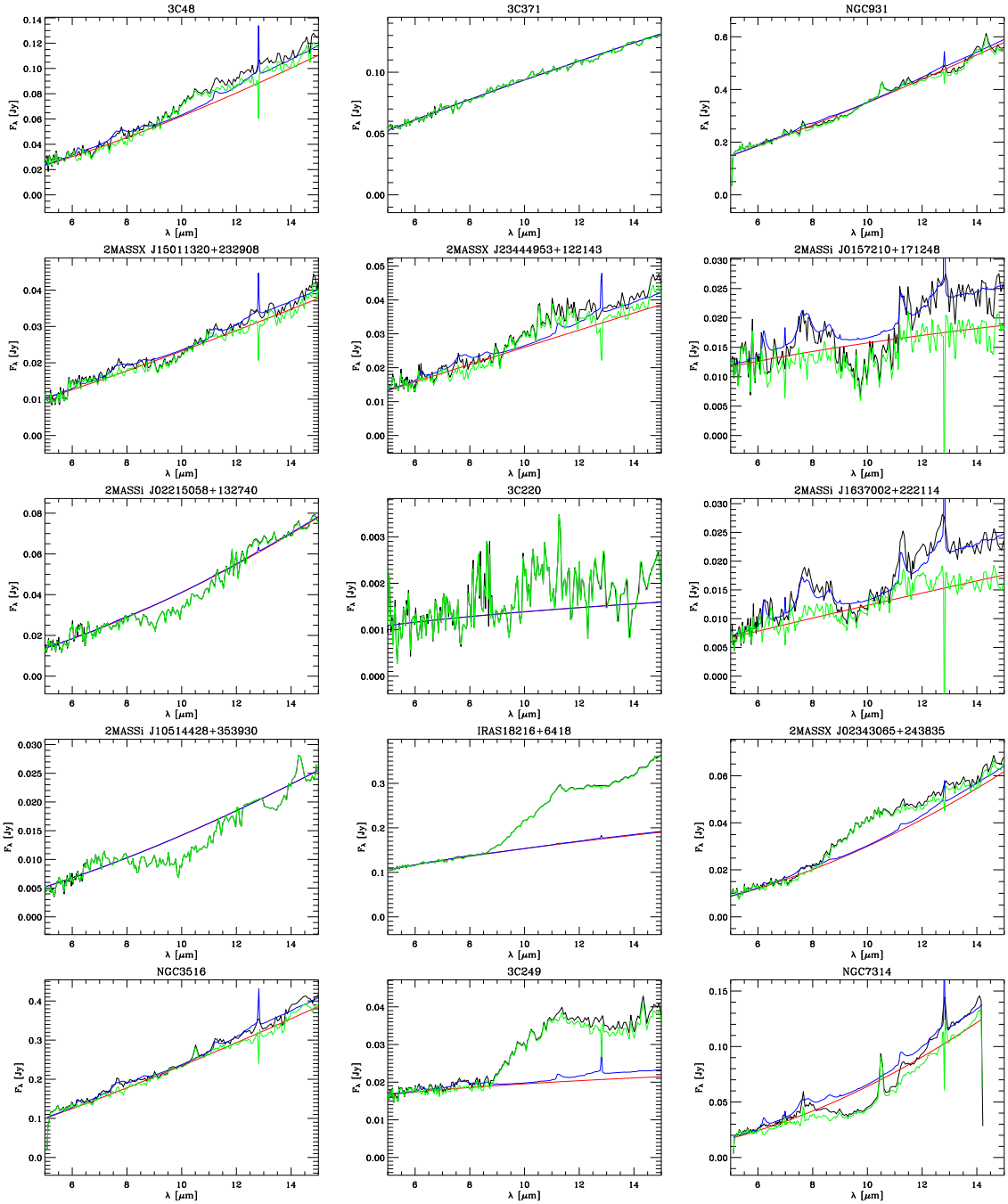
3C48
3C371
NGC931
2MASSX J15011320+232908
2MASSX J23444953+122143
2MASSi J0157210+171248
2MASSi J02215058+132740
3C220
2MASSi J1637002+222114
2MASSi J10514428+353930
IRAS18216+6418
2MASSX J02343065+243835
NGC3516
3C249
NGC7314
λ [μm]
Fλ [Jy]

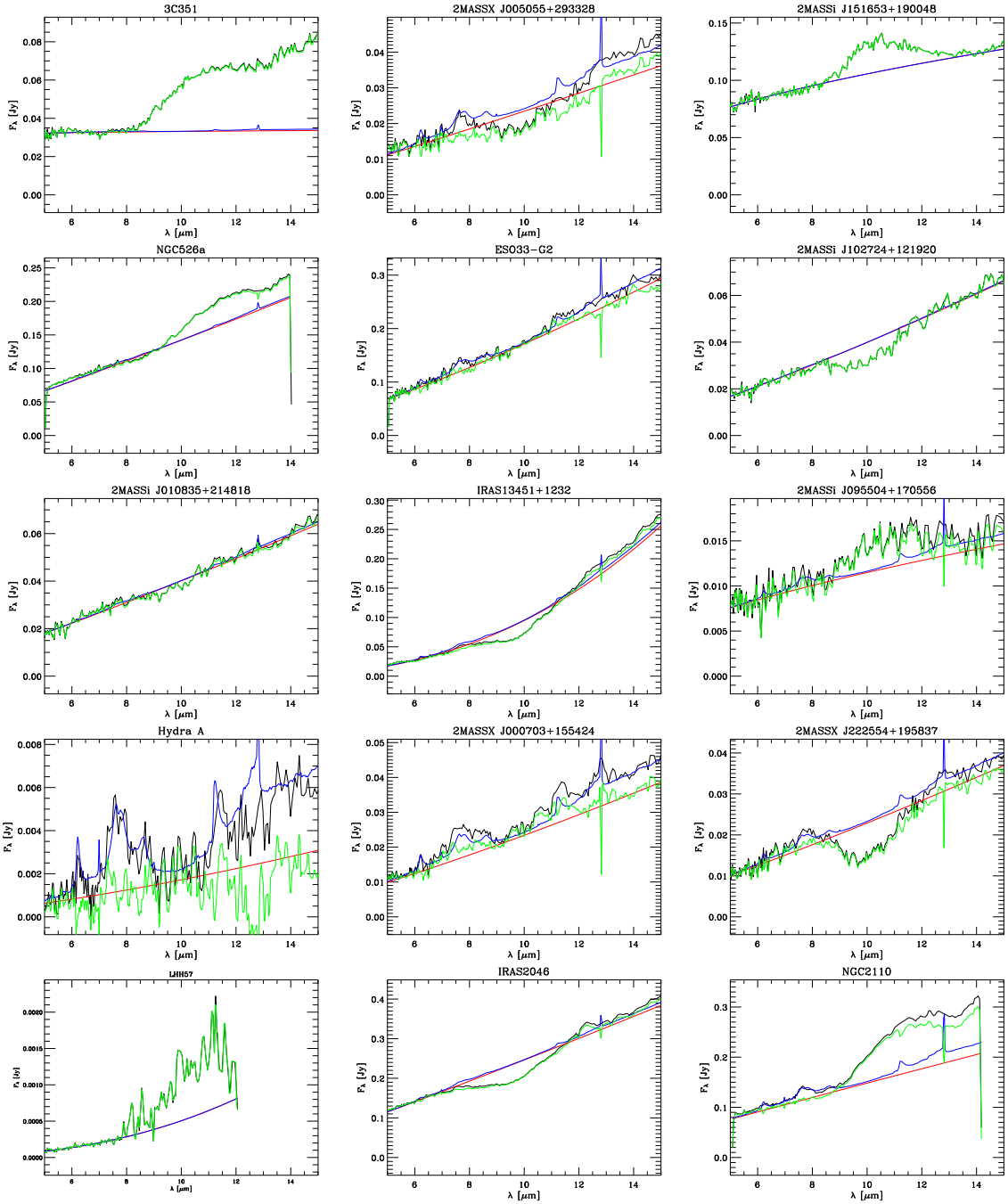
3C351
2MASSX J005055+293328
2MASSi J151653+190048
NGC526a
ES033−G2
2MASSi J102724+121920
2MASSi J010835+214818
IRAS13451+1232
2MASSi J095504+170556
Hydra A
2MASSX J000703+155424
2MASSX J222554+195837
LHH57
IRAS2046
NGC2110
λ [μm]
Fλ [Jy]

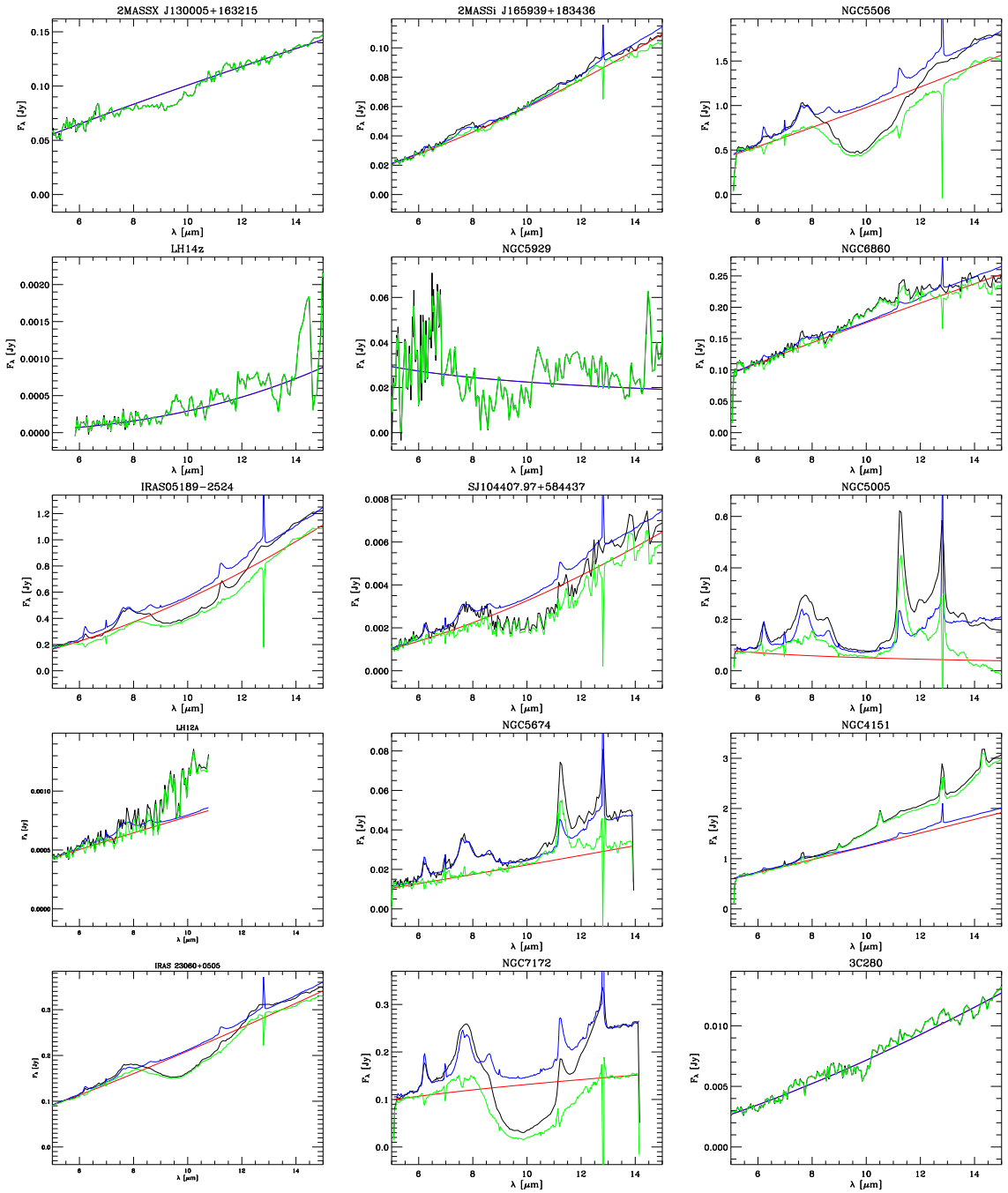
2MASSX J130005+163215
2MASSi J165939+183436
NGC5506
LH14z
NGC5929
NGC6860
IRAS05189−2524
SJ104407.97+584437
NGC5005
LH12A
NGC5674
NGC4151
IRAS 23060+0505
NGC7172
3C280
λ [μm]
Fλ [Jy]

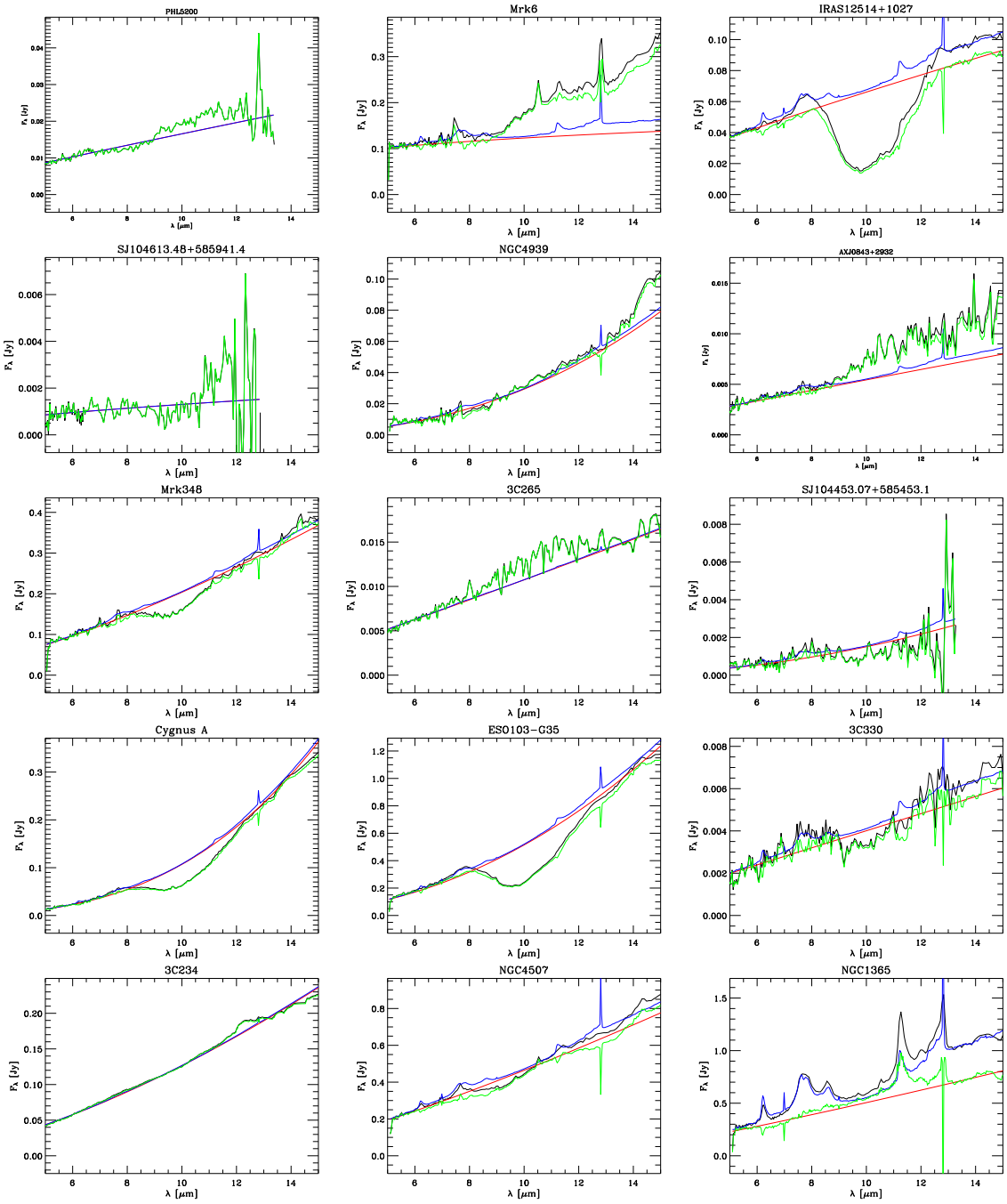
PHL5200
Mrk6
IRAS12514+1027
SJ104613.48+585941.4
NGC4939
AXJ0843+2932
Mrk348
3C265
SJ104453.07+585453.1
Cygnus A
ES0103-G35
3C330
3C234
NGC4507
NGC1365
λ [μm]
Fλ [Jy]

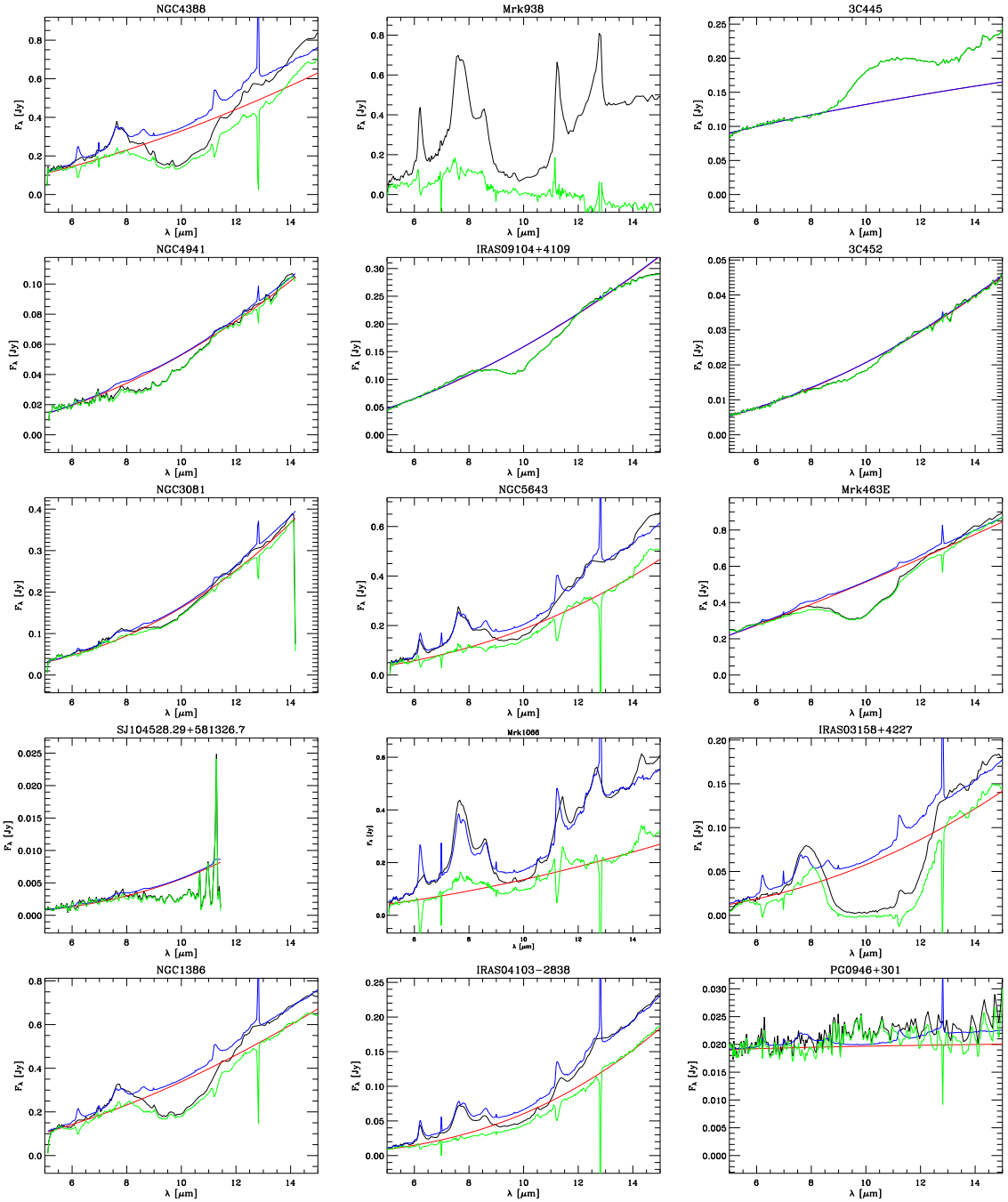
NGC4388
Mrk938
3C445
NGC4941
IRAS09104+4109
3C452
NGC3081
NGC5643
Mrk463E
SJ104528.29+581326.7
Mrk1066
IRAS03158+4227
NGC1386
IRAS04103−2838
PG0946+301
λ [μm]
Fλ [Jy]

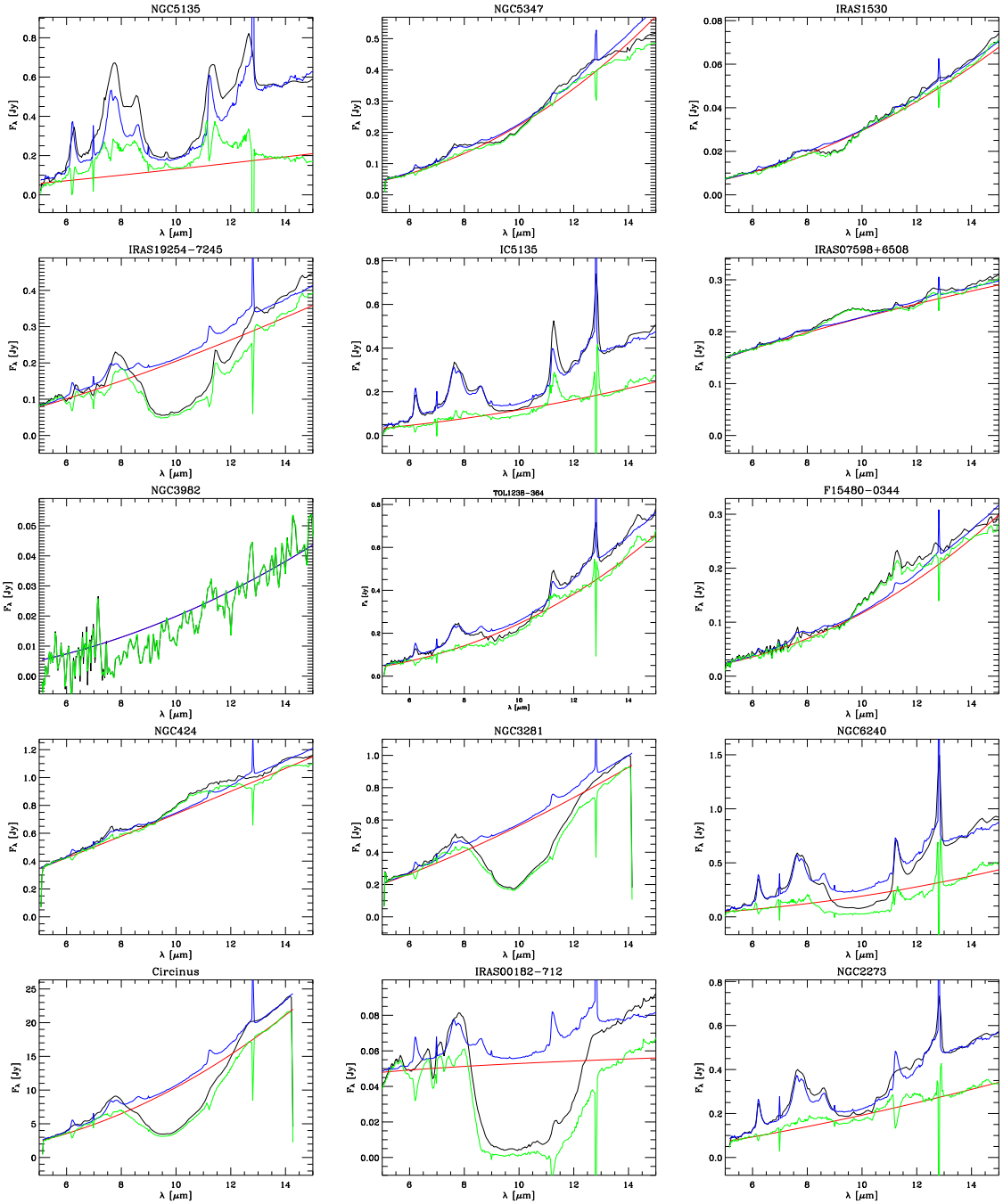
NGC5135
NGC5347
IRAS1530
IRAS19254−7245
IC5135
IRAS07598+6508
NGC3982
TOL1238−364
F15480−0344
NGC424
NGC3281
NGC6240
Circinus
IRAS00182−712
NGC2273
λ [μm]
Fλ [Jy]

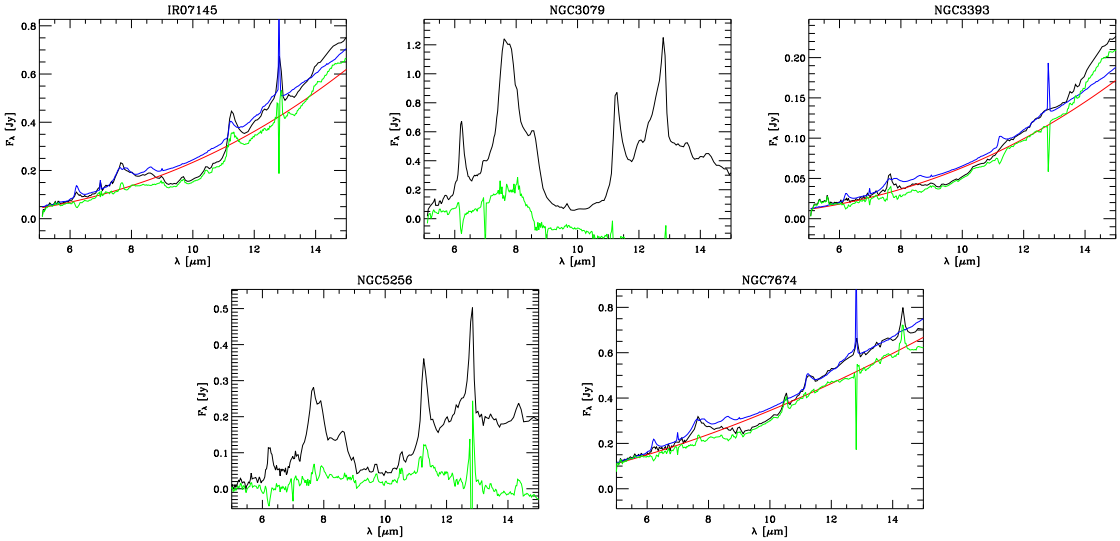
IR07145
NGC3079
NGC3393
NGC5256
NGC7674
F_λ [Jy]
λ [μm]

BIBLIOGRAPHY

Anderson, S. F., Fan, X., Richards, G. T., et al. 2001, AJ, 122, 503

Ando, M., Ohta, K., Iwata, I., et al. 2004, Astrophysical Journal, 610, 635

Antonucci, R. 1993, Annual Review of Astron and Astrophys, 31, 473

Archibald, E. N., Dunlop, J. S., Hughes, D. H., et al. 2001, Monthly Notices of the RAS, 323, 417

Baffa, C., Comoretto, G., Gennari, S., et al. 2001, Astronomy and Astrophysics, 378, 722

Barth, A. J., Martini, P., Nelson, C. H., & Ho, L. C. 2003, Astrophysical Journal Letters, 594, L95

Bassani, L., Dadina, M., Maiolino, R., et al. 1999, Astrophysical Journal Supplement, 121, 473

Baum, S. A., Zirbel, E. L., & O'Dea, C. P. 1995, Astrophysical Journal, 451, 88

Beelen, A., Cox, P., Benford, D. J., et al. 2006, Astrophysical Journal, 642, 694

Belsole, E., Worrall, D. M., & Hardcastle, M. J. 2006, Monthly Notices of the RAS, 366, 339

Bertoldi, F., Carilli, C. L., Cox, P., et al. 2003a, Astronomy and Astrophysics, 406, L55

Bertoldi, F., Cox, P., Neri, R., et al. 2003b, Astronomy and Astrophysics, 409, L47

Bianchi, S., Balestra, I., Matt, G., Guainazzi, M., & Perola, G. C. 2003, Astronomy and Astrophysics, 402, 141

Bianchi, S., Chiaberge, M., Piconcelli, E., Guainazzi, M., & Matt, G. 2008, Monthly Notices of the RAS, 386, 105

Bianchi, S., Matt, G., Balestra, I., Guainazzi, M., & Perola, G. C. 2004, Astronomy and Astrophysics, 422, 65

Braito, V., Della Ceca, R., Piconcelli, E., et al. 2004, Astronomy and Astrophysics, 420, 79

Braito, V., Franceschini, A., Della Ceca, R., et al. 2003, Astronomy and Astrophysics, 398, 107

Brinkmann, W., Ferrero, E., & Gliozzi, M. 2002, Astronomy and Astrophysics, 385, L31

Brotherton, M. S., Wills, B. J., Steidel, C. C., & Sargent, W. L. W. 1994, Astrophysical Journal, 423, 131

Buchanan, C. L., Gallimore, J. F., O'Dea, C. P., et al. 2006, Astronomical Journal, 132, 401

Calura, F., Pipino, A., & Matteucci, F. 2008, Astronomy and Astrophysics, 479, 669

Cappi, M., Panessa, F., Bassani, L., et al. 2006, Astronomy and Astrophysics, 446, 459

Carilli, C. L., Bertoldi, F., Omont, A., et al. 2001a, Astronomical Journal, 122, 1679

Carilli, C. L., Bertoldi, F., Rupen, M. P., et al. 2001b, Astrophysical Journal, 555, 625

Croom, S. M., Rhook, K., Corbett, E. A., et al. 2002, Monthly Notices of the RAS, 337, 275

D'Ammando, F., Bianchi, S., Jiménez-Bailón, E., & Matt, G. 2008, Astronomy and Astrophysics, 482, 499

Della Ceca, R., Braito, V., Beckmann, V., et al. 2003, Astronomy and Astrophysics, 406, 555

Della Ceca, R., Severgnini, P., Caccianiga, A., et al. 2008, Memorie della Societa Astronomica Italiana, 79, 65

Dennett-Thorpe, J., Barthel, P. D., & van Bemmel, I. M. 2000, Astronomy and Astrophysics, 364, 501

Di Matteo, T., Springel, V., & Hernquist, L. 2005, Nature, 433, 604

Dietrich, M., Appenzeller, I., Hamann, F., et al. 2003a, Astronomy and Astrophysics, 398, 891

Dietrich, M., Appenzeller, I., Vestergaard, M., & Wagner, S. J. 2002, Astrophysical Journal, 564, 581

Dietrich, M., Appenzeller, I., Wagner, S. J., et al. 1999, Astronomy and Astrophysics, 352, L1

Dietrich, M. & Hamann, F. 2004, Astrophysical Journal, 611, 761

Dietrich, M., Hamann, F., Shields, J. C., et al. 2003b, Astrophysical Journal, 589, 722

Donato, D., Sambruna, R. M., & Gliozzi, M. 2005, Astronomy and Astrophysics, 433, 1163

Dwek, E., Galliano, F., & Jones, A. P. 2007, Astrophysical Journal, 662, 927

Efstathiou, A. 2006, Monthly Notices of the RAS, 371, L70

Elfgren, E. & Désert, F.-X. 2004, Astronomy and Astrophysics, 425, 9

Elvis, M., Marengo, M., & Karovska, M. 2002, Astrophysical Journal Letters, 567, L107

Elvis, M., Wilkes, B. J., McDowell, J. C., et al. 1994, Astrophysical Journal Supplement, 95, 1

Evans, D. A., Worrall, D. M., Hardcastle, M. J., Kraft, R. P., & Birkinshaw, M. 2006, Astrophysical Journal, 642, 96

Fan, X., Hennawi, J. F., Richards, G. T., et al. 2004, Astronomical Journal, 128, 515

Fan, X., Narayanan, V. K., Lupton, R. H., et al. 2001, Astronomical Journal, 122, 2833

Fan, X., Strauss, M. A., Richards, G. T., et al. 2006, Astronomical Journal, 131, 1203

Fan, X., Strauss, M. A., Schneider, D. P., et al. 2003, Astronomical Journal, 125, 1649

Fanaroff, B. L. & Riley, J. M. 1974, Monthly Notices of the RAS, 167, 31P

Ferland, G. J., Baldwin, J. A., Korista, K. T., et al. 1996, Astrophysical Journal, 461, 683

Filippenko, A. V. 2003, 290, 369

Freudling, W., Corbin, M. R., & Korista, K. T. 2003, Astrophysical Journal Letters, 587, L67

Gabel, J. R., Arav, N., & Kim, T.-S. 2006, Astrophysical Journal, 646, 742

Gallo, L. C., Lehmann, I., Pietsch, W., et al. 2006, Monthly Notices of the RAS, 365, 688

George, I. M., Turner, T. J., Yaqoob, T., et al. 2000, Astrophysical Journal, 531, 52

Ghosh, K. K. 1992, Monthly Notices of the RAS, 259, 175

Gondoin, P., Lumb, D., Siddiqui, H., Guainazzi, M., & Schartel, N. 2001, Astronomy and Astrophysics, 373, 805

Goto, T. 2006, Monthly Notices of the RAS, 371, 769

Granato, G. L. & Danese, L. 1994, Monthly Notices of the RAS, 268, 235

Granato, G. L., De Zotti, G., Silva, L., Bressan, A., & Danese, L. 2004, Astrophysical Journal, 600, 580

Granato, G. L., Silva, L., Monaco, P., et al. 2001, Monthly Notices of the RAS, 324, 757

Grandi, P., Guainazzi, M., Cappi, M., & Ponti, G. 2007, Monthly Notices of the RAS, 381, L21

Groves, B. A., Heckman, T. M., & Kauffmann, G. 2006, Monthly Notices of the RAS, 371, 1559

Guainazzi, M., Matt, G., & Perola, G. C. 2005, Astronomy and Astrophysics, 444, 119

Guainazzi, M., Rodriguez-Pascual, P., Fabian, A. C., Iwasawa, K., & Matt, G. 2004, Monthly Notices of the RAS, 355, 297

Haas, M., Klaas, U., Müller, S. A. H., et al. 2003, Astronomy and Astrophysics, 402, 87

Haas, M., Müller, S. A. H., Chini, R., et al. 2000, Astronomy and Astrophysics, 354, 453

Hamann, F. & Ferland, G. 1993, Astrophysical Journal, 418, 11

Hamann, F. & Ferland, G. 1999, Annual Review of Astron and Astrophys, 37, 487

Hao, L., Spoon, H. W. W., Sloan, G. C., et al. 2005, Astrophysical Journal Letters, 625, L75

Hao, L., Weedman, D. W., Spoon, H. W. W., et al. 2007, Astrophysical Journal Letters, 655, L77

Hardcastle, M. J., Birkinshaw, M., Cameron, R. A., et al. 2002, Astrophysical Journal, 581, 948

Hogg, D. W. 1999, ArXiv Astrophysics e-prints

Hönig, S. F., Beckert, T., Ohnaka, K., & Weigelt, G. 2006, Astronomy and Astrophysics, 452, 459

Hook, I. M., Becker, R. H., McMahon, R. G., & White, R. L. 1998, Monthly Notices of the RAS, 297, 1115

Hooper, E. J., Impey, C. D., Foltz, C. B., & Hewett, P. C. 1995, Astrophysical Journal, 445, 62

Hopkins, P. F., Hernquist, L., Cox, T. J., & Kereš, D. 2008, Astrophysical Journal Supplement, 175, 356

Horst, H., Gandhi, P., Smette, A., & Duschl, W. J. 2008, Astronomy and Astrophysics, 479, 389

Houck, J. R., Roellig, T. L., van Cleve, J., et al. 2004, Astrophysical Journal Supplement, 154, 18

Immler, S., Brandt, W. N., Vignali, C., et al. 2003, Astronomical Journal, 126, 153

Isaak, K. G., McMahon, R. G., Hills, R. E., & Withington, S. 1994, Monthly Notices of the RAS, 269, L28+

Isaak, K. G., Priddey, R. S., McMahon, R. G., et al. 2002, Monthly Notices of the RAS, 329, 149

Iwamuro, F., Kimura, M., Eto, S., et al. 2004, Astrophysical Journal, 614, 69

Iwamuro, F., Motohara, K., Maihara, T., et al. 2002, Astrophysical Journal, 565, 63

Iwasawa, K., Crawford, C. S., Fabian, A. C., & Wilman, R. J. 2005, Monthly Notices of the RAS, 362, L20

Iwasawa, K., Wilson, A. S., Fabian, A. C., & Young, A. J. 2003, Monthly Notices of the RAS, 345, 369

Jenness, T. & Economou, F. 1999, in Astronomical Society of the Pacific Conference Series, Vol. 172, Astronomical Data Analysis Software and Systems VIII, ed. D. M. Mehringer, R. L. Plante, & D. A. Roberts, 171–+

Jiang, L., Fan, X., Hines, D. C., et al. 2006, Astronomical Journal, 132, 2127

Jiang, L., Fan, X., Vestergaard, M., et al. 2007, Astronomical Journal, 134, 1150

Jiménez-Bailón, E., Santos-Lleó, M., Piconcelli, E., et al. 2007, Astronomy and Astrophysics, 461, 917

Juarez, Y., Maiolino, R., Mujica, R., et al. 2009, Astronomy and Astrophysics, 494, L25

Kaspi, S., Brandt, W. N., Netzer, H., et al. 2001, Astrophysical Journal, 554, 216

Kennicutt, Jr., R. C. 1998, Annual Review of Astron and Astrophys, 36, 189

Krolik, J. H. & Begelman, M. C. 1988, Astrophysical Journal, 329, 702

Kurucz, R. 1993, ATLAS9 Stellar Atmosphere Programs and 2 km/s grid. Kurucz CD-ROM No. 13. Cambridge, Mass.: Smithsonian Astrophysical Observatory, 1993., 13

Landi, R., Masetti, N., Morelli, L., et al. 2007, Astrophysical Journal, 669, 109

Lanzuisi, G., Piconcelli, E., Fiore, F., et al. 2009, ArXiv e-prints

Laor, A., Jannuzi, B. T., Green, R. F., & Boroson, T. A. 1997, Astrophysical Journal, 489, 656

Lehner, N., Wakker, B. P., & Savage, B. D. 2004, Astrophysical Journal, 615, 767

Levenson, N. A., Heckman, T. M., Krolik, J. H., Weaver, K. A., & Życki, P. T. 2006, Astrophysical Journal, 648, 111

Levenson, N. A., Weaver, K. A., Heckman, T. M., Awaki, H., & Terashima, Y. 2005, Astrophysical Journal, 618, 167

Lutz, D., Maiolino, R., Spoon, H. W. W., & Moorwood, A. F. M. 2004, Astronomy and Astrophysics, 418, 465

Lutz, D., Sturm, E., Tacconi, L. J., et al. 2008, Astrophysical Journal, 684, 853

Mainieri, V., Bergeron, J., Hasinger, G., et al. 2002, Astronomy and Astrophysics, 393, 425

Maiolino, R., Cox, P., Caselli, P., et al. 2005, Astronomy and Astrophysics, 440, L51

Maiolino, R., Juarez, Y., Mujica, R., Nagar, N. M., & Oliva, E. 2003, Astrophysical Journal Letters, 596, L155

Maiolino, R., Nagao, T., Marconi, A., et al. 2006, Memorie della Societa Astronomica Italiana, 77, 643

Maiolino, R., Schneider, R., Oliva, E., et al. 2004, Nature, 431, 533

Maiolino, R., Shemmer, O., Imanishi, M., et al. 2007, Astronomy and Astrophysics, 468, 979

Marziani, P., Sulentic, J. W., Zamanov, R., et al. 2003, Astrophysical Journal Supplement, 145, 199

Mathur, S., Green, P. J., Arav, N., et al. 2000, Astrophysical Journal Letters, 533, L79

Matt, G., Bianchi, S., D'Ammando, F., & Martocchia, A. 2004, Astronomy and Astrophysics, 421, 473

Matt, G., Bianchi, S., Guainazzi, M., et al. 2003, Astronomy and Astrophysics, 399, 519

Matt, G., Guainazzi, M., Maiolino, R., et al. 1999, Astronomy and Astrophysics, 341, L39

Matteucci, F. & Padovani, P. 1993, Astrophysical Journal, 419, 485

McGreer, I. D., Becker, R. H., Helfand, D. J., & White, R. L. 2006, Astrophysical Journal, 652, 157

McIntosh, D. H., Rieke, M. J., Rix, H.-W., Foltz, C. B., & Weymann, R. J. 1999, Astrophysical Journal, 514, 40

Morgan, H. L. & Edmunds, M. G. 2003, Monthly Notices of the RAS, 343, 427

Mortlock, D. J., Patel, M., Warren, S. J., et al. 2008, ArXiv e-prints

Nagao, T., Maiolino, R., & Marconi, A. 2006a, Astronomy and Astrophysics, 447, 863

Nagao, T., Marconi, A., & Maiolino, R. 2006b, Astronomy and Astrophysics, 447, 157

Nenkova, M., Ivezić, Ž., & Elitzur, M. 2002, Astrophysical Journal Letters, 570, L9

Nenkova, M., Sirocky, M. M., Ivezić, Ž., & Elitzur, M. 2008a, Astrophysical Journal, 685, 147

Nenkova, M., Sirocky, M. M., Nikutta, R., Ivezić, Ž., & Elitzur, M. 2008b, Astrophysical Journal, 685, 160

Netzer, H. 2008, Memorie della Societa Astronomica Italiana, 79, 1083

Netzer, H., Shemmer, O., Maiolino, R., et al. 2004, Astrophysical Journal, 614, 558

Ogasaka, Y., Inoue, H., Brandt, W. N., et al. 1997, Publications of the Astronomical Society of Japan, 49, 179

Oliva, E. 2003, Memorie della Societa Astronomica Italiana, 74, 118

Omont, A., Beelen, A., Bertoldi, F., et al. 2003, Astronomy and Astrophysics, 398, 857

Omont, A., Cox, P., Bertoldi, F., et al. 2001, Astronomy and Astrophysics, 374, 371

Osterbrock Donald E., F. G. J. 2006, Astrophysics of Gaseous Nebulae and Active Galactic Nuclei (University Science Books)

Panessa, F., Bassani, L., Cappi, M., et al. 2006, Astronomy and Astrophysics, 455, 173

Pellegrini, S., Cappi, M., Bassani, L., della Ceca, R., & Palumbo, G. G. C. 2000, Astronomy and Astrophysics, 360, 878

Pentericci, L., Rix, H.-W., Prada, F., et al. 2003, Astronomy and Astrophysics, 410, 75

Perola, G. C., Matt, G., Cappi, M., et al. 2002, Astronomy and Astrophysics, 389, 802

Petric, A. O., Carilli, C. L., Bertoldi, F., et al. 2006, Astronomical Journal, 132, 1307

Pickles, A. J. 1998, Publications of the ASP, 110, 863

Piconcelli, E., Bianchi, S., Miniutti, G., et al. 2008, Astronomy and Astrophysics, 480, 671

Piconcelli, E., Fiore, F., Nicastro, F., et al. 2007, Astronomy and Astrophysics, 473, 85

Piconcelli, E., Jimenez-Bailón, E., Guainazzi, M., et al. 2005, Astronomy and Astrophysics, 432, 15

Pier, E. A. & Krolik, J. H. 1992, Astrophysical Journal, 401, 99

Pier, E. A. & Krolik, J. H. 1993, Astrophysical Journal, 418, 673

Pipino, A. & Matteucci, F. 2004, Monthly Notices of the RAS, 347, 968

Polletta, M., Weedman, D., Hönig, S., et al. 2008, Astrophysical Journal, 675, 960

Polletta, M. d. C., Wilkes, B. J., Siana, B., et al. 2006, Astrophysical Journal, 642, 673

Pounds, K. A., Reeves, J. N., King, A. R., & Page, K. L. 2004, Monthly Notices of the RAS, 350, 10

Priddey, R. S., Isaak, K. G., McMahon, R. G., & Omont, A. 2003a, Monthly Notices of the RAS, 339, 1183

Priddey, R. S., Isaak, K. G., McMahon, R. G., Robson, E. I., & Pearson, C. P. 2003b, Monthly Notices of the RAS, 344, L74

Quadrelli, A., Malizia, A., Bassani, L., & Malaguti, G. 2003, Astronomy and Astrophysics, 411, 77

Reynolds, C. S., Fabian, A. C., & Inoue, H. 1995, Monthly Notices of the RAS, 276, 1311

Risaliti, G. 2002, Astronomy and Astrophysics, 386, 379

Risaliti, G., Elvis, M., Fabbiano, G., Baldi, A., & Zezas, A. 2005, Astrophysical Journal Letters, 623, L93

Risaliti, G., Gilli, R., Maiolino, R., & Salvati, M. 2000, Astronomy and Astrophysics, 357, 13

Robson, I., Priddey, R. S., Isaak, K. G., & McMahon, R. G. 2004, Monthly Notices of the RAS, 351, L29

Ruiz, A., Carrera, F. J., & Panessa, F. 2007, Astronomy and Astrophysics, 471, 775

Sambruna, R. M., Chartas, G., Eracleous, M., Mushotzky, R. F., & Nousek, J. A. 2000, Astrophysical Journal Letters, 532, L91

Sambruna, R. M., Eracleous, M., & Mushotzky, R. F. 1999, Astrophysical Journal, 526, 60

Schartmann, M., Meisenheimer, K., Camenzind, M., Wolf, S., & Henning, T. 2005, Astronomy and Astrophysics, 437, 861

Schartmann, M., Meisenheimer, K., Camenzind, M., et al. 2008, Astronomy and Astrophysics, 482, 67

Schweitzer, M., Groves, B., Netzer, H., et al. 2008, Astrophysical Journal, 679, 101

Schweitzer, M., Lutz, D., Sturm, E., et al. 2006, Astrophysical Journal, 649, 79

Shemmer, O., Brandt, W. N., Vignali, C., et al. 2005, Astrophysical Journal, 630, 729

Shemmer, O., Netzer, H., Maiolino, R., et al. 2004, Astrophysical Journal, 614, 547

Shi, Y., Ogle, P., Rieke, G. H., et al. 2007, Astrophysical Journal, 669, 841

Shi, Y., Rieke, G. H., Hines, D. C., et al. 2006, Astrophysical Journal, 653, 127

Shu, X. W., Wang, J. X., Jiang, P., Fan, L. L., & Wang, T. G. 2007, Astrophysical Journal, 657, 167

Siebenmorgen, R., Haas, M., Krügel, E., & Schulz, B. 2005, Astronomy and Astrophysics, 436, L5

Siebenmorgen, R., Krügel, E., & Spoon, H. W. W. 2004, Astronomy and Astrophysics, 414, 123

Siemiginowska, A., Aldcroft, T. L., Bechtold, J., et al. 2003, Publications of the Astronomical Society of Australia, 20, 113

Sirocky, M. M., Levenson, N. A., Elitzur, M., Spoon, H. W. W., & Armus, L. 2008, Astrophysical Journal, 678, 729

Smith, P. S. 1996, 110, 135

Spoon, H. W. W., Marshall, J. A., Houck, J. R., et al. 2007, Astrophysical Journal Letters, 654, L49

Stern, D., Djorgovski, S. G., Perley, R. A., de Carvalho, R. R., & Wall, J. V. 2000, Astronomical Journal, 119, 1526

Sturm, E., Hasinger, G., Lehmann, I., et al. 2006, Astrophysical Journal, 642, 81

Sturm, E., Lutz, D., Tran, D., et al. 2000, Astronomy and Astrophysics, 358, 481

Sturm, E., Schweitzer, M., Lutz, D., et al. 2005, Astrophysical Journal Letters, 629, L21

Teng, S. H., Veilleux, S., Wilson, A. S., et al. 2008, Astrophysical Journal, 674, 133

Urry, C. M. & Padovani, P. 1995, Publications of the ASP, 107, 803

Vermeulen, R. C., Ogle, P. M., Tran, H. D., et al. 1995, Astrophysical Journal Letters, 452, L5+

Véron-Cetty, M.-P., Joly, M., & Véron, P. 2004, Astronomy and Astrophysics, 417, 515

Vignali, C. & Comastri, A. 2002, Astronomy and Astrophysics, 381, 834

Vignali, C., Comastri, A., Stirpe, G. M., et al. 1998, Astronomy and Astrophysics, 333, 411

Wang, J.-M., Ho, L. C., & Staubert, R. 2003, Astronomy and Astrophysics, 409, 887

Wang, J.-M., Zhang, E.-P., & Luo, B. 2005, Astrophysical Journal Letters, 627, L5

Wang, R., Carilli, C. L., Beelen, A., et al. 2007, Astronomical Journal, 134, 617

Wang, R., Carilli, C. L., Wagg, J., et al. 2008, Astrophysical Journal, 687, 848

Warner, C., Hamann, F., & Dietrich, M. 2003, Astrophysical Journal, 596, 72

Watson, M. G., Schröder, A. C., Fyfe, D., et al. 2009, Astronomy and Astrophysics, 493, 339

Weedman, D., Polletta, M., Lonsdale, C. J., et al. 2006, Astrophysical Journal, 653, 101

Weedman, D. W., Hao, L., Higdon, S. J. U., et al. 2005, Astrophysical Journal, 633, 706

Weymann, R. J., Morris, S. L., Foltz, C. B., & Hewett, P. C. 1991, Astrophysical Journal, 373, 23

Wilkes, B. J., Pounds, K. A., Schmidt, G. D., et al. 2005, Astrophysical Journal, 634, 183

Wilkes, B. J., Schmidt, G. D., Cutri, R. M., et al. 2002, Astrophysical Journal Letters, 564, L65

Willott, C. J., Delorme, P., Omont, A., et al. 2007, Astronomical Journal, 134, 2435

Willott, C. J., Delorme, P., Reylé, C., et al. 2009, Astronomical Journal, 137, 3541

Willott, C. J., McLure, R. J., & Jarvis, M. J. 2003, Astrophysical Journal Letters, 587, L15

Wilms, J., Reynolds, C. S., Begelman, M. C., et al. 2001, Monthly Notices of the RAS, 328, L27

Winter, L. M., Mushotzky, R. F., Tueller, J., & Markwardt, C. 2008, Astrophysical Journal, 674, 686

Young, A. J., Wilson, A. S., Terashima, Y., Arnaud, K. A., & Smith, D. A. 2002, Astrophysical Journal, 564, 176

Zylka, R. 1998, MOPSI User's Manual